Optical Study of Two-dimensional Atomic Hydrogen Gas

Aan mijn ouders en mijn zus

Optical Study of Two-dimensional Atomic Hydrogen Gas

ACADEMISCH PROEFSCHRIFT

ter verkrijging van de graad van doctor
aan de Universiteit van Amsterdam,
op gezag van de Rector Magnificus
prof.dr. J.J.M. Franse
ten overstaan van een door het college voor promoties
ingestelde commissie in het openbaar te verdedigen
in de Aula der Universiteit
op donderdag 30 september 1999 te 15 uur

door

Allard Pieter Mosk

geboren te Amsterdam

Promotor:	prof. dr. J.T.M. Walraven
Co-promotor:	dr. M.W. Reynolds

Commissie:	dr. T. W. Hijmans
	dr. S. Jaakkola
	prof. dr. A. Lagendijk
	prof. dr. ir. H. B. van Linden van den Heuvell
	prof. dr. G. V. Shlyapnikov
	prof. dr. B. J. Verhaar

Faculteit der wiskunde, informatica, natuur- en sterrenkunde

The work described in this thesis is part of the research program of the
Stichting voor Fundamenteel Onderzoek der Materie (FOM),
which is financially supported by the
Nederlandse Organisatie voor Wetenschappelijk Onderzoek (NWO).

The work was carried out at the
Van der Waals–Zeeman Instituut
Universiteit van Amsterdam
Valckenierstraat 65
1018 XE Amsterdam
The Netherlands

Contents

Chapter 1

Introduction

1.1 Spin-polarized hydrogen: a quantum gas

The quantum nature of matter becomes more obvious as one lowers the temperature. However, at temperatures much below one Kelvin the equilibrium state of all materials is either solid or liquid. Although manifestly quantum-mechanical behavior, such as superfluidity and superconductivity, exists in these condensed phases, the influence of interatomic interactions overshadows many aspects of the quantum behavior. Moreover, the interactions preclude a theoretical description of such systems from first principles. One would prefer to study many-body quantum behavior in simple, dilute systems. Cold atomic gases provide just such dilute systems, and although they are far from absolute thermal equilibrium, their metastable gaseous state is sufficiently long-lived to be cooled to the regime where quantum effects can be studied. Such atomic gases are *quantum gases:* dilute enough that only binary collisions are relevant, and cold enough that only a single quantum mechanical collision channel (spherical wave) is open [1]. The thermodynamics of a quantum gas is characterized completely by the scattering length a, which expresses the effect of the interactions, the atom density n, and the thermal de Broglie wavelength $\Lambda = (2\pi\hbar^2/mk_{\rm B}T)^{1/2}$, which expresses the quantum-mechanical uncertainty in the positions of the atoms. Here T is the temperature of the gas, $k_{\rm B}$ is Boltzmann's constant and m is the mass of the atoms in the gas. Atomic hydrogen (H) was the first quantum gas to be stabilized [2], and since then the field of study of these gases has rapidly expanded, most notably due to the development of laser cooling and trapping techniques.

The most widely known examples of quantum gases available at this time are

the Bose-Einstein condensed atomic gases [3]. When a gas is cooled so deeply that the thermal de Broglie wavelength exceeds the mean interatomic distance, $n\Lambda^3 \gtrsim 1$, macroscopic quantum effects on the state of the gas become obvious. In a Bose gas a large fraction of the atoms condenses into a macroscopic quantum state, the Bose-Einstein condensate. Only in a dilute quantum gas this macroscopic quantum behavior can be fully understood in terms of a microscopic theory.

Atomic hydrogen gas occupies a special place among the quantum gases. The hydrogen atom is sufficiently simple to allow its properties and interatomic interactions to be calculated from first principles. Moreover, H is the only gas that can exist in contact with helium coated material walls at temperatures below one Kelvin, where even helium has negligible vapor pressure. At the interface between the liquid helium and the H gas, adsorbed H atoms form a unique two-dimensional quantum gas [4, 5, 6]. As hydrogen atoms obey Bose-Einstein statistics, and analysis has shown that the effective interactions between the adsorbed atoms are weak [7, 8], the adsorbed gas is an experimental realization of the weakly interacting two-dimensional Bose gas. Under conditions where this two-dimensional gas can be made quantum degenerate, it is still in approximate thermal equilibrium with the non-degenerate bulk gas.

The physics of two-dimensional systems may at first glance seem simpler than that of three-dimensional systems, as one has one degree of freedom less to account for. In fact, most field theories are well known to be more subtle and difficult to handle in two dimensions than in any other number of dimensions. There are two main reasons for this: the specific topological properties of two-dimensional space, and the presence of a relatively large number of low-energy states, which causes long-wavelength divergencies in integrals over state space.

In the physics of Bose gases, the two-dimensional system represents an interesting limiting case. In two spatial dimensions, the *ideal* Bose gas does not undergo Bose-Einstein condensation [9]. When the phase space density is increased above $n_2\Lambda^2 = 1$ the distribution function becomes degenerate, i.e., it deviates strongly from the classical Boltzmann distribution, but no condensate is formed. However, the two-dimensional case is a limiting case, and even a very weak external confining potential restores the phase transition for the ideal gas. The behavior of the interacting Bose gas in two dimensions is even more subtle, as the formation of the condensate and the onset of superfluidity are separated.

Superfluidity in two dimensions is usually studied in conjunction with the Berezinskiĭ-Kosterlitz-Thouless (KT) transition [10, 11], which has been widely studied in submonolayer films of ^{4}He [12]. The KT theory predicts that a two-dimensional Bose

fluid becomes superfluid when $n_s\Lambda^2 = 4$. Here n_s is the two-dimensional superfluid density, which is only slightly less than the total density in a weakly interacting system. This prediction has been verified to great precision in helium films. It should be noted that sub-monolayer films of ^{4}He are effectively a rather weakly interacting two-dimensional gas. The KT theory analyzes superfluidity in terms of topological defects in the phase of the local Bose condensate (quasicondensate), but it does not predict anything about the formation of this Bose condensate. Although some work on the theory of the two-dimensional condensate formation exists, it is much less well-explored than the condensate formation in three dimensions. It is predicted that in the condensate both elastic and inelastic processes (recombination) will be reduced. However, predictions of the magnitude of this reduction, and of the behavior in the region around the KT transition temperature vary [13, 14, 15].

Metastable quantum gases, such as H and laser cooled atoms, are well suited for the study of the formation of the Bose condensate. In contrast to helium, these gases can be optically probed, and the decay processes yield additional information on the correlation properties in the gas. Superfluidity is much harder to observe in these systems, and in this sense experiments on adsorbed H are complementary to those in ^{4}He films.

Two-dimensional gases of laser-cooled atoms have only recently been created [16], and their density is presently extremely low. On the other hand, two-dimensional H forms naturally in any experiment where cold H is studied in contact with helium coated walls. High densities can relatively easily be obtained by using H atoms in the stable electron-spin-down state (H$\downarrow$) in a magnetic field (see Fig. 1.1). The H$\downarrow$ atoms have the lowest energy in a high magnetic field, they are therefore called high-field seekers. When the atoms are additionally hyperfine polarized into the "stretch" b hyperfine state (which has no components with electron spin down), the gas can only decay through third order inelastic collisions, and the rate constant for this process is exceptionally small. A gas of H$\downarrow$ atoms in the b state can be compressed to more than 10^{16} atoms per cm^3, a much higher density than is possible for any other quantum gas. At temperatures much below one Kelvin, the density of the two-dimensional adsorbed gas is strongly enhanced, to more than 10^{12} atoms per cm^2. Formation of molecular hydrogen in the dense adsorbed gas then dominates the decay of the system. The heat production associated with this decay (4.5 eV per molecule) is the main obstacle on the road to two-dimensional quantum degeneracy. This heat can be disposed of in an inhomogeneous, 'open' system, where the high densities are obtained only locally [17].

Adsorbed H$\downarrow$ has already been studied for many years using magnetic resonance

methods [18, 19, 20] which are in principle able to directly probe the adsorbed atoms. A drawback of these methods is that they require an homogeneous magnetic field, in which the conditions for two-dimensional quantum degeneracy are hard to fulfill [17]. This problem was circumvented by the use of a cell with an inhomogeneous temperature (cold spot) in an experiment performed in Kyoto [20], and this experiment succeeded in reaching a phase space density of $n_2\Lambda^2 = 0.7$. The density of the gas was probed through the decay processes.

A probing method that is rather indirect, but compatible with strong magnetic compression has been demonstrated in Turku, by Safonov, Vasilyev, Yasnikov, Lukashevich and Jaakkola [21]. These authors probed a two-dimensional H gas in the b-hyperfine state by injecting hydrogen atoms in the reactive a-hyperfine state and analyzing the resulting recombination pulse. Recently, they have observed formation of a two-dimensional Bose condensate by this method [22]. The temperature and density of the adsorbed gas were calculated from the recombination data by inverting a model of the population dynamics in the apparatus, and the formation of the condensate was observed as a reduction of the recombination rate. The magnitude of the observed reduction in recombination is slightly larger than theoretically predicted by Kagan, Svistunov and Shlyapnikov [13], even when taking into account delocalization

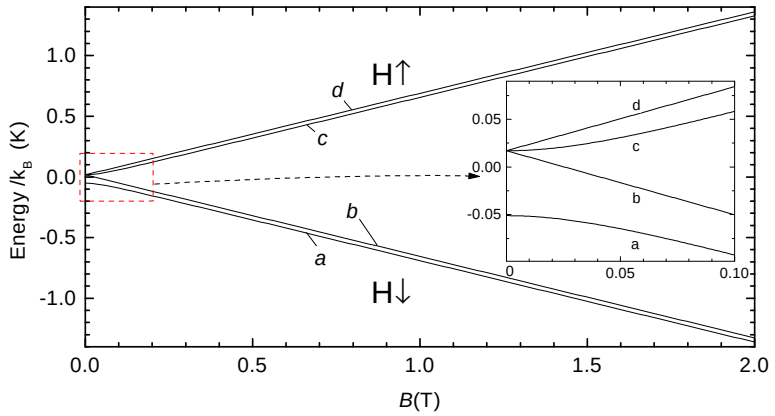

Figure 1.1: Hyperfine states of the hydrogen atom. By convention, these are labeled a, b, c, d by order of increasing energy in small field. The electron spin up (H$\uparrow$) states $c\,(f = 1, m_f = 0)$ and $d\,(f = 1, m_f = 1)$ can decrease their energy by going to lower field, the electron spin down states $a\,(f = 0)$ and $b\,(f = 1, m_f = -1)$ are high-field seeking. The b state is a stretch spin state (both electron and proton spin down), while the lowest energy a state has a field dependent component with electron spin up. See also Table 3.1.3.

of the adsorbed state wavefunction [23]. Still, the reduction is much smaller than that predicted by Stoof and Bijlsma [14].

Clearly, an additional and more direct way of probing the two-dimensional condensate is desirable. Already in 1991, Svistunov, Hijmans, Shlyapnikov and Walraven [24] analyzed the possibility to probe the two-dimensional gas by light-induced fluorescence (LIF), excited by light at the Lyman-α wavelength, $\lambda = 121$ nm. Their analysis shows that it is possible to optically determine the density of the adsorbed gas, and to study the equilibrium between the two-dimensional condensate and the three-dimensional bulk gas. The formation of a condensate leads to an increase by a factor two in density of the two-dimensional gas, due to the reduction in elastic interaction strength [24], see Fig. 1.2. The theory of the LIF lineshape was later extended to negative detuning by Reynolds and Walraven [25]. Although there remained some uncertainty if the predicted optical signals would be strong enough to be usable in practice, these theoretical papers have provided a solid basis for the design of an experimental apparatus.

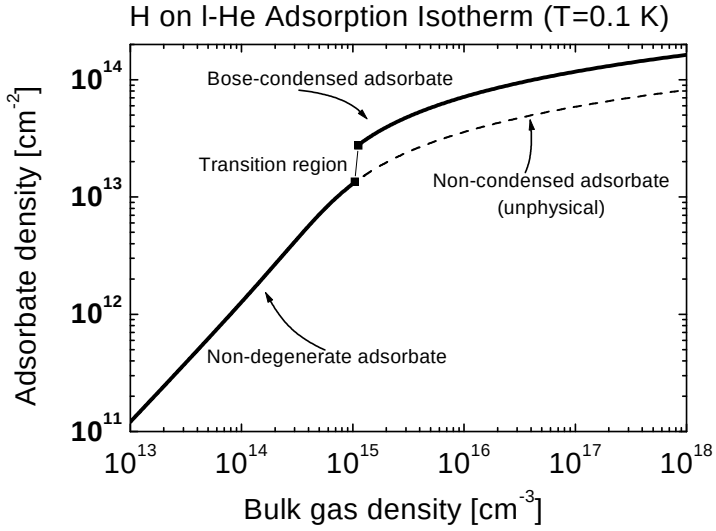

Figure 1.2: Adsorption isotherm which relates the density of the two-dimensional adsorbed H$\downarrow$ gas to that of the three-dimensional bulk gas, for a temperature of 100 mK [24]. The formation of the condensate has a clear signature in this isotherm: a sudden increase in the adsorbate density by a factor two. The behavior in the region where the condensate forms and the KT transition takes place is not well-understood.

1.2 This thesis

In this thesis, I present and discuss the first optical investigation of magnetically compressed H↓, both in the two-dimensional adsorbed state and in the three-dimensional bulk gas. The first measurements of the LIF signal of the adsorbed hydrogen show the signal is strong enough to allow sensitive determination of the adsorbate density, even at densities which correspond to one percent of a monolayer, on a surface area of less than 1 mm^2. The signal of the adsorbed atoms is seen both in transmission and in fluorescence. It is an approximately 300 GHz broad feature which is shifted approximately 300 GHz to the red from the lowest Lyman-α transition of the free atoms. Both the line width and the redshift are reduced upon adding ^{3}He, which lowers the adsorption energy for H atoms. From the optical absorption signal we can infer the density of adsorbed atoms, and from the spectrum of the bulk gas we can deduce their temperature. Using this data we found the highest phase space density reached in the present compression cell was $n_2\Lambda^2 = 0.9$, an encouraging result as improvement is possible. The design of the current apparatus was optimized for spectroscopy, and stronger magnetic compression is possible while maintaining the ability to optically probe the gas.

The Lyman-α optical method is based upon the one used in previous optical studies of atomic hydrogen [26, 27, 28, 29]. Contrary to this work, those studies have focused on hydrogen gas in the low-field seeking (H↑) hyperfine states (see Fig 1.1), which can be confined in magnetic traps [30, 31], and evaporatively cooled to Bose-Einstein condensation (BEC) [32]. The previous optical studies have offered insight into the physics of magnetostatic trapping, and of optical and evaporative cooling of trapped gases. The density in experiments with trapped H↑ is necessarily limited, as the low-field seeking gas suffers from trap loss due to spin-flip collisions.

In the bulk H↓ gas in our compression cell, the density can be raised more than two orders of magnitude above the highest densities reached with trapped H↑. This high density has enabled us to observe photoassociation of hydrogen. Photoassociation is an optical collision process in which two atoms are excited by a photon into an excited molecular state. Obviously, the photoassociation process depends on the number of atom pairs being within range of the excited state potential, and this is proportional to the square of the density. In experiments with trapped H↑, searches for photoassociation have been fruitless, due to a combination of low density, and therefore very small signal, and large uncertainty in the predicted line positions. In H↓, we were able to measure the photoassociation line positions to an accuracy of 1 GHz. The line positions are in agreement with the calculations by Kołos and

Rychlewski of the vibrational levels in the excited $a^3\Sigma_g$ potential. The line width is an indicator of the temperature of the gas, and this may be useful for thermometry of low-temperature H$\downarrow$ in future experiments. The magnetic field dependence of the lines is a sensitive probe for the magnetic moment of the molecule, and we have used it to reveal non-adiabatic effects due to the rotation of the molecule. It is found that the light hydrogen molecule rotates so fast that the electronic wavefunction cannot follow the rotation of the internuclear axis. Corrections to the Born-Oppenheimer approximation (rotational coupling to a nearby $^3\Pi$ state) have to be taken into account to explain the observed magnetic moment. A similar effect has recently been observed in magnetically trapped CaH molecules [33].

1.3 Future

The present experimental apparatus was optimized for observation of the optical signature of the adsorbed atoms. We chose to employ relatively weak magnetic compression, in order to have a large sample of adsorbed atoms and easier optical access. Even in this geometry, we were able to achieve a phase-space density of $n_2\Lambda^2 = 0.9$, on the edge of the degenerate regime. To further increase the phase-space density the compression cell will need to be modified. The results presented in chapters 4 and 5, together with the experimental results of the Turku group, suggest that two-dimensional Bose-Einstein condensation is within reach in our apparatus if a stronger magnetic compression field is arranged.

Stronger magnetic compression will also enable even higher densities, and it might be possible to resolve more photoassociation lines. In addition, some features were seen near the atomic resonances that might be photoassociation lines, but their character has not yet been determined. It should in principle be possible to Zeeman shift a molecular line through the atomic resonance, in which case an excited state Feshbach resonance occurs, leading to extremely high photoassociation probabilities.

A third line along which experiments could be developed is the substitution of deuterium for hydrogen. Preliminary experiments have shown that it is indeed possible to obtain an optical signal from adsorbed atomic deuterium. Atomic deuterium is a much less stable gas than hydrogen, and therefore attaining quantum degeneracy of adsorbed D$\downarrow$ requires even more stringent control of the experimental conditions.

1.4 Outline

Including this introductory chapter, in which a brief overview of the context in which the research was performed is given, this thesis contains six chapters, and an appendix which consists of a table of constants.

In chapter 2 the experimental setup which was used to perform the experiments described in this thesis is described. The cryogenic apparatus, which stabilizes the H$\downarrow$ sample and cools it to a temperature of ≈ 0.1 K, is described in detail, since it is strongly modified with respect to previous experiments. The optical apparatus which generates the Lyman-α light is treated more briefly, as it is similar to that used before in experiments with trapped hydrogen.

Chapter 3 deals with the theory of light propagation in the H$\downarrow$ gas. It is found that most of the numerical methods that were developed for calculating the spectra the relatively dilute H$\uparrow$ samples can be used even in our much denser gas. The corrections due to the high density are analyzed, and turn out to be small. To correctly analyze the optics at high density, the resonant-dipole interaction, which gives rise to long range interaction potentials between ground-state and excited atoms, is discussed. The resonant dipole interaction dominates the physics of pressure broadening, optical collisions and photoassociation in high-density monatomic gases.

The observation of the LIF signal of the adsorbed atoms is discussed in chapter 4. From the LIF spectrum we can determine the density of the adsorbate n_2, and we reach the conclusion that the maximum phase space density reached is $n_2\Lambda^2 \approx 1$. The temperature of the adsorbed atoms is inferred from the adsorption equation. This allows us to determine the temperature dependence of the heat conductance from the helium surface (ripplons) to the helium bulk liquid (phonons).

The population dynamics of the hydrogen atoms in the sample, and the transport of heat in the apparatus are described in chapter 5. It is found that by taking into account the migration of atoms through the apparatus as well as the heat dissipation due to recombination, the behavior of the hydrogen sample can be accurately modeled. The model is then applied to the design of a revised apparatus, and it is shown that according to our model quantum degeneracy can be reached when a compression cell with a smaller effective area is constructed.

In Chapter 6 we discuss the observation of photoassociation that was made in the bulk vapor in our compression cell. Under the influence of Lyman-α light molecules in the excited triplet $a^3\Sigma_g$ state are formed. The molecule formation gives rise to narrow lines in the absorption spectrum, and the subsequent radiative decay is visible in the light induced fluorescence spectrum. The binding energies of these molecules

can be inferred from the line positions, and compare well to *ab initio* theory. The non-adiabatic rotation of the molecule is discussed, and its influence on the magnetic field dependence of the line position is shown. A simple model for the non-adiabatic effects of the rotation of the molecule is developed, and its results agree well with the data. Finally, an analytic expression for the photoassociation lineshape is derived.

Chapters 4 and 6 were published separately, and the introductory matter in these chapters shows some overlap with the rest of this thesis.

References

[1] J. T. M. Walraven, in *Quantum dynamics of simple systems*, proceedings of SUSSP44, ed. G. L. Oppo, S. M. Barnett, E. Riis and M. Wilkinson, (SUSSP publishing, Edinburgh and IOP publishing, Bristol, 1996).

[2] I.F. Silvera and J.T.M. Walraven, *Stabilization of atomic hydrogen at low temperature*, Phys. Rev. Lett. **44**, 164 (1980).

[3] The first Bose condensates were reported in 1995:
M.H. Anderson, J.R. Ensher, M.R. Matthews, C.E. Wieman, and E.A. Cornell, Science **269**, 198 (1995),
K.B. Davis, M.-O. Mewes, M.R. Andrews, N.J. van Druten, D.S. Durfee, D.M. Kurn, and W. Ketterle, Phys. Rev. Lett. **75**, 3969 (1995).
C.C. Bradley, C.A. Sackett, and R.G. Hulet, Phys. Rev. A **55**, 3951, 1997.

[4] D. O. Edwards and I. B. Mantz, *The adsorption of atomic hydrogen to the surface of* ^{4}*He*, supplement **C7** of Journal de Physique **41**, 257 (1980).

[5] J. T. M. Walraven, *Atomic hydrogen and liquid helium surfaces*, in *Fundamental systems in quantum optics*, Les Houches summer school LIII, 1990, ed. J. Dalibard, J. M. Raimond and J. Zinn-Justin, (Elsevier Science, Amsterdam, 1992).

[6] I. F. Silvera and J. T. M. Walraven, *Spin Polarized Atomic Hydrogen*, in *Progress in Low Temperature Physics*, edited by D. F. Brewer (Elsevier, Amsterdam 1986), Vol. 10, p. 139.

[7] Yu. Kagan, G. V. Shlyapnikov, I. A. Vartan'yants, and N. A. Glukhov, *Quasi-two-dimensional spin-polarized atomic hydrogen*, JETP Lett. **35**, 477 (1982).

[8] B. J. Verhaar, J. P. H. W. van der Eijnde, M. A. J. Voermans and M. M. J. Schaffrath, *Scattering length and effective range in two dimensions; application to adsorbed hydrogen atoms*, J. Phys. A **17**, 595 (1984).

[9] P. C. Hohenberg, *Existence of long-range order in one and two dimensions*, Phys. Rev. **158**, 383 (1967).

[10] J. M. Kosterlitz and D. J. Thouless, *Ordering, metastability and phase transitions in two-dimensional systems*, J.Phys. C **6**, 1181 (1973), and *ibid., Two-dimensional physics*, Progress in Low-Temperature Physics **VIIB**, 374 (1978).

[11] V. L. Berezinskiĭ, *Destruction of long-range order in one-dimensional and two-dimensional systems having a continuous symmetry group, I. Classical systems*, Sov. Phys. JETP **32**, 493 (1971), and *II. Quantum systems*, Sov. Phys. JETP **34**, 610 (1972).

[12] D. J. Bishop and J. D.. Reppy, *Study of the superfluid transition in two-dimensional* ^{4}He *films*, Phys. Rev. Lett. **40**, 1727 (1978).

[13] Yu. Kagan, B. V. Svistunov and G. V. Shlyapnikov, *Influence on inelastic processes of the phase transition in a weakly collisional two-dimensional Bose gas*, Sov. Phys. JETP **66**, 314 ,[Zh. Eks. Theor. Fiz **93**, 552], (1987).

[14] H. T. C. Stoof and M. Bijlsma, *Kosterlitz-Thouless transition in a dilute Bose gas*, Phys. Rev. E **47**, 939 (1993),
The influence of the Kosterlitz-Thouless transition on the decay of spin-polarized atomic hydrogen, Physica B **194-196**, 909 (1994).

[15] M. Bijlsma, *Quantum degeneracy in a Bose gas*, Ph.D. thesis, Universiteit Utrecht, 1997 (unpublished).

[16] H. Gauck, M. Hartl, D. Schneble, H. Schnitzler, T. Pfau, and J. Mlynek, *Quasi-2D Gas of Laser Cooled Atoms in a Planar Matter Waveguide*, Phys. Rev. Lett. **81**, 5298 (1998).

[17] Yu. Kagan and G. V. Shlyapnikov, *Bose-condensation of spin-polarized hydrogen in a highly inhomogeneous field*, Phys. Lett. A **130**, 483 (1988),
Same authors and N. A. Glukhov, *The basic role of open systems in attaining Bose condensation in spin-polarized atomic hydrogen gas*, JETP Lett. **41**, 239 [Pis'ma Zh. Eksp. Teor. Fiz. **41**, 197] (1985).

[18] M. W. Reynolds, I. Shinkoda, W. N. Hardy, A. J. Berlinsky, F. Bridges, and B. W. Statt, *Electron-spin-resonance studies of spin-polarized hydrogen on the surface of liquid* ^{4}He, Phys. Rev. B **31**, 7503 (1985).

[19] M. Morrow, R. Jochemsen, A. J. Berlinsky, and W. N. Hardy, *Zero-field hyperfine resonance of atomic hydrogem for* $0.18 < T < 1\,\mathrm{K}$*: The binding energy of* H *on liquid* ^{4}He, Phys. Rev. Lett **46**, 195 (1981).

[20] A. Matsubara, T. Arai, J. S. Korhonen, T. Suzuki, A. Masaike, J. T. M. Walraven, T. Mizusaki and A. Hirai, *Cooling of polarized atomic hydrogen adsorbed on liquid helium*, Proceedings of LT20, Physica B **194-196**, 899 (1994).

[21] A. I. Safonov, S. A. Vasilyev, I. S. Yasnikov, I. I. Lukashevich, and S. Jaakkola, *Magnetic compression of two-dimensional spin-polarized atomic hydrogen* JETP Lett. **61**, 1032 (1995), same authors and E. Tjukanov, LT21, Czech. J. Phys. **46**, 539 (1996).

[22] A. I. Safonov, S. A. Vasilyev, I. S. Yasnikov, I. I. Lukashevich and S. Jaakkola, *Observation of quasicondensate in two-dimensional atomic hydrogen*, Phys. Rev. Lett. **81**, 4545 (1998)

[23] Yu. Kagan, N. A. Glukhov, B. V. Svistunov and G. V. Shlyapnikov, *Collective phenomena in adsorbed* $\mathrm{H}\downarrow$ *phase of limiting density*, Phys. Lett. A **135**, 219 (1989).

[24] B. V. Svistunov, T. W. Hijmans, G. V. Shlyapnikov and J. T. M. Walraven, *Resonant-light absorbtion and the problem of observing the Kosterlitz-Thouless transition in spin-*

polarized atomic hydrogen adsorbed on a liquid-He *surface*, Phys. Rev. B **43**, 13412 (1991).

[25] M. W. Reynolds and J. T. M. Walraven, *Optical excitation of atomic hydrogen adsorbed on liquid helium*, Physica B **194-196**, 905 (1994).

[26] Jom Luiten, *Lyman-α spectroscopy of magnetically trapped atomic hydrogen*, Ph.D. Thesis, Amsterdam, 1993 (unpublished),
O. J. Luiten, H. G. C. Werij, I. D. Setija, M. W. Reynolds, T. W. Hijmans, and J. T. M. Walraven, *Lyman-α spectroscopy of magnetically trapped atomic hydrogen*, Phys. Rev. Lett. **70**, 544 (1993).

[27] Irwan Setija, *Optical cooling of magnetically trapped atomic hydrogen*, Ph.D. Thesis, Universiteit van Amsterdam, 1995 (unpublished),
I.D. Setija, H.G.C. Werij, O.J. Luiten, M.W. Reynolds, T.W. Hijmans, and J.T.M. Walraven, Phys. Rev. Lett. **70**, 2257 (1993).

[28] Pepijn Pinkse, *Evaporatively cooled atomic hydrogen investigated by one- and two-photon optical methods*, Ph.D. Thesis, Universiteit van Amsterdam, 1997 (unpublished),
P.W.H. Pinkse, A. Mosk, M. Weidemüller, M.W. Reynolds, T.W. Hijmans, J.T.M. Walraven and C. Zimmermann, *Resonance enhanced two-photon spectroscopy of magnetically trapped atomic hydrogen*, Phys. Rev. Lett., **79**, 2423 (1997).

[29] Claudio L. Cesar, Dale G. Fried, Thomas C. Killian, Adam D. Polcyn, Jon C. Sandberg, Ite A. Yu, Thomas J. Greytak, Daniel Kleppner and John M. Doyle *Two-photon spectroscopy of trapped atomic hydrogen*, Phys. Rev. Lett. **77**, 255 (1996).

[30] R. van Roijen, J.J. Berkhout, S. Jaakkola, and J.T.M. Walraven, *Experiments with atomic hydrogen in a magnetic trapping field*, Phys. Rev. Lett. **61**, 931 (1988).

[31] Harald F. Hess, Greg P. Kochanski, John M. Doyle, Naoto Masuhara, Daniel Kleppner, and Thomas J. Greytak, *Magnetic trapping of spin-polarized atomic hydrogen*, Phys. Rev. Lett. **59**, 672 (1987).

[32] D. G. Fried, T. C. Killian, L. Willmann, D. Landhuis, S. C. Moss, D. Kleppner and T. J. Greytak, *Bose-Einstein condensation of atomic hydrogen*, Phys. Rev. Lett. **81**, 3811 (1998).

[33] Jonathan D. Weinstein, Robert deCarvalho, Thierry Guillet, Bretislav Friedrich, and John M. Doyle, *Magnetic trapping of calcium monohydride molecules at millikelvin temperatures*, Nature, 395, pp. 148-150 (1998).

Chapter 2

Experimental set-up and methods

To optically study dense and cold atomic hydrogen we basically need only three elements: a tunable light source, a gas sample and a light detector. Unfortunately, for each of these three elements an intricate piece of instrumentation is needed. Narrowband tunable light at the deep-UV wavelengths needed for optical excitation of H can only be generated by a complex laser system. The sample requires a cryogenic environment and a high magnetic field to be stable. The detection of deep-UV fluorescence and transmission is a third nontrivial task. The symbiosis between the cryogenic system and the high power laser setup necessary to generate deep-UV is particularly hard to achieve. A further important requirement on all elements is reliability, since the experiment can only be performed if both the optical and cryogenic systems are working simultaneously. The laser system that generates narrowband Lyman-α light has been developed and used by Luiten, Setija and Pinkse [1, 2, 3] for diagnostics and optical cooling of low field seeking H in traps. Although our requirements on the light source are different, its design is flexible enough to be used in our experiment without major modifications. Since the laser system is described in detail in [3], we will only give a brief description in section 2.3.

In contrast to the laser system, our hydrogen compression cell is completely new, and the cryogenic and magnetic system around it has undergone a major revision. The H$\downarrow$ compression apparatus which prepares and stabilizes the sample is described in section 2.1. The apparatus fits inside the bore of a superconducting solenoid, which is capable of providing a bias field of up to 7 T. This high field prevents depolarization of

the electron spins. It also prevents low field seeking atoms from entering the apparatus and recombining there. Cobalt-iron parts adjust the field profile inside the apparatus, a dilution refrigerator provides the low temperature environment.

The system we use to detect fluorescent light is based on color conversion in an

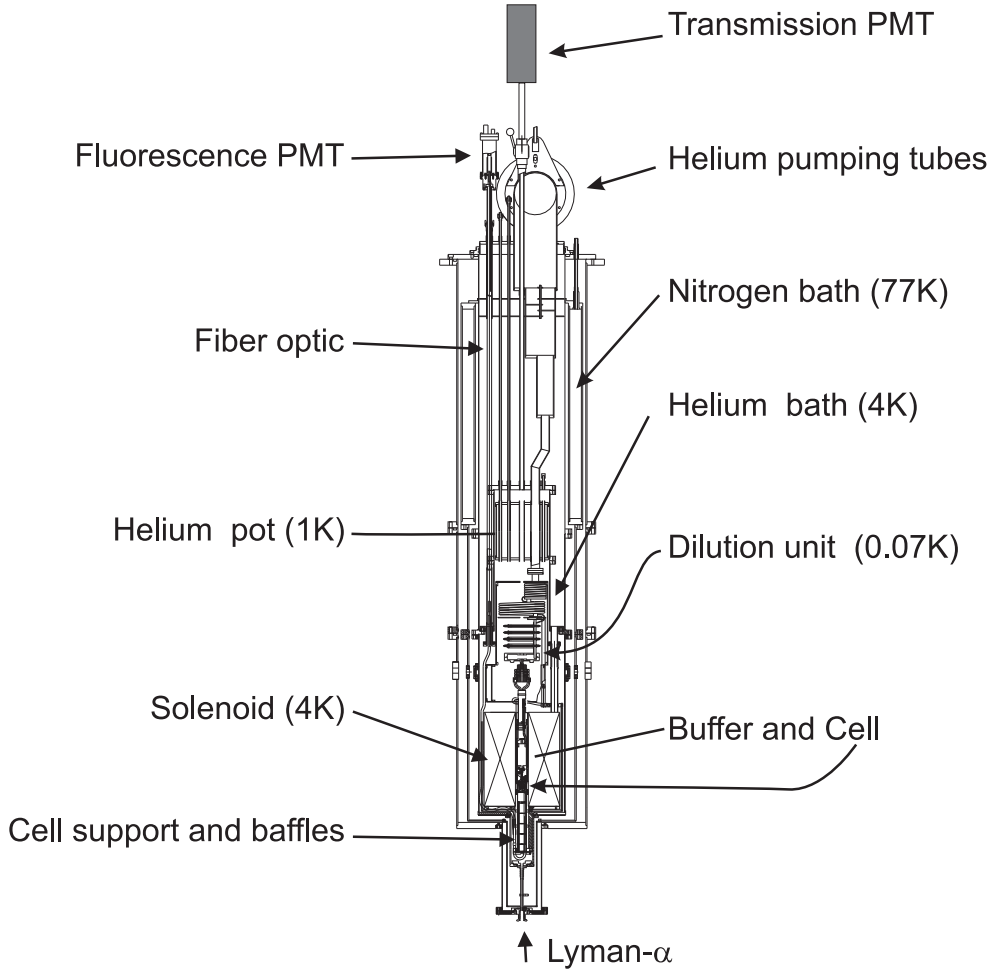

Figure 2.1: The cryostat containing the hydrogen compression apparatus. The setup is 3m high. The Lyman-α light is generated near the bottom of the cryostat and propagates up along the axis of the apparatus, through the inner vacuum can of the cryostat, traversing the hydrogen filled buffer volume and compression cell. Lyman-α fluorescence from the hydrogen atoms in the compression cell is converted to visible light and then guided to the small PMT on top of the cryostat by means of an optical fiber.

organic material. The Lyman-α light is hard to handle, on average there is a loss of 50 % of the intensity per optical element. To avoid these high losses, the scattered Lyman-α is converted to visible light in the cell. The visible light is guided to a room temperature photomultiplier with acceptable losses, see section 2.4.

2.1 Cryogenic Apparatus

To obtain a degenerate gas of two-dimensional H on the surface of liquid helium, a high density has to be reached in combination with a low temperature. Our experiment aims at crossing the KT transition at a temperature $T \gtrsim 100$ mK, where it will occur at a density of 1.3×10^{13} atoms per cm^2. At such a high density, the three body recombination process is important. The three-body recombination constant is $K_{bbb} = 2 \times 10^{-24}$ cm^4/s [4], leading to a lifetime of only 3 ms for an adsorbed atom. To take a Lyman-α spectrum of the system, we typically need several seconds. The atoms lost due to recombination must therefore be replaced to extend the measuring time. If the surface is in contact with a sufficiently large reservoir filled with bulk gas, the adsorbate and bulk will exchange atoms on a time scale comparable to the mean surface residence time τ_a, which can be expressed (for a non-degenerate adsorbate) as [5]

$$\tau_\mathrm{a} = \frac{2\pi\hbar}{s k_\mathrm{B} T} \exp(E_\mathrm{a}/k_\mathrm{B}T), \tag{2.1}$$

where $E_\mathrm{a}/k_\mathrm{B} = 1.01$ K is the surface adsorption energy and s is the sticking probability, for the temperature range of interest $s \approx 0.3\,T$[K] [5]. This leads to $\tau_\mathrm{a} = 0.3$ ms at 100 mK, which is much shorter than the lifetime of the adsorbed atoms, signifying that the atoms stick and desorb many (>10) times before recombining. In this quasi-equilibrium situation surface recombination losses will be compensated by atoms from the bulk gas. As the equilibrium bulk gas density at the KT transition is 10^{16} atoms per cm^3 at 0.13 K, a homogeneously filled spherical volume would need to have a radius of more than 10 cm to maintain a quasi-equilibrium situation for ten seconds. To avoid the construction of such a large volume, one has to either actively compress the hydrogen with moving components, or choose an adequate spatially inhomogeneous setup. We have chosen a setup that employs two H filled reservoirs, a ≈ 0.3 K buffer volume and a 0.1 K compression cell. The compression cell is small, and its effective surface area is reduced further by applying a field gradient, which compresses the H$\downarrow$ so that its density is highest at the bottom of the cell, where it is in contact with a meniscus of bulk liquid helium. The optical system is constructed to probe the sample at this highest density point. In consequence, the adsorbed H

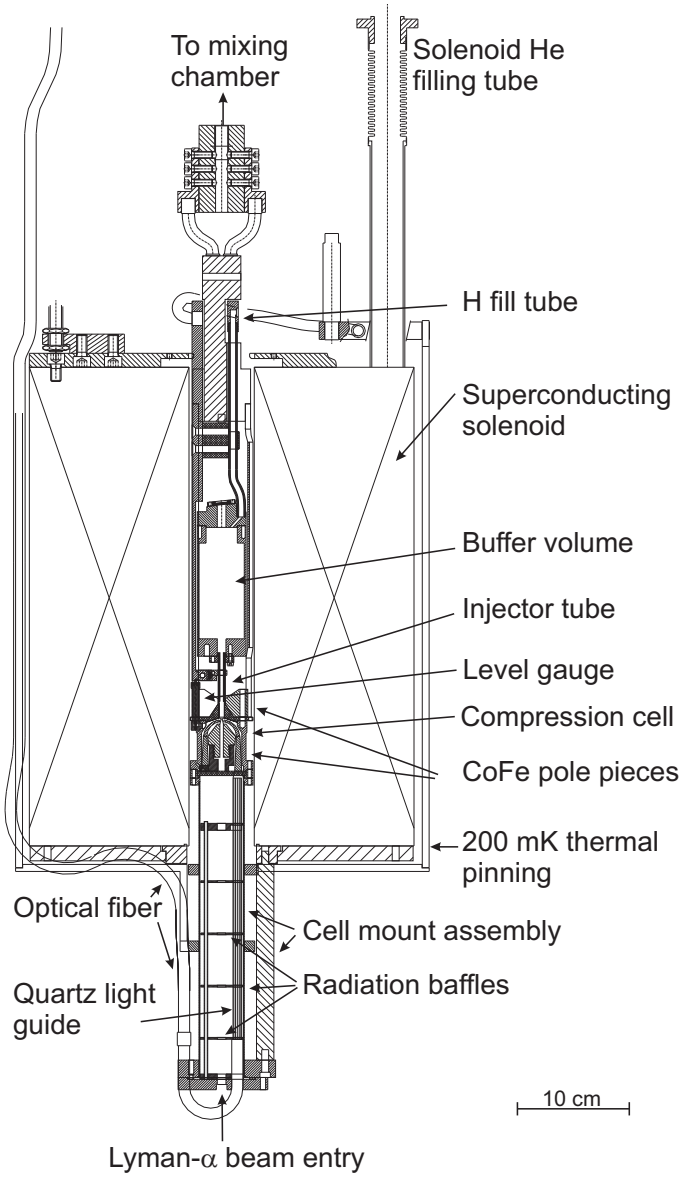

Figure 2.2: The superconducting solenoid containing the core of the apparatus. The optical fiber and the quartz rod guide the fluorescent light from the cell to a room temperature PMT. The cell mount assembly is thermally pinned at 200 and 500 mK. The solenoid operates at 4 K.

recombination is negligible everywhere except at the meniscus. The effective surface area for recombination is ≈ 4 mm^2 for temperatures of interest, see Fig. 5.2. The 30 cm^3 buffer volume stores enough hydrogen to feed a prospective degenerate two-dimensional gas sample for several tens of seconds. The flux of atoms from the buffer volume to the cell is regulated by means of a thermal 'valve': a region of low magnetic field which is present between the buffer volume and the compression cell. For the H$\downarrow$, this region acts as a potential barrier, and the flux of atoms that crosses this barrier depends exponentially on temperature. An injector tube, which is thermally linked to the buffer volume, guides atoms across this barrier. By controlling the temperature of this injector we can directly exert control over the flux of H atoms into the compression cell. Atoms that flow into the cell thermalize to the lower cell temperature and therefore lack the thermal energy to reach the injector and return to the buffer. This leads to a significant thermal compression of atoms into the cell.

The buffer volume and compression cell (Fig. 2.2) reside in the 37.3 mm bore of a (nominally 12 T) superconducting solenoid [6], operated at 4 K. The magnetic field of this solenoid, which we typically used at 7.5 T, keeps the electron spins of the H polarized. A cryogenic discharge is run to dissociate H_2 molecules, this dissociator is placed in the fringe field of the superconducting solenoid. The high field seeking atoms are guided into the buffer volume by a copper tube, the low field seeking atoms can diffuse towards lower field into the H_2 filling tube, where they recombine on the walls. Under optimal conditions a flux of 10^{13} atoms per second arrives in the buffer volume. The buffer volume provides an environment that is optimized for stabilizing H$\downarrow$. Its inner walls are fully wetted with a film of superfluid helium, which reduces surface adsorption and subsequent recombination, and its temperature is typically 0.3 K. This temperature is low enough for depolarization of the electron spins in thermal collisions to be negligible, but high enough so that only a small fraction of the atoms is adsorbed to the walls. Magnetically pure materials are chosen for the walls beneath the helium film, in order to prevent relaxation of the nuclear spins.

2.1.1 Magnetic compressor

The superconducting solenoid provides a bias field to separate the H$\downarrow$ from the H$\uparrow$ and to prevent depolarization of the electron spins. This bias field is smooth and varies only little over the volume of the buffer volume and compression cell. Magnetic pole pieces are used to create the field gradients needed in the experiment. These pieces are made of a cobalt-iron (CoFe) alloy [7], which is a soft ferromagnetic material with a saturation magnetization $\mu_0 M = 2.35$ T. The CoFe is driven into full saturation by

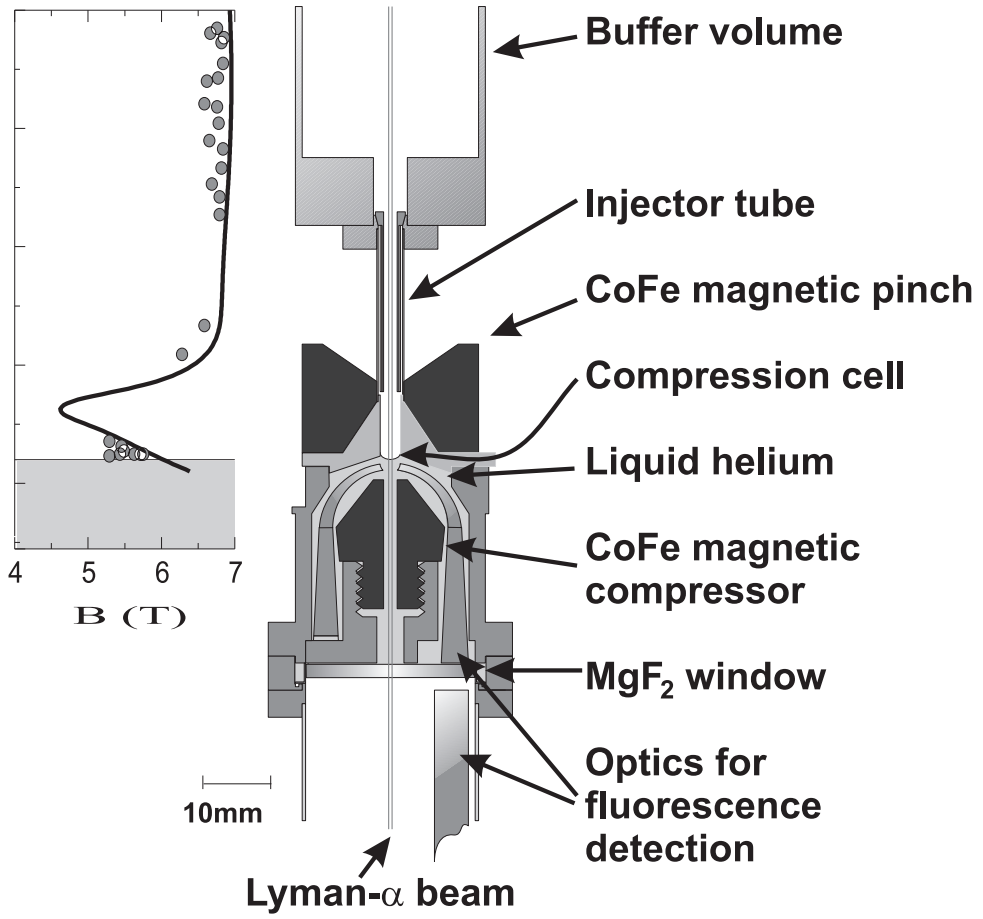

Figure 2.3: The compression cell and bottom half of the buffer volume.

the field of the superconducting solenoid, its magnetization is aligned to the applied field. The use of CoFe to modify the field profile has some advantages over the use of small superconducting coils: the material can easily be machined in almost any shape, it cannot quench and it does not require wiring. The force the solenoid exerts on the pole pieces is considerable (1500 N, directed upwards). For this reason, they are fixed relative to the solenoid's frame by a rugged support construction. Since the CoFe pieces are at a much lower temperature than the solenoid, the supports are long (to reduce thermal conduction) and adequate thermal pinnings are in place to intercept the heat-load. The wires of the solenoid also experience a force due to the field of the CoFe. This force is mostly directed vertically (downwards). The wires normally

experience mainly radial forces. The extra forces cause the solenoid to quench at a current below its critical current, although the critical field of the wires is not exceeded anywhere. To investigate this effect, and to remove it by *training*, we performed a separate cooldown. Training is the phenomenon in which a superconducting magnet can operate at higher currents after the occurrence of a quench. Probably, training occurs due to shifts of components of the magnet system relative to each other . In the training run no cell was present, but only the CoFe pieces, their supports and a magnetometer. During the first ramp up of the field we found the solenoid to quench at 6 T in presence of the CoFe. After this one training quench, the solenoid was able to reach the desired field strength of 7.5 T.

Field profile calculation

The soft ferromagnetic CoFe pieces experience an external field which is much larger than the field needed to saturate them, therefore their magnetization will be equal to the saturation magnetization of the material. Since the applied field is also larger that the field corresponding to the magnetization of the material, the direction of the magnetic field lines inside the material remains predominantly vertical. Therefore, we can assume the pieces to be magnetized uniformly in the vertical direction. Numerical calculations of the field profile support this assumption. The field due to a piece of uniformly magnetized material can be calculated by integrating the field due to the bound surface current density $\mathbf{K}_b$ [8, 9]:

$$\mathbf{K}_b = \mathbf{M} \times \hat{n}. \tag{2.2}$$

Here, $\hat{n}$ is a unit vector normal to the surface, and $\mathbf{M}$ is the magnetization vector. A thin disk of radius a and thickness Δh that is magnetized perpendicular to its surface will act as a current loop with $I = \mathbf{K}_b \Delta h$. The field on the axis of such a current loop can be found from the Biot-Savart law,

$$B_z(z) = \frac{\mu_0 I a^2}{2(a^2+z^2)^{3/2}} = \frac{\mu_0 M(\Delta h) a^2}{2(a^2+z^2)^{3/2}}. \tag{2.3}$$

The ferromagnetic pole pieces in our apparatus can be decomposed for calculational purposes into a stack of conical disks (see Fig. 2.4). The field due to the conical disk shown in Fig. 2.5 can be found by in turn decomposing it into infinitely thin disks and then summing over the contributions from these disks, leading to the integral

$$\begin{aligned} B_z(z) &= \frac{\mu_0 M}{2} \int_0^h dh' \, \frac{(\rho_1 + t h')^2}{((\rho_1 + t h')^2 + (z_1 + h' - z)^2)^{3/2}}; \\ & \quad h = z_2 - z_1 \, ; \, t = (\rho_2 - \rho_1)/h. \end{aligned} \tag{2.4}$$

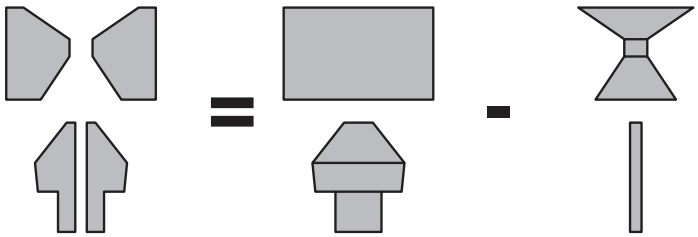

Figure 2.4: The shapes of the pole pieces can be decomposed into conical disks. The field due to each conical disk is expressed analytically, see Eq. (2.5).

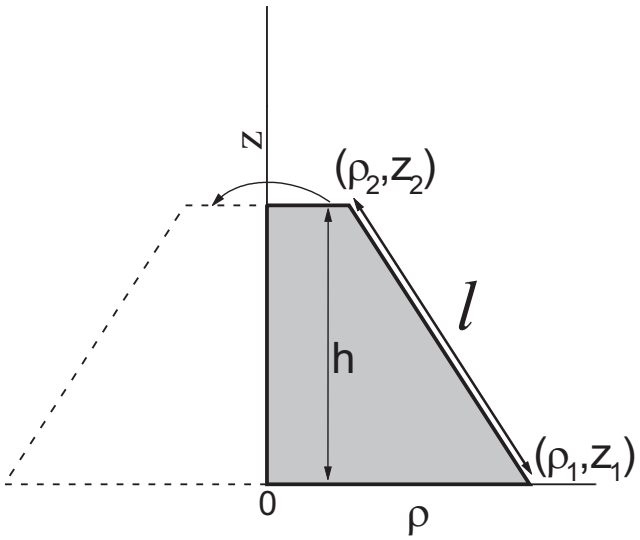

Figure 2.5: One conical 'slice' of the CoFe pole; the shape is revolved around the z axis.

The integral can be evaluated to give

$$B_z(z) = \frac{\mu_0 M}{2s^2}\left[\frac{\tilde{z}_1 - t\rho_1}{r_1} - \frac{\tilde{z}_2 - t\rho_2}{r_2} + \frac{t^2}{s}\ln\left(\frac{\tilde{z}_1 + r_1 s + \rho_1 t}{\tilde{z}_2 + r_2 s + \rho_2 t}\right)\right] \tag{2.5}$$

with the substitutions

$$\begin{aligned} \tilde{z}_{1,2} &= z_{1,2} - z, \\ r_{1,2} &= (\tilde{z}_{1,2}^2 + \rho_{1,2}^2)^{1/2}, \text{and} \\ s &= t(1 + t^{-2})^{1/2}. \end{aligned}$$

This simple expression can be evaluated for each of the sides of the iron pieces to obtain the field profile in the apparatus.

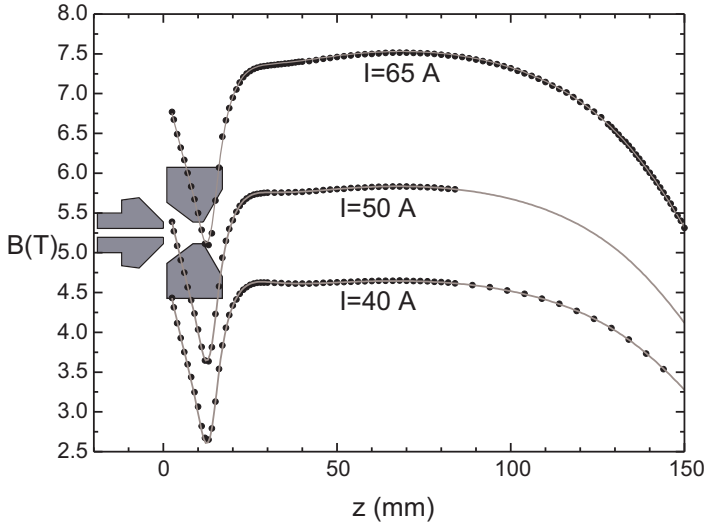

Figure 2.6: Magnetic field profile in the cell. We have fitted calculated profiles (lines) to the data (points) to verify the saturation magnetization and the relative positions of the elements.

The field profile was checked during the training run, using a semiconductor Hall probe (Siemens KSY 14) on a translator stick, which could be controlled from its room temperature end. The Hall probe was read using an AVS47 ac resistance bridge, and the Hall coefficient was determined by calibrating the probe in the field of the solenoid, far away from the CoFe pieces.

Figure 2.6 shows the measured field profile for a number of solenoid currents. The measured profile was found to agree very well with the calculation. We used the measurements to verify the position of the elements relative to the center of the solenoid and to determine the saturation magnetization of the CoFe.

2.1.2 Buffer volume

The buffer volume is designed to hold a large number of atoms which accumulate when the dissociator is running. It has an interior volume of 32 cm^3. Since the field inside the buffer volume is slightly inhomogeneous its effective volume for holding H$\downarrow$ atoms is temperature dependent (see Fig. 5.2). Typically we reach densities of $n_B = 10^{15}$ atoms per cm^3 in the buffer volume, corresponding to 3×10^{16} atoms in total. The flux of atoms from the buffer volume into the compression cell can be controlled sensitively during the actual experiment by heating the buffer volume

and the injector tube. The effusive flux $\Phi_{B\to C}$ of atoms from the buffer volume into the compression cell is exponentially dependent on the temperature T_B of the buffer volume,

$$\Phi_{B\to C} = \frac{1}{4} K^* \bar{v} A_{\rm inj} n_B e^{-\mu_B (B^{\rm buf}_{\rm max} - B^{\rm inj}_{\rm min})/k_B T_B}, \tag{2.6}$$

where $B^{\rm buf}_{\rm max} - B^{\rm inj}_{\rm min} \approx 2.5$ T is the difference between the maximum field in the buffer volume and the field minimum, $A_{\rm inj} = 3.14$ mm^2 is the cross section of the injector tube, and $\bar{v}$ is the thermal speed of atoms in the buffer volume (see Eq. A.2). The effective Clausing factor $K^* \approx 0.5$ is discussed below eq. 5.28 on page 90. The flux of atoms that arrives in the compression cell when the buffer volume is suddenly heated can be very high, at $n_B = 10^{15}$ cm^{-3}, $T_B = 0.4$ K we find $\Phi_{B\to C} = 10^{15}$ atoms per second, i.e. two orders of magnitude higher than the dissociator flux.

During dissociation the temperature of the buffer volume is kept relatively low so that only a small flux of atoms goes to the cell. The dissociator produces atoms in the a and b state, but since the a atoms recombine more efficiently [10], the gas becomes polarized in the b state. Relaxation of the spins is reduced by a careful choice of wall materials [11]: the buffer volume was machined out of a block of very pure copper, and after machining the copper was etched in dilute nitric acid to remove possible iron impurities. A Kapton [12] film was glued (using Stycast 1266 epoxy) to the inside of the buffer volume to reduce its effective surface area with a non-magnetic material. Kapton has a very smooth surface. Once it is covered by a helium film we may assume that the effective surface area of the buffer volume for adsorption of H atoms approaches the geometrical surface area [13], which is 60 cm^2. The buffer volume is weakly thermally linked to a ≈ 0.2 K heat exchanger in the dilution unit and temperature stabilized at temperatures between 0.17 and 0.4 K. Above 0.4 K the buffer volume cannot be used as the fountain effect causes dripping of helium from the injector tube into the compression cell. At low temperature, the fountain effect in superfluid helium can be viewed as radiation pressure on the helium surface due to excitations in the liquid. The low-energy part of the excitation spectrum in the liquid is purely phonon-like, and this leads to a fountain pressure [14, 15] of $P_{\rm fount} = (251\,{\rm Pa\,K^{-4}})T^4$, equivalent to a gravitational head of

$$\frac{P_{\rm fount}}{\rho g} = (0.177\,{\rm m/K^4})T^4. \tag{2.7}$$

The liquid helium is slightly diamagnetic (with a magnetic susceptibility of $\chi_m/\mu_0 = -0.69\,{\rm Pa\,T^{-2}}$), in the strong field gradients in the cell gravity is effectively reduced by $\approx 20\%$ (this diamagnetism has been used to levitate droplets of liquid helium, in geometries involving even stronger field gradients).

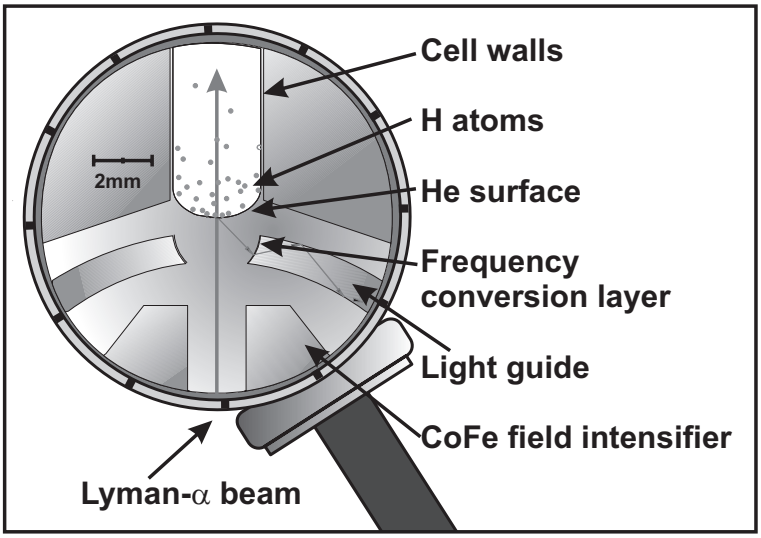

Figure 2.7: Detail view of the compression cell showing the helium meniscus and the hydrogen atmosphere. The fluorescent light is frequency converted to visible wavelength by a thin layer of TPB at the surface of the quartz light guide, see section 2.4.

When we raise the temperature of the injector above 0.4 K, the local equilibrium pressure on the helium film will become positive and drops of helium will grow at the end of the injector. These droplets then fall into the compression cell, causing the helium surface to oscillate. This causes spurious noise on the transmission spectra. In case ^{3}He is present, the fountain effect may be aggravated: ^{3}He quasiparticles give rise to an extra osmotic pressure contribution that adds to the fountain pressure [16].

2.1.3 Compression cell

In the compression cell the H is in contact with a cold helium surface (T$\approx$ 0.08 K). The substrate is bulk superfluid helium, which has the key advantages that its thermal conductivity is superior to any other material, it is transparent to Lyman-α and it provides a magnetically pure environment for the adsorbed H. In addition, long range substrate effects on the H adsorption behavior can be ruled out [17]. A bulk liquid substrate has some disadvantages too, most importantly it cannot be constructed at room temperature and the position of its surface must be determined during the experiment. The procedure used for this is outlined in section 3.6. A second disadvantage is the possibility of sloshing due to mechanical vibrations or due

to the fountain effect. To prevent this sloshing, mechanical vibrations in the cryostat have to be minimized and the temperature of the buffer volume must be kept below 0.4 K, or even lower if ^{3}He is present (see section 2.1.2).

The cell bottom, which is filled with superfluid helium, contains the CoFe magnetic field intensifier and the fluorescence detection optics, see Fig. 2.7. A thick copper heat conductor connects the cell to the mixing chamber of the dilution refrigerator. To ensure good thermal contact between the liquid and the cell housing a few mm^3 of silver sinter is present. Two resistance thermometers are mounted on a Kapton support disk inside the liquid. During many of the experiments, one of these was used as a heater, permitting quick manipulation of the helium temperature.

To check the helium level in the cell a capacitive level gauge is present. The capacitance of this coaxial capacitor will change as it fills up with liquid helium. It is part of a tunnel diode oscillator [18], the frequency of this oscillator is inversely proportional to the capacitance of the level gauge. The absolute accuracy of this gauge is not good enough to use it to determine the correct position of the helium level, but it can be used to simplify filling the cell with helium. The absolute position of the helium meniscus was inferred from the hydrogen spectra, as described in section 3.6.

2.1.4 Cell optics

The windows that permit the Lyman beam to enter the apparatus require a carefully designed mount in order to be reliable at low temperatures. The only suitable window materials are single crystals of magnesium fluoride (MgF_2) and lithium fluoride (LiF), the latter being an impractical choice as this material is both very brittle and hygroscopic. Magnesium fluoride is much tougher and although it is described in the literature [19] as weakly hygroscopic, we never observed any degradation due to atmospheric water vapor under normal laboratory conditions. The contraction upon cooling of magnesium fluoride is smaller than that of the materials of the cell body (copper and stainless steel). Moreover, it is anisotropic. In previous experiments indium seals were used to seal windows of a diameter up to 10 mm. This technique was also used for the small window on top of the buffer volume. To ensure maximum reliability, small steel springs were inserted under the screws that compress the indium seal. Thermal contractions can then be compensated by the spring while the indium remains under compression. The window is not horizontal, it is mounted at an angle to eliminate the possibility of a window reflection ($\approx 10\%$ of the beam) giving stray light on the fluorescence detector.

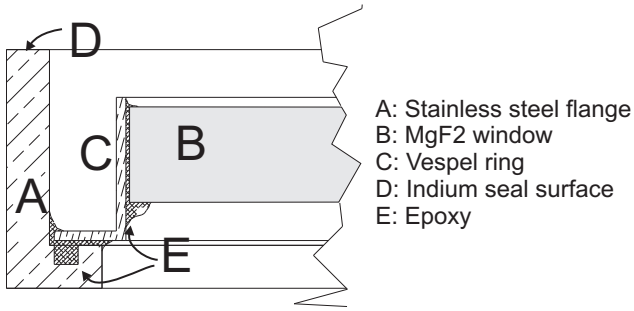

Figure 2.8: Window mounting flange designed to reduce stress on the single crystal window when cooling down.

The lower window, with a diameter of 25 mm, cannot be reliably sealed in a rigid construction, as we found in preliminary tests of the apparatus. Its radial thermal contraction is strongly mismatched from the steel flange that surrounds it. Differential thermal contraction normal to the window surface can be compensated for by inserting a calibrated thickness of indium so that the average contraction of magnesium fluoride plus indium just equals that of the steel flange, but radial differential contraction cannot be sufficiently compensated. A very thin window holder made of a flexible material was designed to cope with the strain due to differential thermal contraction. It is important that no components of the cell deform inelastically as this will cause leaks upon thermal cycling. Furthermore, the stress on the MgF_2 optics should be low, and it should never be negative, as the crystal will cleave. We used the polymeric material Vespel SP-1 (unfilled polyimide), which remains relatively flexible down to low temperatures. A mounting ring with a thickness of 0.2 mm was machined to fit around the window, and a filled epoxy with a low thermal coefficient of expansion (Stycast 2850 GT) was used to glue the window in the ring, and the Vespel to the steel window flange (see Fig. 2.8). Contamination of the optical surfaces of the window during the curing of the epoxy was prevented by temporarily coating them with a removable polymer film [20]. No degradation of the Lyman-α transmission was observed. An important disadvantage of the use of Vespel is that it is permeable to helium at room temperature, which hampers leak detection. Fortunately, this permeability disappears upon cooling. Leaktesting of the cell was carried out by cooling it in a helium atmosphere inside a simple test cryostat. In this test, silicon diodes were used as simple thermometers. It was found that at a temperature of 150 K the helium diffusion rate becomes too small for our leak detector to detect, i.e. less than 10^{-10} ml(NTP)/s. To test for a possible superleak, we immersed the cell in

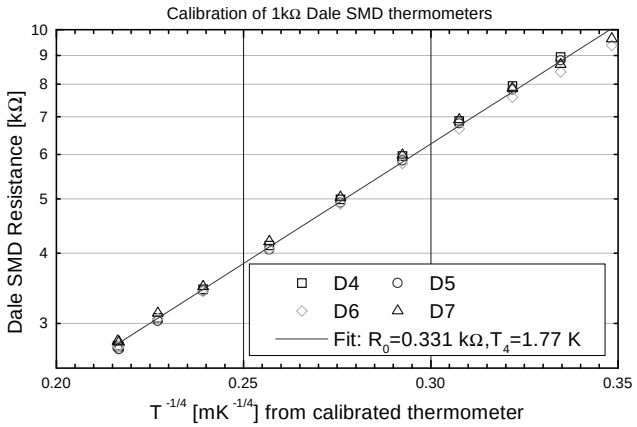

Figure 2.9: Resistance of Dale miniature resistors vs. temperature. The temperature is determined by a resistance thermometer which has been calibrated against the ^{3}He melting line. Due to the age of this calibration, a ± 5 mK drift cannot be ruled out.

superfluid helium, no helium was detected even after several minutes.

2.1.5 Thermometry

Although the temperature of the H gas in the cell is determined from the optical spectrum, many other relevant temperatures, like that of the bulk helium and that of the dense H gas in the buffer volume, cannot be obtained in this way. In our experiments, a highly accurate measurement of these temperatures is not required. Resistance thermometers are well suited as they are small, relatively easy to read out, and very sensitive at dilution refrigerator temperatures. We used surface mounted device (SMD) miniature thick film resistors made by Dale electronics [21] to monitor the temperatures of the buffer volume and the helium in the compression cell. Two of these resistors were glued to a Kapton foil that was suspended in the cell, well below the liquid level, while one was glued to the outside of the buffer volume. Four more were on a Cu pole that was attached to the mixing chamber, together with a pre-calibrated carbon resistor. All resistance thermometers were read out using a four point AC bridge technique [22], dissipating less than a pW in the sensors, and all thermometers were wired using thin superconducting wires. The production

process of the Dale SMD resistors is extremely well-controlled so that differences in composition between resistors are minimal. The resistance of these thermometers has been found to follow [23]

$$R(T) = R_0 \exp[\left(\frac{T_4}{T}\right)^{1/4}], \tag{2.8}$$

where R_0 and T_4 are phenomenological constants that may differ slightly between batches of resistors, but are expected to be the same within one batch. To determine the values of R_0 and T_4 for our batch, we measured the resistance of the four resistors on the Cu pole at various temperatures (see Fig. 2.9). We obtained $R_0 = 331(1)\,\Omega$; $T_4 = 1.77(1)$ K, while for the resistor in ref. [23] it was found that $R_0 = 438\,\Omega$; $T_4 = 1.11$ K, calibrated in a slightly wider temperature range.

We avoided a time-consuming calibration run by relying on batch calibration curves. The thermoresistance curves of different resistors in the same batch are expected to be very similar. We have used uncalibrated resistors as temperature sensors in the buffer volume and compression cell, and to obtain an indication of the absolute temperature we calibrated four other resistors from the same batch against a pre-calibrated carbon-glass resistor. The calibrations were done during the same cooldown as the actual experiment. The four calibration resistors were found to display the expected uniform behavior, from which we inferred the above values for R_0 and T_4. We may, with caution, assume that this calibration curve holds for all resistors from this batch.

The two resistors in the cell showed a different resistance at low temperature (see Fig. 2.10). The thermoresistance curve is very steep in this temperature regime, so that a small temperature difference could already explain this behavior. However, these two resistors are close together in a superfluid helium filled cell, therefore they must be at the same temperature, and apparently the thermoresistance of at least one of them deviates. Since the cell is far away from the calibration thermometers, we cannot know its absolute temperature, and we have no information as to which of the cell thermometers deviates from the batch behavior. In principle, it is possible for both cell thermometers to deviate from the batch behavior, but this is very unlikely. The best guess of the cell temperature is the average value of the inferred temperatures for the two thermometers, and an extra calibration uncertainty has to be accepted. The inferred temperatures are different by only 3.1 mK at temperatures of interest (0.08 K), this is of the order of the possible calibration error of the carbon-glass reference resistor we used. The additional calibration uncertainty is therefore 1.6 mK, and the total calibration uncertainty is estimated to be 5 mK. The thermometer of the buffer

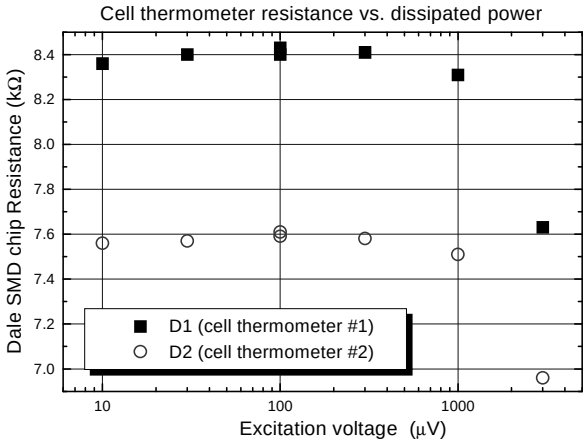

Figure 2.10: Resistance of the two cell thermometers (Dale resistors) vs. excitation voltage of the AC resistance bridge. The helium temperature is kept constant during the experiment. The power dissipated in the sensor is roughly $V_{\rm exc}^2/R$, which is $\approx$ 1 nW at the maximum excitation voltage, this does not significantly heat the helium bath although the sensor is measurably heated.

volume is subject to the same calibration uncertainty.

Either of the compression cell thermometers can be used as a heater, while the other is used to form a feedback loop to a temperature controller. This way the compression cell temperature can be regulated to within 2 mK. However, since the cell is quite strongly linked to the mixing chamber it is not possible to cool the system rapidly if the cell has been heated for a while, as the dilution unit will be too warm. The buffer volume also has a heater attached to it so that its temperature can be regulated by a second temperature controller. The buffer volume is more weakly thermally linked, therefore it can be heated without disrupting the operation of the dilution refrigerator.

2.2 Isotopic purification of ^{4}He

The fluorescence detector and the magnetic pole piece inside the cell are submerged in superfluid helium. Approximately 4 cm^3 of liquid is present in the cell corresponding to 3 liters of gas at NTP. To be sure the atoms interact with a ^{4}He surface, the helium

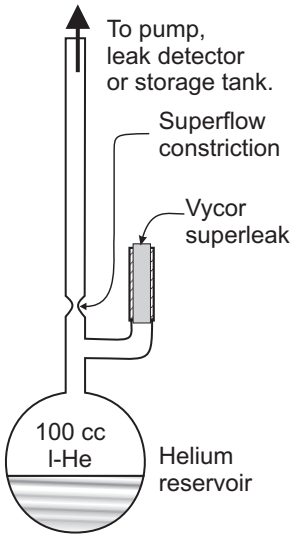

Figure 2.11: The helium purification apparatus. The apparatus is made out of glass, the Vycor superleak is held in a brass tube. The apparatus is inserted in a glass cryostat which is filled with commercial purity ^{4}He to a level above the superleak.

must be isotopically purified. Commercial helium contains about 0.5 ppm of ^{3}He. Since at low temperatures the ^{3}He will accumulate on the surface this concentration is too high. The cold surface in our cell is of order 50 mm^2 in size. A monolayer of ^{3}He on this surface area is reached at $\approx 6.4 \times 10^{14}$ atoms/cm^2 [16], that is 3×10^{14} atoms. This corresponds to about 1×10^{-5} cm^3 of gas at NTP, or about 4 ppb of the helium charge in our cell. It was found in earlier experiments [5] that a coverage of a fraction of a monolayer will not perceptibly change the way the H interacts with the surface. We only need to reduce the impurity by slightly more than three orders of magnitude to have a well-defined adsorption energy.

We built a superleak helium purifier, based on a design by Fatouros *et al.* [24]. Below 2.17 K, ^{4}He is superfluid – it can then flow without resistance through a porous material. A porous material can be modeled as a bundle of thin tubes [25]. The normal flow rate through such a system is inversely proportional to its length, the superfluid flow is independent of length and depends only on the temperature. If the temperature is low enough, the flow of superfluid ^{4}He can be very high while ^{3}He impurities will pass through the porous material only diffusively. The purification apparatus, shown in Fig. 2.11, consists of a superleak made from Vycor porous glass and a glass bulb to collect the purified liquid. Once superfluid helium is collected inside, it will creep up

the glass tube that leads to the room temperature gas handling system, evaporate from the hot walls higher up and heat the collected liquid. To prevent this heating, the tube contains a flow constriction (area with smaller tube diameter). This reduces the flow of the superfluid film, since the critical flow is proportional to the smallest perimeter in the system. As a bonus, the flow constriction also reduces the reflux of hot gas into the cold part of the apparatus. The apparatus is made out of glass so that the helium level can be checked visually. At room temperature, helium diffuses in at a rate of 1.5×10^{-5} ml(NTP)/s. Upon cooling down and filling the cryostat with normal helium at 4K, the detected helium diffusion remains of the same order. When we pumped the cryostat, the helium outside the purifier became superfluid. However, no increase in the amount of helium vapor was detected by the leak detector. Only after ≈ 20 minutes the leak detector detected large amounts of helium vapor and liquid began to fill the bulb. It took 15 more minutes to fill a substantial fraction of the bulb. A probable explanation for this long time delay is the following: The adsorption energy of helium to the channels in the Vycor heats the system locally. Heat is transported diffusively in Vycor, therefore it takes some time for the whole superleak to cool down to below the critical temperature. From the ratio between the normal flow rate and the superflow rate we estimate a purification factor of $> 10^5$, taking into account that the normal flow continued for some minutes after the temperature was raised above the Lambda point. The purified liquid was evaporated and the vapor was stored in a ^{3}He-free container, from which the cell was filled later.

2.3 The Lyman-α source

The Lyman-α transition of the hydrogen atom at $\lambda = 122$ nm lies in the vacuum ultraviolet (VUV). Radiation in this part of the electromagnetic spectrum does not propagate through air. Neither lasers nor efficient second harmonic generation schemes are available for this range of wavelengths, which complicates spectroscopy. We generate narrowband tunable light in this wavelength region using pulsed third-harmonic generation in krypton. This scheme may have the disadvantage of being inefficient, but it is very reliable. As an off-resonant method it is probably the easiest way to generate widely tunable narrowband VUV.

2.3.1 Vacuum ultraviolet generation

We produce light at 122 nm by frequency tripling of UV laser pulses. These narrowband UV pulses are in turn generated by frequency doubling of a 729 nm laser

source, in the setup shown in Fig. 2.12. A stabilized, tunable continuous wave (CW) titanium-sapphire laser at 729 nm provides a seed frequency for the laser pulses. This CW laser can be tuned over a range of 30 GHz and its frequency is calibrated using a stable reference cavity to provide a frequency accuracy of better than 30 MHz. Its output power is $0.3 - 0.5$ W. The light from this laser is amplified in a three-stage pulsed dye amplifier (PDA). This amplifier is pumped by a 100 MW XeCl excimer laser, and delivers 20 ns pulses. It is typically used at a repetition rate of 10 Hz for optimum signal to noise. The amplified 729 nm pulses are frequency doubled in a KDP (potassium di-hydrogen phosphate) crystal, and the resulting 365 nm UV pulses are amplified in a fourth PDA stage. The amplified UV pulses have an energy per pulse of typically 15 mJ. The intense UV pulses are focused into the tripling cell

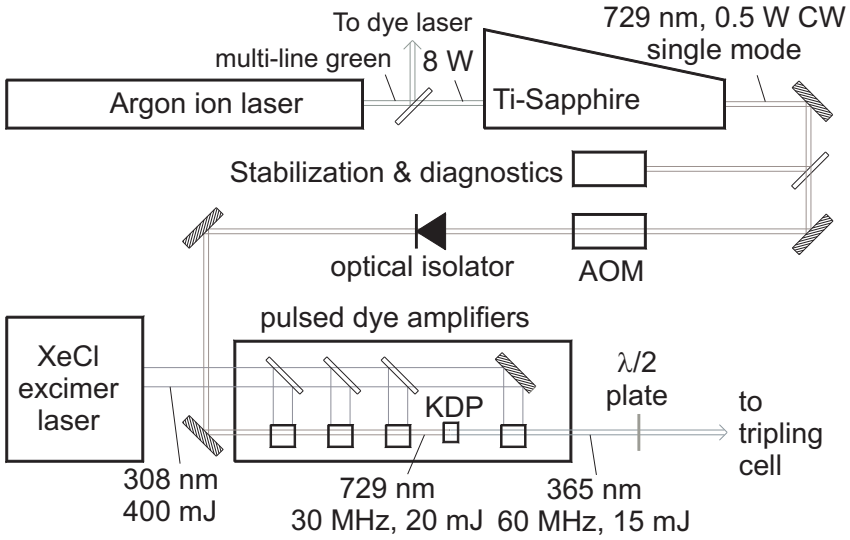

Figure 2.12: Optical set-up to generate the 365 nm light, which is used as an intermediate frequency in the Lyman-α source. The typical energies and bandwidths of the pulses are indicated.

which contains a mixture of krypton and argon. The krypton has a high third-order susceptibility, enabling frequency tripling, and the presence of argon prevents the dispersion in the krypton gas from causing destructive interference between the third harmonic light generated at different positions in the beam path (phase matching [26]). Typically 10^{10} VUV photons are generated per pulse, but most of this power is dissipated in the optics, as each optical element absorbs approximately half of the incident light. A lens at the exit port of the tripling cell focuses the VUV beam onto

the H sample in the cryostat, where approximately 5×10^7 photons per pulse arrive.

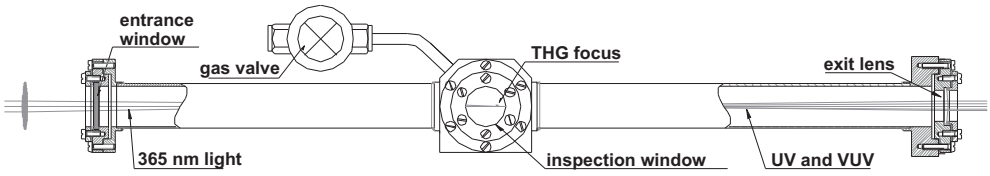

Figure 2.13: Drawing of the tripling cell. The UV enters from the left, the right side of the tripling cell attaches to the monochromator. The MgF_2 exit lens refocuses the Lyman-α beam.

2.3.2 VUV monochromator and beam steering

The 122 nm light produced in the Kr/Ar cell is copropagating with a fundamental beam that is ten million times more intense. It is absolutely necessary to separate these beams since the 365 nm light would otherwise heat our sample cell and saturate our detectors. This separation is accomplished by a monochromator consisting of two magnesium fluoride prisms, shown in Fig. 2.14. The monochromator is kept under a low pressure of Ar to prevent contamination of the VUV optics by materials ablated from the walls by the intense UV light. The second prism can be used to overlap a visible light beam with the VUV. The main purpose of this feature is to enable two-color spectroscopy, such as resonance enhanced two-photon spectroscopy (RETS, see section 3.6.2 and Ref. [3]). The ability to accurately overlap a visible light beam with the VUV is also extremely valuable for alignment purposes. About 10% of the VUV light is reflected by the second prism, this light is detected by a reference detector, which is insensitive to 365 nm and visible light ('solar blind'). The signal from this detector is used to monitor VUV production. Pulse to pulse fluctuations of the excimer laser are high, of order 10%. We reduce the noise on our spectra by up to a factor 10 by dividing the transmission signal by the VUV reference signal. After this division signal to noise is no longer limited by the pulse to pulse fluctuations, but by mechanical oscillations of the helium surface (for the transmission signal) and by shot noise (for the fluorescence signal).

2.3.3 Double seed laser operation

The frequency of the Lyman-α light can be scanned by varying the frequency of the CW laser. This laser, a Coherent 899-21 titanium-sapphire laser, is tunable over

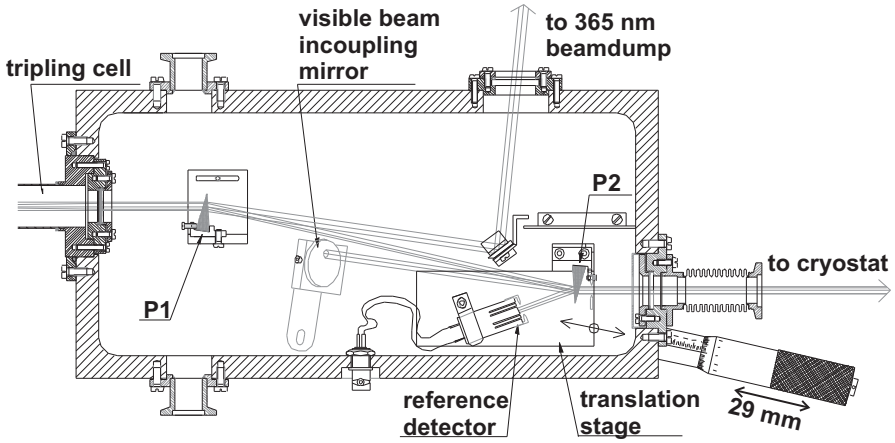

Figure 2.14: Drawing of the monochromator which separates the Lyman-α from the much intenser UV light. On the left the exit lens of the tripling cell is visible. The MgF_2 prism P1 separates the intense UV from the VUV, P2 enhances the separation and can be used to overlap a visible beam with the VUV.

a range of 30 GHz under optimal conditions. Part of this width is required for frequency stabilization, leaving a useful scan width of 18 GHz. This results in a Lyman-α scan width of 108 GHz, which is wide enough to perform spectroscopy on any single line of the Lyman-α spectrum. The center frequency can easily be changed but this requires operator intervention and 60 seconds for recalibration, during which time the measurements are paused. The signal arising from the adsorbed gas is at a different frequency than the σ_4 line of the bulk H, which is the most suitable line for determining the bulk temperature and density. The distance between these lines is 300 GHz. It is desirable to be able to change the laser frequency quickly so that adsorbate and bulk gas spectra can be probed quasi-simultaneously. This was achieved by using an extra seed laser at 729 nm. This laser, a Coherent 699 dye laser, was tuned to the broad resonance of the adsorbate, while the titanium-sapphire laser was used for spectroscopy of the 3D gas. The dye laser was not externally frequency stabilized, it may drift several tens of MHz per hour. Since the line shape of the adsorbate signal is very broad (hundreds of GHz) this drift is acceptable. Both seed lasers are equipped with an acousto-optical modulator (AOM) that functions as a light valve, at each pulse of the PDA only one AOM is activated so that only one laser frequency is used to seed the amplifier. The difference between the laser frequencies cannot be larger than $\approx$ 100 GHz as the phase matching condition in the KDP frequency doubling

crystal must be fulfilled for both frequencies.

2.4 Transmission and fluorescence detection

The part of the VUV beam that is not scattered in the cell or the buffer volume propagates through the IVC to the top of the cryostat, where a solar-blind PMT detects it. The quantum efficiency of this PMT is of order 10% at 121 nm, taking into account the absorption in the MgF_2 windows on top of the buffer volume and on top of the cryostat, the overall detection efficiency is estimated to be 2.5%. The dynode chain of the PMT is sensitive to a single photoelectron. The light flux in the cell is estimated to be 2×10^7 Lyman-α photons per pulse, taking into account loss in the MgF_2 optics. This would lead to 5×10^5 photoelectrons per pulse on the transmission PMT in the absence of a sample. In practice we detect a signal that is an order of magnitude weaker. Possible explanations for this discrepancy are contamination of the optics in the cryogenic environment, small angle scattering of light by the optics in the monochromator or a degradation of the quantum efficiency of the PMT.

The PMT has a very low sensitivity to 365 nm light, so that an offset signal due to the stray UV can be neglected. (We verified this by introducing air into the VUV monochromator, after which any remaining signal cannot be VUV and therefore must be due to stray light). It is also insensitive to light at the Balmer-α transition, which is useful when exciting two-color transitions [3]. The enormous dynamic range (over 10^6 if one adjusts the dynode voltages) of the PMT is useful when aligning the beam to the aperture in the cryostat: even when the beam is misaligned by several beam diameters a signal is detected

To sensitively detect fluorescence from the adsorbed H, a second PMT is used. The environment of the cell (small space, high field, cryogenic temperatures) is not suitable for placing a fluorescence detector close to the sample. Bolometers, such as used in ref. [1] will not work in our cell as the heat fluxes due to the recombining H greatly exceed the light pulse energy. Therefore, the light is channeled out to a room temperature PMT. To reduce losses in the optical elements, the light is converted into visible light in the cell by an organic fluorescent material, tetraphenyl butadiene (TPB) [27]. A thin layer of TPB is applied on a quartz light guide. The TPB molecules absorb scattered Lyman-α and emit radiation at $\approx$ 400 nm. This blue light is then channeled by a system of quartz light guides into an optical fiber, which guides the light to a PMT. The overall efficiency of this system is calculated to be 3×10^{-5} photoelectrons per photon scattered by a H atom [28]. This estimation

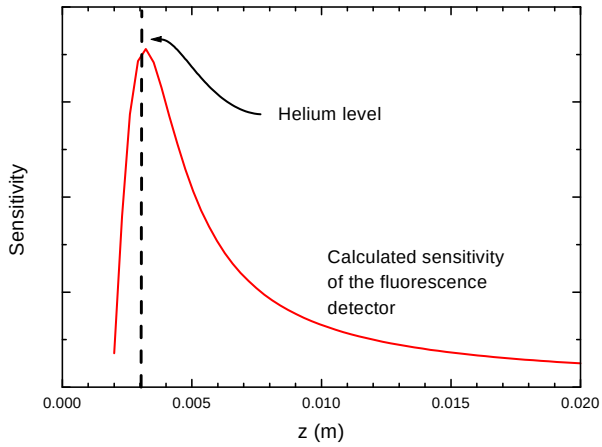

Figure 2.15: Geometrical efficiency (arbitrary units) of the fluorescence collector versus height.

includes factors such as transmission and reflection losses, conversion loss in the TPB and the quantum efficiency of the PMT. Since photoelectrons can be detected with unit efficiency, we can detect a photon flux that is as low as 10^5 scattered photons per pulse. In practice we can detect scattering of order 1% of the incident light, or better if we average the signal over many pulses. The most important advantage of using a PMT is its large dynamic range. The intensity of the fluorescence of the adsorbed gas is very low while a large amount of fluorescent light hits the detector when the light source is tuned to a bulk H line. It is convenient to have the PMT at room temperature as in the event of a breakdown it can easily be replaced. In preliminary tests we established that small PMTs (Hamamatsu 1635) could not be placed inside the cryostat as they do not work at $T < 150$ K [28], probably because the gallium arsenide dynodes fail. An important feature of the fluorescence detection system is that its geometrical collection efficiency is strongly position dependent, as shown in Fig. 2.15. The efficiency drops sharply about 3 mm from the helium surface; in this way a large cross-talk signal form off-resonant scattering of light by the atoms in the buffer volume is avoided.

References

[1] Jom Luiten, *Lyman-α spectroscopy of magnetically trapped atomic hydrogen*, Ph.D. Thesis, Universiteit van Amsterdam, 1993 (unpublished).

[2] Irwan Setija, *Optical cooling of magnetically trapped atomic hydrogen*, Ph.D. Thesis, Universiteit van Amsterdam, 1995 (unpublished).

[3] Pepijn Pinkse, *Evaporatively cooled atomic hydrogen investigated by one- and two-photon optical methods*, Ph.D. Thesis, Universiteit van Amsterdam, 1997 (unpublished).

[4] A. I. Safonov, S. A. Vasilyev, I. S. Yasnikov, I. I. Lukashevich, S. Jaakkola, and E. Tjukanov, *Atomic hydrogen experiments at the onset of two-dimensional superfluidity*, LT21, Czech. J. Phys. **46**, 539 (1996).

[5] J. J. Berkhout, *Atomic hydrogen and the surface of liquid helium*, Ph.D. Thesis, Universiteit van Amsterdam, 1994 (unpublished).

[6] The solenoid was built to order by Oxford Instruments (http://www.oxinst.com). It features a maximum field of 12 T at a temperature of 4 K and a bore diameter of 37.3 mm.

[7] Vacoflux 50 is a soft magnetic cobalt-iron alloy made by Vacuumschmelze, Hanau, Germany. Its chemical composition is equal to that of permendur 2V. See Vacuumschmelze leaflet M 039.

[8] See any electrodynamics textbook, for example: David J. Griffiths, *Introduction to Electrodynamics*, Prentice Hall, London, 1989.

[9] D. Bruce Montgomery, *Iron magnet design*, in "High Magnetic Fields", (M.I.T. press 1961).

[10] J. W. Statt and A. J. Berlinsky, *Theory of spin relaxation and recombination in spin-polarized atomic hydrogen*, Phys. Rev. Lett. **45**, 2105 (1980).

[11] R. Sprik, J. T. M. Walraven, G. H. van Yperen and Isaac F. Silvera, *Experiments with "doubly"-spin-polarized atomic hydrogen*, Phys. Rev. B **34**, 6172 (1986).

[12] Kapton is a polyimide film made by DuPont.

[13] R. Sprik, J. T. M. Walraven , G. H. van Yperen and Isaac F. Silvera, *State-dependent recombination and suppressed nuclear relaxation in atomic hydrogen*, Phys. Rev. Lett. **49**, 153 (1982).

[14] H. London, Proc. Roy. Soc. (A) **171**, 484 (1939).

[15] O.V. Lounasmaa, *Experimental Principles and Methods Below 1K*, Academic Press, Orlando, 1974.

[16] D. O. Edwards and W. F. Saam, *The Free Surface of Liquid Helium*, Progress in Low Temperature Physics, edited by D. F. Brewer (North-Holland, Amsterdam 1978), Vol. VII, p. 284.

[17] T. W. Hijmans, J. T. M. Walraven and G. V. Shlyapnikov, *Influence of the substrate on the low-temperature limit of the sticking probability of hydrogen atoms on He films*, Phys. Rev. B **45**, 2561 (1992).

[18] Rudolf Sprik, *Experiments on spin-polarized hydrogen at high density* , Ph.D. thesis, Universiteit van Amsterdam, 1986 (unpublished).

[19] James A.R. Samson *Techniques of Vacuum Ultraviolet Spectroscopy* (J. Wiley & Sons, New York, 1967).

[20] "Opti-clean polymer" available from Dantronix inc, USA, `www.opticlean.com`.

[21] Dale Electronics 1 kΩ miniature resistors, model RCWP-575, consist of bismuth ruthenate particles in a silica matrix.

[22] AVS 47 "picowatt" resistance bridge, RV Electronica OY, Finland.

[23] Q. Li, C. H. Watson, R. G. Goodrich, D. G. Haase and H. Lukefahr, *Thick film chip resistors for use as low temperature thermometers*, Cryogenics **26**, 467 (1986).

[24] P.P. Fatouros, D.O. Edwards, F.M. Gasparini, and S.Y. Shen *Isotopically pure* ^{4}*He*, Cryogenics **15**, 147 (1975).

[25] M. F. Wilson, D. O. Edwards, and J. T. Tough, *Construction of Vycor glass superleaks*, Rev. Sci. Instr. **39**, 134 (1968).

[26] G. C. Bjorklund, *Effects of focusing on third order nonlinear processes in isotropic media*, IEEE J. Quantum Electron. QE-**11**, 287 (1975).

[27] Susan Krieger, *Fluorescent materials for Lyman-α frequency downconversion*, doctoraalscriptie (Master's thesis), Universiteit van Amsterdam, 1995 (unpublished).

[28] Tycho Sonnemans, *VUV spectroscopy on atomic hydrogen adsorbed on* ^{4}*He; fluorescence detection after frequency downconversion*, doctoraalscriptie (Master's thesis), Universiteit van Amsterdam, 1994 (unpublished).

Chapter 3

Lyman-α spectroscopy of atomic hydrogen gas

Lyman-α spectroscopy is a powerful method to determine the density and temperature of cold H gas. It has been used successfully to probe trapped low field seeking H$\uparrow$ gas [1, 2], and to study optical cooling mechanisms in such a gas [5]. More recently, Lyman-α spectroscopy has enabled precise *in situ* studies of evaporative cooling [3] and of the thermodynamics of trapped H gas [4]. It has been predicted by Svistunov *et al.* [6] that optical excitation of H adsorbed on liquid ^{4}He would give rise to a signal at large positive detuning. Such a signal can be used to measure the density of adsorbed atoms, and the design of the present experiment relies on this principle.

In this chapter, I will first give a description of the theory of light propagation in a gas of H$\downarrow$ at low density (section 3.1). This description follows the analysis by Luiten [1] and Setija [5] of light propagation in a trapped sample of H$\uparrow$ and extends their approach to the case of H$\downarrow$ in high field. Further, to investigate deviations from the low-density limit, I will theoretically describe the resonant-dipole interaction that gives rise to long range optical collisions (section 3.2) and the resulting effect on the line shape (section 3.3). At the gas density present in our apparatus, this collision broadening is found to be small. An additional effect of a high density of atoms is the deviation of the refractive index from unity (section 3.4). This effect gives rise to a reflection of light from the liquid-gas interface. It is seen that for the conditions of our experiment, this reflection is negligible. The conclusion is that even at a density of ≈ 1 particle per cubic optical wavelength, the low-density theory of resonant light propagation works well, and can be used to determine density and temperature of the

sample.

By no means does our choice to use Lyman-α spectroscopy imply that there are no other methods available to probe spin-polarized H. An optical method that is very different from ours, non-resonant spectroscopy on the 1S to 2S two photon transition, has been used by the MIT atomic H group to study Bose-Einstein condensates of trapped H$\uparrow$ [9]. Non-optical methods that have successfully been used to probe H include electron spin resonance and nuclear spin resonance methods (as in e.g. [35, 36]), mechanical pressure gauges [34] and sensitive bolometric detection methods that measure the heat of recombination [32, 33, 30].

3.1 Resonant light propagation in an inhomogeneous gas

The Lyman-α spectrum of cold H$\downarrow$ is sensitive to the temperature and density of the gas, and it contains enough information for these variables to be extracted. We extract the thermodynamical variables from the spectrum by the following inversion procedure: The transmission spectra are calculated from the theory outlined in this section and parameters of the calculation are varied to obtain a least squares fit between the calculated spectra and the measured data.

The forward problem, to calculate the spectrum from the thermodynamical variables of the gas, is in itself a rich and interesting one. It has been extensively analyzed in the theses of Luiten [1] and Setija [5], in which it was applied to the spectroscopy of H$\uparrow$ in magnetic traps. For the sake of readability I will partially reproduce this analysis here before extending it to the case of high field seeking H$\downarrow$ atoms at high density and in high field.

3.1.1 The propagation equation

The propagation equations for light *in vacuo* are Maxwell's homogeneous equations. In a medium, such as an atomic gas, inhomogeneous terms due to the induced polarization in the atoms appear. In the case of optical (electric dipole) transitions, the induced magnetic dipole moment can be neglected, leading to the propagation equation for the electric field $\vec{E}(\vec{r})$:

$$\nabla^2\vec{E} - \frac{1}{c^2}\frac{\partial^2\vec{E}}{\partial t^2} = \frac{1}{\epsilon_0 c^2}\frac{\partial^2\vec{P}}{\partial t^2} - \frac{1}{\epsilon_0}\nabla(\nabla\cdot\vec{P}), \tag{3.1}$$

where the polarization $\vec{P}(\vec{r},t)$ is the induced dipole moment per unit volume in the medium. The spectrum of the bulk gas sample is calculated by integrating this differential equation over the beam path. We are interested in the propagation of a beam of narrowband radiation through the medium. *In vacuo*, such a beam is described by a plane wave with frequency ω and wavevector $\vec{k} \parallel \hat{z}$. The typical length scales on which the properties of the medium and the light beam vary are much longer than the wavelength (except at the helium-hydrogen interface, see section 3.4). Therefore, we can use the slowly varying envelope approximation (SVEA). In the SVEA, both the electric field and the induced polarization can be locally approximated by plane waves,

$$\begin{aligned} \vec{E}(\vec{r},t) &= \vec{E}_0(\vec{r},t)e^{i(kz-\omega t)}, \\ \vec{P}(\vec{r},t) &= \vec{P}_0(\vec{r},t)e^{i(kz-\omega t)}, \end{aligned} \tag{3.2}$$

with $\vec{E}_0$ and $\vec{P}_0$ the slowly varying amplitudes. Substituting Eq. 3.2 into Eq. 3.1 we find

$$\frac{\partial \vec{E}_0}{\partial z} = \frac{ik}{2\epsilon_0}\, \mathcal{P}_{xy}\vec{P}_0, \tag{3.3}$$

where $\mathcal{P}_{xy}$ is the operator that projects a vector on the xy plane. From this equation, it is easy to see that a polarization $\vec{P}_0$ that is in phase with the driving field $\vec{E}_0$ leads to a phase correction, and that a polarization that is out of phase with $\vec{E}_0$ leads to extinction of the electromagnetic wave. We are mainly interested in the case of weak radiation fields, in this case the polarization is proportional to the applied electric field. The proportionality constant is the complex electric susceptibility tensor $\overleftrightarrow{\chi}$, defined by

$$\vec{P}_0 = \epsilon_0 \overleftrightarrow{\chi}\, \vec{E}_0. \tag{3.4}$$

In the next section we will derive an expression for $\overleftrightarrow{\chi}$ in a gas of H$\downarrow$.

3.1.2 Dilute gas of two level atoms

While the light field can be treated semiclassically in Eq. 3.1, the atoms that scatter the light have to be treated quantummechanically. The H$\downarrow$ atom in a strong magnetic field, excited by a suitably polarized Lyman-α beam, is an almost ideal example of a two-level atom. We will briefly review the theory of optical excitation of a two-level atom at rest [20, 13]. The state of such an atom is described by a density matrix, ρ_{ij}. The diagonal elements ρ_{11} and ρ_{22} (with $\rho_{11}+\rho_{22}=1$) describe probabilities to find the atom in the ground and excited state, respectively. The off diagonal elements ρ_{12} and ρ_{21} (with $\rho_{12}=\rho_{21}^*$) describe the presence of coherence between these states; in

fact they are related to the probability to find an atom in a coherent superposition of the ground and excited states. The evolution of the density matrix is given by [20]

$$\dot{\rho}_{22} = -2\gamma\rho_{22} - \tfrac{1}{2}i(\Omega\rho_{12} - \Omega^*\rho_{21}), \tag{3.5}$$

$$\dot{\rho}_{12} = -(\gamma - i\Delta)\rho_{12} - \tfrac{1}{2}i\Omega^*(\rho_{22} - \rho_{11}), \tag{3.6}$$

where $\gamma \equiv \Gamma/2$ is the half width at half maximum (HWHM) and $\Delta \equiv (\omega_{21} - \omega)$. At high density, $n \gtrsim 10^{15}$ cm^{-3}, collisions will lead to extra terms in the optical Bloch equations, this phenomenon is discussed in section 3.3. The rate at which a weak applied electromagnetic field changes the density matrix elements is characterized by the Rabi frequency,

$$\Omega = \frac{-\vec{d}_{21} \cdot \vec{E}_0}{\hbar} = -(\vec{d}_{21} \cdot \hat{\varepsilon})\frac{E_0}{\hbar}, \tag{3.7}$$

where

$$\vec{d}_{21} = -e\vec{r}_{21} = -e\langle 2|\vec{r}|1\rangle \tag{3.8}$$

is the electric dipole transition matrix element (e is the positive elementary charge) and $\hat{\varepsilon}$ is the polarization unit vector of the electromagnetic field. The hydrogen atom has no permanent electric dipole moment, neither in the $1S$ ground state nor in the $2P$ excited state, but a coherent superposition of these states does have a dipole moment. It is therefore not surprising that the off-diagonal density matrix elements ρ_{12} and ρ_{21} describe the evolution of the electric dipole moment,

$$\vec{P}' = n\langle\vec{d}\rangle = 2n\rho_{21}\vec{d}_{12}e^{i(kz-\omega' t)}, \tag{3.9}$$

where n is the density of atoms and the prime means we have transformed to the inertial frame in which the atom is at rest.

For pulsed light the Rabi frequency Ω is a function of time, in general this makes the solution of the optical Bloch equations dependent on details of the pulse shape. The laser pulses in our experiment are sufficiently long (much longer than the lifetime of the excited state), that we may use a quasicontinuum picture. Furthermore, the laser pulses are so weak that there is never an appreciable fraction of the atoms in the excited state, i.e. $\rho_{22} \ll 1$ (see also section 3.5). In that case we find

$$\rho_{21} = \frac{-\frac{1}{2}\Omega}{\Delta - i\gamma}. \tag{3.10}$$

We substitute this equation into Eq. 3.9 to obtain the electric susceptibility for a gas of two-level atoms,

$$\overleftrightarrow{\chi}_0 = \frac{6\pi n}{k^3}\frac{\vec{d}_{12}\vec{d}^*_{12}}{|\vec{d}_{12}|^2}\left(\frac{\gamma}{\Delta - i\gamma}\right), \tag{3.11}$$

where we have approximated [20]

$$\begin{aligned} \gamma &= (\omega_{21}/c)^3 |\vec{d}_{12}|^2/6\pi\epsilon_0\hbar \\ &\approx k^3 |\vec{d}_{12}|^2/6\pi\epsilon_0\hbar. \end{aligned} \tag{3.12}$$

This approximation holds if the detuning $|\Delta|$ is much smaller than the excited state energy. For a multilevel system this can easily be extended to

$$\overleftrightarrow{\chi}_0 = \frac{6\pi}{k^3} \sum_{h,j} n_h \frac{\vec{d}_{hj}\vec{d}^*_{hj}}{\sum_f |\vec{d}_{fj}|^2} \left(\frac{\gamma}{\omega_{hj} - \omega - i\gamma}\right), \tag{3.13}$$

where $\vec{d}_{hj}$ is the electric dipole matrix element between a ground state h and an excited state j, ω_{hj} the corresponding transition frequency and n_h the density of atoms in the h-state. Again, a necessary condition for Eq. 3.13 is that $|\Delta| \ll \omega_{hj}$, which can only be fulfilled if the spread in transition frequencies is much smaller than the frequencies themselves. In the case of the $1S \rightarrow 2P$ transitions in H$\downarrow$, this is clearly the case. In this approximation the width of all excited states is equal, $\gamma_j = k^3 \sum_f |\vec{d}_{fj}|^2/6\pi\epsilon_0\hbar = \gamma$.

We can also determine the excited state fraction ρ_{22} by substituting ρ_{21} and ρ_{12} from Eq. 3.10 into Eq. 3.5,

$$\dot{\rho}_{22} = -2\gamma\rho_{22} + \frac{1}{2}|\Omega|^2 \frac{\gamma}{\Delta^2 + \gamma^2}. \tag{3.14}$$

The first term on the right hand side is the spontaneous decay rate, the second term is the photon absorption rate. This rate can also be written as $(I/\hbar\omega)\sigma$, where the intensity $I = \frac{1}{2}c\epsilon_0 E_0^2$ and σ is the absorption cross section,

$$\sigma = \frac{|\vec{d}_{21} \cdot \vec{\varepsilon}|^2}{|\vec{d}_{21}|^2} \, \sigma_0 \, \frac{\gamma^2}{\Delta^2 + \gamma^2}, \tag{3.15}$$

where $\sigma_0 = 3\lambda^2/2\pi$ is the maximum absorption cross-section for a polarized atom in a polarized light field. If either the light or the atoms, or both, are unpolarized, the first fraction in Eq. 3.15 must be angle-averaged and the maximum cross-section becomes $\sigma_0/3$.

The random thermal motion of the atoms gives rise to Doppler broadening of the absorption line. Due to the Doppler effect, an atom moving in the z direction experiences the electromagnetic field at a slightly different frequency, $\omega_{\rm at} = \omega - \vec{k} \cdot \vec{v}$. In addition the recoil of the atom due to the impulse from the photon causes a line shift of ≈ 13 MHz, which we ignore here. To obtain the correct lineshape in a gas of

moving atoms, one has to average the complex susceptibility tensor over the thermal distribution of atomic velocities. The transition frequencies are therefore convoluted with a Gaussian of FWHM width

$$\Delta_D = 2b\sqrt{\ln 2} \approx 1.76\,\mathrm{GHz} \times \sqrt{T[\mathrm{K}]}, \tag{3.16}$$

$$\text{where} \qquad b = k\sqrt{2k_\mathrm{B}T/m_\mathrm{H}}. \tag{3.17}$$

The convolution yields

$$\begin{aligned} \overleftrightarrow{\chi} &= \langle \overleftrightarrow{\chi}_0\,(\Delta - \vec{k}\cdot\vec{v})\rangle \\ &= i\frac{6\pi^{3/2}}{k^3}\sum_{h,j} n_h\,\frac{\vec{d}_{hj}\,\vec{d}^{\,*}_{hj}}{\sum_f |\vec{d}_{fj}|^2}\,\frac{\gamma}{b}\,w(\zeta_{hj}), \end{aligned} \tag{3.18}$$

where the angular brackets denote an average over the Maxwell velocity distribution. In this expression $w(\zeta) = e^{-\zeta^2}\mathrm{erfc}(-i\zeta)$ is the complex error function, and $\zeta_{hj} = (\omega - \omega_{hj} + i\gamma)/b$.

3.1.3 Lyman-α transitions

To calculate the susceptibility of a gas of multilevel atoms using Eq. 3.18 we need to know the transition frequencies ω_{ij} and the dipole matrix elements $\vec{d}_{ij}$ for all relevant combinations of upper and lower states. In the case of H$\downarrow$, the relevant lower states are the high field seeking a and b hyperfine states, both indicated by the fine structure label $1S(j = 1/2, m_j = -1/2)$ in figure 3.1. These states are eigenstates of the hyperfine Hamiltonian

$$H_\mathrm{HF} = a_h\vec{i}\cdot\vec{s} + (g_\mathrm{e}\mu_\mathrm{B}\vec{s} - g_n\mu_n\vec{i})\cdot\vec{B}, \tag{3.19}$$

with $\mu_n = \mu_\mathrm{B}m_e/m_p$ the nuclear magneton and $g_n = 5.56$ the gyromagnetic ratio of the proton [12]. For $B = 0$ the $1S_{1/2}$ state consists of a $(f = 1)$ triplet and a $(f = 0)$ singlet, separated by energy $a_h = 1.42\,\mathrm{GHz} \times 2\pi\hbar$ [28]. In a field the degeneracy between the $f = 1$ states is lifted, the eigenenergies for arbitrary field are shown in table 3.1.3. This table also lists the eigenstates. It is seen that the b state is a stretch state, i.e., it is $|{\downarrow}{\downarrow}\rangle$ independent of field, and it has no projection on an electron-spin up state. The lowest energy eigenstate a resembles the nuclear spin up state $|{\downarrow}{\uparrow}\rangle$ in a high field, but it has a projection on the electron spin up state $\sin\theta_h|{\uparrow}{\downarrow}\rangle$. Here the hyperfine projection angle θ_h is given by

$$\tan 2\theta_h = a_h/(\mu^+ B);\ \ \mu^\pm = g_e\mu_\mathrm{B} \pm g_n\mu_n. \tag{3.20}$$

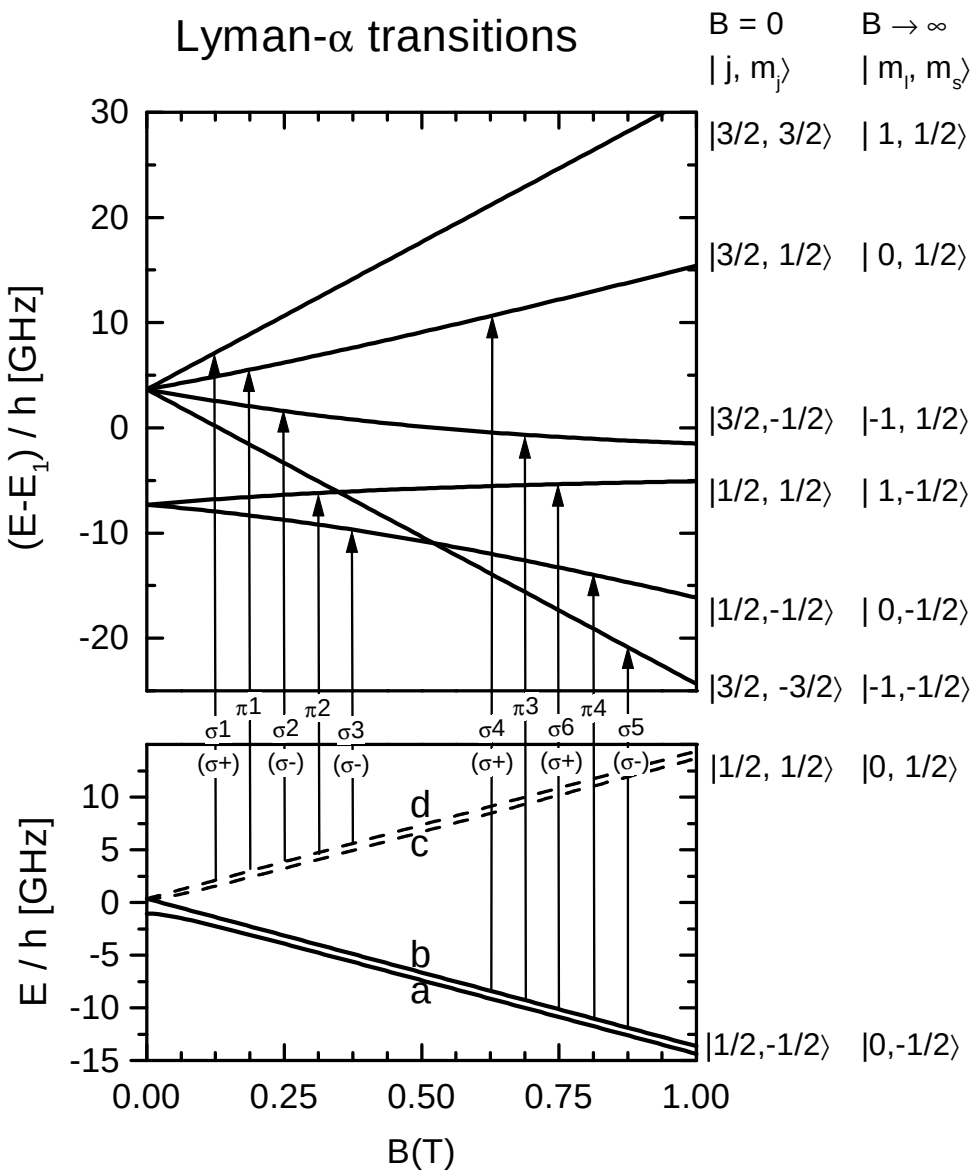

Figure 3.1: Allowed transitions between the $1S$ and $2P$ states in H. The labels used to identify the transitions are shown, as well as the polarization needed to excite the σ transitions. The excited state energies are shown relative to $E_1/h = 2\,466\,068$ GHz [10, 11, 14]

The probability to measure the electron of an a state atom in the spin-up state is proportional to $\sin^2\theta_h$, which is $\approx (0.025\mathrm{T}/B)^2$ in high field.

The relevant excited states are the $2P$ states, which can be labeled either by their low-field quantum numbers j, m_j or by the high-field labels m_l, m_s, as shown in figure 3.1. The hyperfine splitting in the $2P$ states is well below the radiative linewidth, as the wavefunctions of the nucleus and the electron hardly overlap [1]. However, the nuclear spin does give rise to a nuclear Zeeman effect, $\mu_n g_n B$, which is 125 MHz in a field of 6 T, of the order of the radiative linewidth of the $2P$ level. The fine structure energies of the $2P$ states and the admixture coefficients are given in table 3.1.3. The projection coefficients in this table are expressed in the fine structure projection angles $\theta_\pm$, with

$$\sin\theta_\pm \equiv \sqrt{\tfrac{1+\delta_\pm}{2}} \approx 1 - \frac{0.068\,\mathrm{T}^2}{B^2}\ (B\to\infty); \tag{3.21}$$

$$\cos\theta_\pm \approx \frac{0.136\,\mathrm{T}^2}{B^2}\ (B\to\infty), \tag{3.22}$$

with

$$\delta_\pm = \frac{x \pm 1/3}{\sqrt{1 \pm 2x/3 + x^2}},\ \ x = B/B_{\mathrm{LS}} = B/0.781900\,\mathrm{T}. \tag{3.23}$$

In a field of 6 T, the probability to measure a $2P_{1/2,-1/2}$ atom with its electron spin up is $\cos^2\theta_- \approx 4\times10^{-3}$.

For an electric dipole transition, the electric field of the light couples directly to the orbital motion of the electron. In absence of spin-orbit coupling the selection rule for optical transitions is $|l'-l|=1$, $m_l'-m_l\in\{-1,0,1\}$, and all transition dipole elements $\vec{d}_{ij}$ that do not obey this rule are zero. In case an excited eigenstate is a superposition of various m_l states, the transition dipole moment of a transition from the $|s,m_s\rangle$ ground state to the $|j',m_j'\rangle$ excited state couples to those $|l,m_l\rangle$ components of the excited state wavefunction for which the dipole matrix element is nonzero. The resulting dipole moment is

$$\vec{d}_{(l=0,m_s),(j',m_j')} \equiv -e\langle j',m_j'|\vec{r}|l=0,m_s\rangle \tag{3.24}$$

$$= \sum_{l',m_l',m_s'} \langle l',m_l',s,m_s'|j',m_j'\rangle \vec{d}_{(l=0,m_s),(l',m_l')}. \tag{3.25}$$

This leads to the transition probabilities indicated in table 3.2 for the transitions from the b state. From the a state, there are five transitions that resemble the transitions from the b state. These transitions couple to the $|{\downarrow}{\updownarrow}\rangle$ component of the a state. An additional five transitions couple to the $|{\uparrow}{\updownarrow}\rangle$ hyperfine component, these are therefore referred to as hyperfine-enabled transitions. In high field the transition probabilities

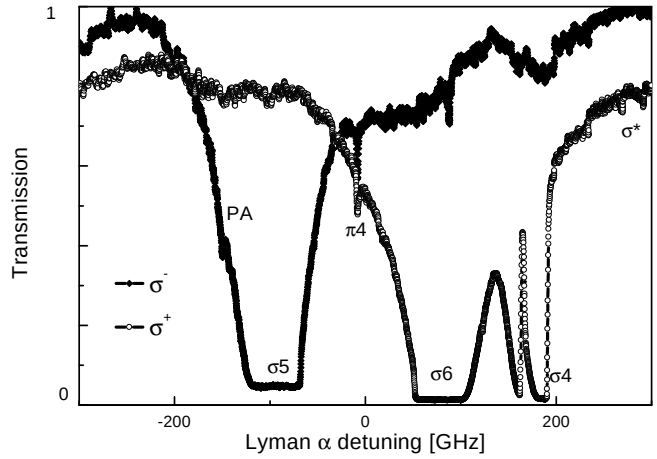

Figure 3.2: Measured transmission spectrum of the hydrogen bulk gas, showing the allowed transitions σ_5 and σ_6, the geometrically forbidden π_4 transition, the fine-structure enabled transition σ_4 and the hyperfine-enabled transition σ_*, which is just recognizable in the noise. The σ_4 and σ_* transitions are Zeeman split because the fields in buffer and compression cell are different. The background noise is due to drifts of the laser system during manual scanning. This spectrum took 8 hours measuring time.

of the hyperfine-enabled transitions are strongly suppressed, as can be seen in table 3.2. This can also be seen in the spectrum in figure 3.2.

3.1.4 Simplified propagation equation

Using the transition frequencies and matrix elements from the preceding section we can now numerically solve the propagation equation (3.3). The specific geometry of our experiment allows us to simplify the equation considerably. The greatest simplification comes from the fact that the magnetic field on the axis of our apparatus is parallel to the direction of propagation of the light beam. Therefore, the absorption probability on any of the π transitions vanishes. In practice, very weak π lines can be seen due to a slight misalignment. The fact that the propagation of propagation coincides with the field lines has another important consequence, namely, that the complex susceptibility tensor $\overleftrightarrow{\chi}$, as calculated from Eq. 3.18, can be diagonalized in the laboratory frame. The susceptibility becomes diagonal in the circular basis $(\hat{\varepsilon}_+, \hat{\varepsilon}_-, \hat{\varepsilon}_z)$. Here $\hat{\varepsilon}_-$ stands for the right hand circular polarized (RHP) component, $\hat{\varepsilon}_+$ stands for the left hand circular polarized (LHP) component and $\hat{\varepsilon}_z$ is the z polarized component. The electric field is written $\vec{E}_0 = \vec{E}_0 = E_{0+}\hat{\varepsilon}_+ + E_{0-}\hat{\varepsilon}_-$ in this basis.

	m_j	energy	state
$2^2P_{3/2}$	$\frac{3}{2}$	$E_{2P} + \Delta/3 + (1+g_e/2)\mu_B B$	$\|1\uparrow\rangle$
	$\frac{1}{2}$	$E_{2P} - \Delta/6 + \mu_B B/2 + (\Delta/2)\sqrt{1+2x/3+x^2}$	$\sin\theta_+\|0\uparrow\rangle + \cos\theta_+\|1\downarrow\rangle$
	$-\frac{1}{2}$	$E_{2P} - \Delta/6 - \mu_B B/2 + (\Delta/2)\sqrt{1-2x/3+x^2}$	$\sin\theta_-\|-1\uparrow\rangle + \cos\theta_-\|0\downarrow\rangle$
	$-\frac{3}{2}$	$E_{2P} + \Delta/3 - (1+g_e/2)\mu_B B$	$\|-1\downarrow\rangle$
$2^2P_{1/2}$	$\frac{1}{2}$	$E_{2P} - \Delta/6 + \mu_B B/2 - (\Delta/2)\sqrt{1+2x/3+x^2}$	$-\cos\theta_+\|0\uparrow\rangle + \sin\theta_+\|1\downarrow\rangle$
	$-\frac{1}{2}$	$E_{2P} - \Delta/6 - \mu_B B/2 - (\Delta/2)\sqrt{1-2x/3+x^2}$	$-\cos\theta_-\|-1\uparrow\rangle + \sin\theta_-\|0\downarrow\rangle$
$1^2S_{1/2}$	d	$a_h/4 + \mu^- B/2$	$\|0\uparrow\uparrow\rangle$
	c	$-a_h/4 + (a_h/2)[1+(\mu^+ B/a_h)^2]^{1/2}$	$\cos\theta_h\|0\uparrow\downarrow\rangle + \sin\theta_h\|0\downarrow\uparrow\rangle$
	b	$a_h/4 - \mu^- B/2$	$\|0\downarrow\downarrow\rangle$
	a	$-a_h/4 - (a_h/2)[1+(\mu^+ B/a_h)^2]^{1/2}$	$\sin\theta_h\|0\uparrow\downarrow\rangle - \cos\theta_h\|0\downarrow\uparrow\rangle$

Table 3.1: Energy levels and eigenstates of the ground state hyperfine structure and the first excited state fine structure of hydrogen in a magnetic field. The magnetic moments $\mu^{\pm} = g_e\mu_{\rm B} \pm g_n\mu_n$ may be approximated by $\mu^{\pm} \approx 2\mu_{\rm B}$ with only a $< 0.1\,\%$ error. The hyperfine mixing angle θ_h is defined in Eq. 3.20.

Since the propagation direction is $\hat{z}$, the component along $\hat{\varepsilon}_z$ represents a longitudinal field and therefore remains zero. The complex susceptibility tensor then takes the form

$$\left[\overleftrightarrow{\chi}\right]' = \begin{pmatrix} \chi_+ & 0 & 0 \\ 0 & \chi_- & 0 \\ 0 & 0 & \chi_z \end{pmatrix}. \tag{3.26}$$

where, in the case of a sample consisting of b atoms,

$$\begin{aligned} \chi_- &= i(6\pi^{3/2}/k^3)\, n_b\, (\gamma/b)\, w(\zeta_{\sigma 5}), \\ \chi_+ &= i(6\pi^{3/2}/k^3)\, n_b\, (\gamma/b)\, [\sin^2\theta_+\, w(\zeta_{\sigma 6}) + \cos^2\theta_+\, w(\zeta_{\sigma 4})], \\ \chi_z &= 0. \end{aligned} \tag{3.27}$$

Label	Poln.	Zeeman	$m_{s,i}\rightarrow m_{l,s,i}$	Low field notation	Γ_{ij}/Γ	$\Gamma_{ij}(6\,\mathrm{T})/\Gamma$
σ_5	$\sigma-$	-1	$\downarrow\downarrow \rightarrow -1\downarrow\downarrow$	$b \rightarrow 2P_{3/2,-3/2}$	1	1
π_4	π	0	$\downarrow\downarrow \rightarrow 0\downarrow\downarrow$	$b \rightarrow 2P_{1/2,-1/2}$	$\sin^2\theta_-$	0.995 93
σ_6	$\sigma+$	$+1$	$\downarrow\downarrow \rightarrow 1\downarrow\downarrow$	$b \rightarrow 2P_{1/2,1/2}$	$\sin^2\theta_+$	0.996 57
σ_4	$\sigma+$	$+2$	$\downarrow\downarrow \rightarrow 0\uparrow\downarrow$	$b \rightarrow 2P_{3/2,1/2}$	$\cos^2\theta_+$	3.4×10^{-3}
π_3	π	$+1$	$\downarrow\downarrow \rightarrow -1\uparrow\downarrow$	$b \rightarrow 2P_{3/2,-1/2}$	$\cos^2\theta_-$	4.1×10^{-3}
$\sigma_5 a$	$\sigma-$	-1	$\downarrow\updownarrow \rightarrow -1\downarrow\updownarrow$	$a \rightarrow 2P_{3/2,-3/2}$	$\cos^2\theta_h$	0.999 98
$\pi_4 a$	π	0	$\downarrow\updownarrow \rightarrow 0\downarrow\updownarrow$	$a \rightarrow 2P_{1/2,-1/2}$	$\cos^2\theta_h \sin^2\theta_-$	0.995 91
$\sigma_6 a$	$\sigma+$	$+1$	$\downarrow\updownarrow \rightarrow 1\downarrow\updownarrow$	$a \rightarrow 2P_{1/2,1/2}$	$\cos^2\theta_h \sin^2\theta_+$	0.996 55
$\sigma_4 a$	$\sigma+$	$+2$	$\downarrow\updownarrow \rightarrow 0\uparrow\updownarrow$	$a \rightarrow 2P_{3/2,1/2}$	$\cos^2\theta_h \cos^2\theta_+$	3.4×10^{-3}
$\pi_3 a$	π	$+1$	$\downarrow\updownarrow \rightarrow -1\uparrow\updownarrow$	$a \rightarrow 2P_{3/2,-1/2}$	$\cos^2\theta_h \cos^2\theta_-$	4.1×10^{-3}
	π	$+1$	$\downarrow\updownarrow \rightarrow 1\downarrow\downarrow$	$a \rightarrow 2P_{1/2,1/2}$	$\sin^2\theta_h \cos^2\theta_+$	6.1×10^{-8}
	$\sigma-$	0	$\downarrow\updownarrow \rightarrow 0\downarrow\downarrow$	$a \rightarrow 2P_{1/2,-1/2}$	$\sin^2\theta_h \cos^2\theta_-$	7.2×10^{-8}
σ_*	$\sigma+$	$+3$	$\downarrow\updownarrow \rightarrow 1\uparrow\downarrow$	$a \rightarrow 2P_{3/2,3/2}$	$\sin^2\theta_h$	1.8×10^{-5}
π_*	π	$+2$	$\downarrow\updownarrow \rightarrow 0\uparrow\downarrow$	$a \rightarrow 2P_{3/2,1/2}$	$\sin^2\theta_h \sin^2\theta_+$	1.8×10^{-5}
	$\sigma-$	$+1$	$\downarrow\updownarrow \rightarrow -1\uparrow\downarrow$	$a \rightarrow 2P_{3/2,-1/2}$	$\sin^2\theta_h \sin^2\theta_-$	1.8×10^{-5}

Table 3.2: Lyman-α transitions from the high field seeking a and b states of H. The approximate Zeeman shift of the transitions in high field is indicated in units of μ_B. The high field quantum numbers m_s, m_i of the lower state and m_l, m_s, m_i of the upper state are given in addition to the more usual low-field quantum numbers.

The propagation equation (3.3) now reduces to a system of two *uncoupled* differential equations,

$$\frac{\partial E_{0+}}{\partial z} = \frac{ik}{8}\chi_+ E_{0+}\,; \quad \frac{\partial E_{0-}}{\partial z} = \frac{ik}{8}\chi_- E_{0-}, \tag{3.28}$$

which can be integrated to

$$E_{0\pm}(z) = E_{0\pm}(0)\exp\left(-\frac{1}{2}D_\pm(z) + i\phi_\pm(z)\right), \tag{3.29}$$

$$-\frac{1}{2}D_\pm(z) + i\phi_\pm(z) = \int_0^z dz'\frac{ik}{8}\chi_\pm(z'). \tag{3.30}$$

The real part $-\frac{1}{2}D$ of the integral represents the optical density of the gas, the imaginary part ϕ expresses the phase shift the light acquires while passing through the gas. In principle, the optical density may equally well be calculated from the absorption cross-section,

$$D_\pm(z) = \int_0^z dz' n(z')\sigma_\pm(z',\omega), \tag{3.31}$$

where $\sigma_\pm$ is the effective cross-section of the atoms, taking into account Doppler broadening. The approach we used has the advantage that it is more easily generalized to hold for arbitrary directions of the magnetic field. This has been used to obtain the equations that describe light propagation through H$\uparrow$ in a magnetic trap [1, 2, 5].

3.2 Resonant dipole interaction

As one increases the density of an atomic gas, the interactions between the atoms will manifest themselves in the spectrum. The main contribution will be due to two-particle effects, since in a gas the probability to find three or more particles within the range of interaction is always smaller than the probability to find two particles. The interactions between excited and ground state atoms of the same species have a particularly long range. At interatomic distances of $\gtrsim 10$ atomic units (a_0) the interaction potential has the $1/r^3$ behavior typical of dipole-dipole interactions. This resonant dipole coupling was first pointed out by Eisenschitz and London in ref. [17]. Since this interaction plays an important role in the estimation of the effects of pressure broadening and in the observation of photoassociation I will sketch the mechanism that gives rise to this interaction. For a more thorough discussion, the papers by King and van Vleck [18] and by Mulliken [19] are recommended.

When two atoms are close together the atom pair must be described as a quasi-molecule, even if the electron clouds of the atoms do not overlap. We will consider two H atoms at rest, at a distance that is smaller than the Lyman-α wavelength λ_α, but much larger than the extent of the electronic wavefunctions (of order of the Bohr radius a_0). Since the atoms interact, the eigenfunctions of the Hamiltonian of this system are not separable into atomic wavefunctions, instead they are the appropriately symmetrized wavefunctions

$$\Psi(\vec{r}_1,\vec{r}_2) = \frac{1}{2}\sqrt{2}\left[\Psi_S(\vec{r}_1)\Psi_P(\vec{r}_2) + \eta\Psi_P(\vec{r}_1)\Psi_S(\vec{r}_2)\right]. \tag{3.32}$$

Here, Ψ_S is a $1S$ wavefunction, Ψ_P a $2P$ state and $\eta = \pm 1$ the appropriate symmetry factor, for a spin triplet $\eta = -1$, for a singlet state $\eta = 1$. These states can be rewritten as

$$\begin{aligned}\Psi(\vec{r}_1,\vec{r}_2) &= \frac{1}{2}\sqrt{2}\left[\Psi_S(\vec{r}_1) + \eta\Psi_P(\vec{r}_1)\right]\times\left[\Psi_P(\vec{r}_2) + \Psi_S(\vec{r}_2)\right] \\ &\quad -\frac{1}{2}\sqrt{2}\Psi_S(\vec{r}_1)\Psi_S(\vec{r}_2) - \frac{\eta}{2}\sqrt{2}\Psi_P(\vec{r}_1)\Psi_P(\vec{r}_2).\end{aligned} \tag{3.33}$$

The latter two terms in this equation are product states of atomic S and P wavefunctions. These terms do not have an electric dipole moment [16]. Therefore, the

interactions between these states will be of the normal Van der Waals type, $\sim 1/r^6$. The superposition $S \pm P$ does have a dipole moment, in fact, as can be seen from equation (3.8),

$$e\left\langle \frac{S+\eta P}{\sqrt{2}}\middle|\,\vec{r}\,\middle|\frac{S+\eta P}{\sqrt{2}}\right\rangle = e\eta\,\langle P|\,\vec{r}\,|S\rangle = \eta\vec{d}_{SP}\,. \tag{3.34}$$

Therefore, this term in the molecular wavefunction resembles the product of two atomic wavefunctions which each have an oscillating electric dipole moment, with the size of the transition dipole moment. Although the expectation value of the product of these dipole operators is nonzero, the expectation value of the dipole operator for the complete molecular wavefunction is still zero, i.e., the molecule does not have a permanent electric dipole moment. Since the atoms are separated by much less than an optical wavelength, we may neglect the retardation of the electromagnetic field. We then use the electrostatic dipole interaction formula for point dipoles $\vec{d}_{\mathrm{a,b}}$ separated by $\vec{r}$,

$$U_{\mathrm{dip,dip}} = \frac{1}{4\pi\epsilon_0 r^3}\left[\vec{d}_{\mathrm{a}}\cdot\vec{d}_{\mathrm{b}} - 3(\vec{d}_{\mathrm{a}}\cdot\hat{r})(\vec{d}_{\mathrm{b}}\cdot\hat{r})\right]. \tag{3.35}$$

The direction of the dipoles $\vec{d}_{SP}$ in the quasimolecule is opposite (for $\eta = 1$)[19], and the dot product $\vec{d}_{SP}\cdot\hat{r}$ is zero for a Π molecular state and maximal for a Σ state [31]. Therefore, the interaction potential between two atoms in a state with orbital angular momentum Λ about the internuclear axis becomes

$$U_\Lambda = \frac{1}{4\pi\epsilon_0 r^3}\eta|\vec{d}_{SP}|^2\left[2-3\Lambda^2\right] \equiv \frac{C_3}{r^3}\eta\left[2-3\Lambda^2\right]. \tag{3.36}$$

In atomic units, C_3 can be evaluated for H to give $C_3 = \eta \times 2^{15}/3^{10} \approx \eta \times 0.555$ a.u. [21]. Alternatively, we can use the fact that the value of $\vec{d}_{SP}$ is related to the radiative HWHM linewidth γ through Eq. 3.12, so that we can write

$$C_3 = \eta\frac{3\hbar\gamma}{2(2\pi)^3}\lambda_\alpha^3. \tag{3.37}$$

This formulation makes clear that the range of interaction, defined as the internuclear distance where the interaction becomes of the order of the radiative level width, is $\approx \lambda_\alpha/2\pi$, or $\approx 360a_0$. Approximately at this same distance, the electrostatic approximation breaks down, since the electric field will pick up a non-negligible phase shift while traveling from one atom to the other.

3.3 Pressure broadening

The optical Bloch equations as reproduced above (3.5,3.6) are valid in the limit of low density only. In case the density of atoms is high, interatomic collisions will modify

the spectrum. The theory of pressure broadening in a gas [24] is rather complex and the simplified expressions here will only suffice to estimate the effect. There are two approaches for including the effects of collisions in the optical Bloch equations: impact broadening and quasistatic pressure broadening. The first approach, valid at moderate density and relatively high temperature, is to assume that the atoms undergo instantaneous phase-changing collisions. It is only valid if the duration of the collisions is shorter than the radiative lifetime of the upper state. The quasistatic theory of pressure broadening, on the other hand, applies if the atomic velocities are so low and the densities are so high that the excited atoms is within range of the potential of the other atom for longer than its radiative lifetime. This type of broadening also applies in the very far wings of the line, $|\Delta| \gg \gamma$, since there the relevant time scale for the excitation is $1/|\Delta|$ instead of $1/\gamma$. A key difference between impact broadening and quasistatic broadening lies in the fact that impact broadening is a homogeneous broadening mechanism, and therefore reduces power broadening, while static pressure broadening is an inhomogeneous mechanism. The atoms move at an average relative speed $\bar{v}\sqrt{2}$. In our case, at 150 mK, they cover a distance of $\bar{v}\sqrt{2}/\Gamma \approx 100$ nm before decaying radiatively. The range of the potential is $\approx \lambda_\alpha/2\pi$, which is a factor 5 smaller, so the lineshape near resonance is reasonably described by impact broadening.

In the impact broadening picture, a collision destroys coherence between the different states of the atoms. The impact resets the off-diagonal elements of the density matrix ρ_{12}, ρ_{21} to zero, but the populations (the diagonal elements of ρ) remain unchanged [20]. This approach is valid if the duration of a collision is much shorter than the time τ_0 of free-flight in between collisions. In this simple picture, a pair of atoms collides if they approach each other to a distance shorter than the Weisskopf radius r_W, which is the radius where a collision will result in a phase shift of 1 [25, 26]. We find, using the resonant dipole interaction potential (3.36),

$$\sigma_{1S-2P} = \pi r_W^2 = \frac{3\gamma\lambda_\alpha^3}{4\pi^2\bar{v}_{\rm rel}} \approx 4\times 10^4 a_0^2, \tag{3.38}$$

where $\bar{v}_{\rm rel}$ is the average relative atomic speed, $\bar{v}_{\rm rel} = \sqrt{2}\bar{v}$. This leads to a collision frequency of

$$\begin{aligned} \gamma_{\rm coll} &= 1/\tau_0 = n\sigma_{1S-2P}\bar{v}_{\rm rel} = n\frac{3\gamma\lambda_\alpha^3}{4\pi^2} \\ &\approx \left(\frac{n}{1.5\times 10^{16}{\rm cm}^{-3}}\right)\gamma \end{aligned} \tag{3.39}$$

The collision rate will be of the order of the radiative lifetime at $n \approx 1.5\times 10^{16}$ cm^{-3}. At the densities encountered in our experiment, impact broadening does not

play an important role. At the highest density the effect on the linewidth in the buffer volume is only a few percent, in the cell the linewidth is strongly dominated by Zeeman broadening.

At large detuning, $|\Delta| \gg \gamma$, the impact broadening picture is not valid. Instead, one must use the quasistatic theory of pressure broadening, as developed by Jabloński [23]. I will discuss a very basic formulation of the quasistatic broadening theory here.

If the optical frequency is detuned far enough from resonance for $1/|\Delta|$ to become short compared to the duration of a collision, one can treat the atoms as stationary. At intermediate density, the light absorption at large positive detuning $\Delta \gg \gamma$ is then dominated by atom pairs which are at the internuclear distance r where $V(r) = \hbar\Delta$. The lineshape at large detuning is then given by

$$F(\Delta) = \frac{\pi\gamma}{\Delta^2} + 4\pi n \int r^2 dr \chi(r) \sum_{\Lambda} P(\Lambda)\hbar\delta(\hbar\Delta - \frac{C_3}{r^3}[2 - 3\Lambda^2]);\ (\Delta \gg \gamma). \quad (3.40)$$

Here, the first term is the Lorenzian wing of the single atom line, the second term is the contribution of the light absorption by atom pairs. The pair correlation function $\chi(r)$ depends on the ground state interactions and the quantum statistics. It can be taken equal to unity for a weakly interacting nondegenerate gas. There are three quasimolecular states which contribute, depending on the angle between the internuclear axis and the polarization vector of the light. In the isotropic case, the probability $P(\Lambda)$ for each Λ state to be excited is equal to 1/3. The attractive states should not be included, as for negative detuning only discrete molecular levels (photoassociation lines) can be excited. For a spin triplet quasimolecule, the repulsive states are the two Π states, with the same potential, corresponding to $\Lambda = \pm 1$. We evaluate the integral, and obtain

$$\begin{aligned} F(\Delta) &= \frac{\gamma}{\pi\Delta^2} + \frac{8}{9}\pi n \frac{C_3}{\hbar\Delta^2}, & (3.41)\\ &= \frac{1}{\pi\Delta^2}\left(\gamma + \frac{8nC_3}{9\hbar}\right), & (3.42)\\ &= \frac{\gamma}{\pi\Delta^2}\left(1 + n\frac{\lambda^3}{6\pi}\right). & (3.43) \end{aligned}$$

The result for the quasistatic pressure broadening term is approximately 30% smaller than the extrapolation of the impact broadening expression (3.39) to large detuning. There is an extra factor which comes into play at large detunings: in obtaining relation (3.41) classical correlations between the particles have been assumed. In the case the colliding particles are closer than the thermal de Broglie wavelength, quantum effects on the two-particle correlator $\chi(r)$ come into play [27]. This is the case for

$\Delta/\gamma \gtrsim \lambda^3/\Lambda^3$, where λ is the optical wavelength and Λ is the thermal de Broglie wavelength of the atoms (A.1). For an ideal Bose gas, the quantum correlator at distances much smaller than Λ is approximately 2, while the classical correlator is unity. In the present experiment the de Broglie wavelength is rather small, of order 5nm, so that quantum effects will only be visible at a detuning of $\Delta \gtrsim 1000$ GHz. At such detunings, the signal strength is insufficient to observe these effects.

In conclusion, at the present densities pressure broadening is not (yet) important. However, we are very close to the region where it determines the line shape at large detuning. Mechanisms such as resonant transfer of excitation [22] influence the lineshape only at even higher densities.

3.4 Refraction effects

When the index of refraction of the gas differs appreciably from unity there will be effects of this refraction on the propagation of the light inside the sample. In addition, the refractive index of the gas determines the reflection and transmission of light at the sharp boundary between the H gas and the liquid helium.

The dielectric constant $\epsilon(\omega)$ of a dilute gas of polarizable atoms can be found from

$$\epsilon_{\pm}(\omega)/\epsilon_0 = 1 + n\,\mathrm{Re}\,\chi_{\pm}(\omega), \tag{3.44}$$

where n is the number density of atoms and $\chi_{\pm}$ is the appropriate diagonal element of the susceptibility tensor (3.27). In a magnetic field, the dielectric constant for LHP light, ϵ_+, may be different from that for RHP light, ϵ_-, this is known as the Faraday effect. If the refractive index is not close to unity, one has to use the Lorentz-Lorenz relation to include the effects of local field factors on the dielectric constant (see for example Ref. [7]). We will assume the low density approximation holds. We find the refractive index of the hydrogen gas, η_H from Maxwell's relation, $\eta_{\mathrm{H}}(\omega) = [\epsilon(\omega)/\epsilon_0]^{1/2}$. At the helium surface the light passes from the helium ($\eta_{\mathrm{He}} = 1.03$ [15]) into the hydrogen gas, at normal incidence. If there is a mismatch between the refractive indices of the liquid and the gas, part of the light will be reflected, as expressed by the Fresnel formula [8],

$$R_{\perp} = \left(\frac{\eta_{\mathrm{H}} - \eta_{\mathrm{He}}}{\eta_{\mathrm{H}} + \eta_{\mathrm{He}}}\right)^2. \tag{3.45}$$

Note that this reflected intensity can in principle be calculated from the full propagation equation (3.1). The reflection arises from the fact that the polarizability changes

abruptly at the liquid-gas interface, a violation of the slowly varying envelope approximation (SVEA). In the SVEA, reflection does not occur. Therefore, the reflection probability does not follow from the attenuation equation (3.3), which is based on the SVEA.

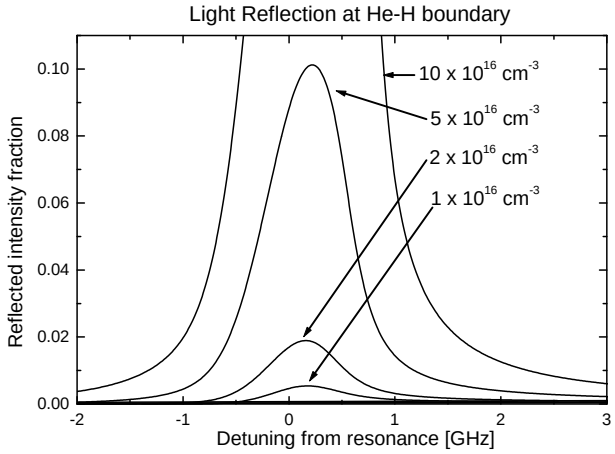

Figure 3.3: Intensity reflection coefficient of the interface between liquid helium and very dense H$\downarrow$. Curves drawn for a number of H$\downarrow$ densities, at $T = 130$ mK.

Since the reflected beam will not reach the fluorescence detector, a decrease in the measured fluorescence will occur. Figure 3.3 shows the reflected intensity in the present situation at the maximum obtained density of $\approx 2 \times 10^{16}$ atoms per cm^3. The reflection is slightly too small to be observed under present conditions. When the bulk gas density is increased, reflective effects will become more important, leading to a reflected intensity of almost 10 percent at 5×10^{16} atoms/cm^3 (see figure 3.3).

3.5 Power broadening

Power broadening is the first onset of nonlinear optical phenomena in a gas. It occurs when the exciting light beam is intense enough that a sizable fraction of the atoms is in the excited state. In this case, the excited state population ρ_{22} cannot be neglected in equation (3.6), and equation (3.10) does not hold. For a small amount of power broadening, the steady-state value of ρ_{22} can be estimated from equation (3.14) to be

$$\rho_{22} \approx \frac{1}{4} \frac{|\Omega|^2}{\Delta^2 + \gamma^2}. \tag{3.46}$$

If we substitute this approximation back into the optical Bloch equation (3.6), this can be seen to lead to a reduction of the excitation rate at resonance by a factor $(1 - 2\rho_{22})=1 - |\Omega|^2/2\gamma^2$. Therefore, power broadening becomes important when $|\Omega| \approx \gamma$, which for the allowed Lyman-α transitions is at an intensity of $I_{\rm sat} = 3.6{\rm W/cm}^2$. The intensity of the Lyman-α beam in our compression cell is estimated to be approximately 5×10^7 photons per 10 ns pulse on a ≈ 0.25 mm^2 area, which yields approximately 3 W/cm^2. This means saturation broadening is expected to be of the same order as the radiative linewidth for the allowed lines. The allowed σ_5 and σ_6 lines are already strongly broadened by the optical thickness of the gas, and the extra power broadening, which is only relevant near the line center, will not be observable.

The case is different for the L-S-enabled σ_4 transition, whose Zeeman-broadened lineshape we use to determine the temperature of the bulk gas. This line is optically thin, and power broadening would certainly influence the inferred gas temperature. Fortunately, since the dipole moment for excitation of this transition is much smaller, the Rabi frequency is much smaller and the influence of power broadening is reduced strongly.

The presence of other broadening mechanisms may change the influence of power broadening. For instance, collision broadening in a gas increases the linewidth and reduces power broadening. Doppler broadening, an inhomogeneous broadening mechanism, does not decrease power broadening. In the case of Doppler broadening, the thermal sample can be thought to consist of classes of atoms, each class moving at a certain velocity. For each class, there is power broadening, and the net effect will be a reduction of the apparent light scattering cross-section.

A special case is the adsorbate signal, which is an allowed line that is broadened by interactions with the liquid helium. This interaction broadening can be viewed as homogeneous collision broadening [20] due to collisions with the helium atoms in the surface layer, and therefore we expect power broadening to be reduced. An upper limit to the excited state fraction is the number of photons scattered per atom in the beam region, per radiative lifetime, $\rho_{22} = \Phi_{\rm phot} P_{\rm scatt}/(\Gamma A_{\rm beam} n_2)$. We insert $A_{\rm beam} = 2 \times 10^{-8}$ m^2, $\Phi_{\rm phot} = 10^{15}$/s for the photon flux during a pulse, $n_2 = 10^{12}$ cm^{-3}, and $P_{\rm scatt} \approx 0.02$ for a typical surface fluorescence, and find $\rho_{22} \approx 2 \times 10^{-3}$. Therefore, we do not expect the adsorbate signal to suffer from power broadening.

3.6 Spectroscopic determination of thermodynamic quantities

As demonstrated in the preceding sections, deviations from the low-density low intensity picture presented in section 3.1 are very small. Therefore, we can use equation (3.29) to calculate the transmission spectrum of the bulk gas sample given the temperature and density distribution. Since the atoms undergo thermalizing collisions with each other and with the helium coated walls of the reservoirs, the density distribution will be thermal,

$$n(z) = n_0 e^{\mu_B (B(z) - B_{\max})/k_B T}. \tag{3.47}$$

Here $B_{\max}$ is the maximum field in the reservoir under consideration and n_0 is the reference density (the density at $B_{\max}$). The buffer volume and compression cell are separated by a potential barrier, therefore the temperature T_3 and reference density n_3 of the gas in the compression cell can be different from the temperature and density T_B, n_B in the buffer (see chapter 5). Therefore, there are four thermodynamic quantities of interest in a one-component gas. Since the gas will always contain some atoms in the a hyperfine state, the hyperfine composition $(n^{(a)}/n)$ of the gas in both volumes is another set of parameters on which the spectrum depends. Finally, the spectrum depends quite strongly on the position of the helium surface in the compression cell. The exact position of this surface depends on the amount of helium liquid present. If more helium is present, the high-field area near the tip of the magnetic compressor becomes inaccessible to the H$\downarrow$ atoms, and the maximum Zeeman shift will be reduced.

3.6.1 Determination of the temperature of bulk H in the compression cell

The bulk gas in the compression cell is compressed down by the magnetic field gradient of the CoFe pole pieces. This magnetic field acts like artificial gravity on the magnetic hydrogen atoms, therefore the density profile in the cell is atmospheric. The atmosphere height is directly proportional to the temperature T_3 of the bulk gas. When we probe the gas on a Zeeman shifted optical transition, the resonance frequency depends on the local magnetic field. Through this inhomogeneous Zeeman broadening, the spectrum roughly reflects the atmospheric profile. The $1/e$ width of the inhomogeneously broadened line, as shown in figure 3.4, is

$$(\delta\omega)_Z/2\pi = 2k_B T_3/2\pi\hbar \approx 28\,\mathrm{GHz} \times T_3[\mathrm{K}]. \tag{3.48}$$

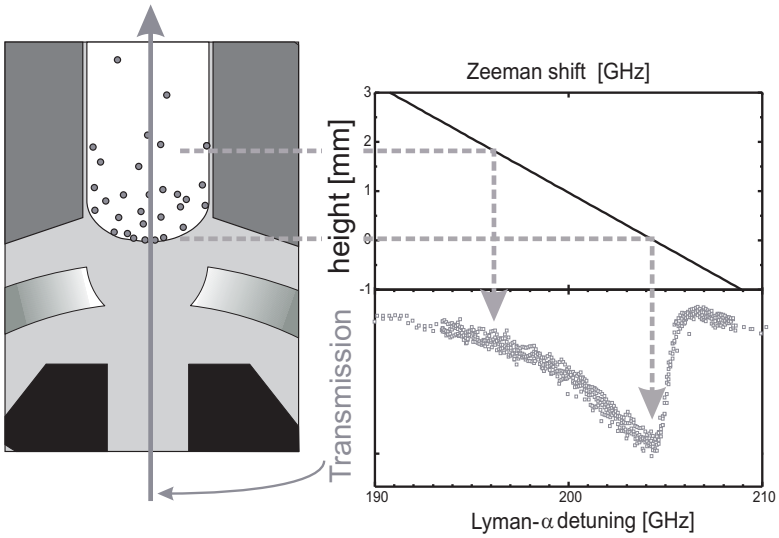

Figure 3.4: The line shape of the σ_4 absorption line due to the atoms in the cell. Left is a drawing of the cell, with the atmospheric density profile. Upper graph: Zeeman shift (x axis) versus height (y axis). Lower graph: Measured line shape. Due to the linear field gradient, the line shape reflects the density profile.

From this lineshape the temperature T_3 can be determined. In the temperature regime of interest the Zeeman width is ≈ 5 GHz, much larger than the 0.6 GHz Doppler width (3.16), therefore the temperature is most accurately determined from the absorption spectrum on a strongly Zeeman broadened line. The fluorescence spectrum does not yield accurate thermometry information as the collection efficiency of the fluorescence detector drops sharply at a height comparable to the atmosphere height.

3.6.2 Hyperfine composition of the gas

The hyperfine splitting between the a and b ground states of H is ≈ 0.7 GHz in the fields under consideration, while the hyperfine splitting of the P and D excited states is negligible, there is only the $\approx$ 100MHz nuclear Zeeman effect [1, 10]. Therefore the Lyman-α lines show hyperfine structure, the lines due to the atoms in the a state are at a frequency which is ≈ 0.6 GHz higher than the corresponding excitation from the b state. This can in principle be used to determine the ratio $f_a = a/(a+b)$ in which the a and b hyperfine states are occupied. The Zeeman broadening is too large to detect the subtle hyperfine shift on a Zeeman broadened line. The only Lyman-α line that can in principle be used for determination of f_a is the π_4 line, which is only

very weakly Zeeman broadened in the relevant field range. However, this transition cannot be excited when the light beam is perfectly aligned with the magnetic field. In our case it is weakly visible due to a slight misalignment between the field and the beam. This misalignment may not be constant over the whole apparatus, therefore this line cannot reliably be used to determine the hyperfine composition of the H.

A different method of determining the density of atoms in the a state is by spectroscopy on the hyperfine-enabled transitions, which can be excited from the a state only, see table 3.2. The only hyperfine-enabled line that is not overshadowed by allowed transitions is the σ_* line. This line is very strongly Zeeman broadened, which enables good separation between the buffer volume and compression cell contributions. Its absorption cross-section is very small, and even at very high density it is hardly visible. Furthermore, determination of the a-state fraction from this line would rely heavily on the ability to compare absolute absorption cross-sections in very different areas of the spectrum.

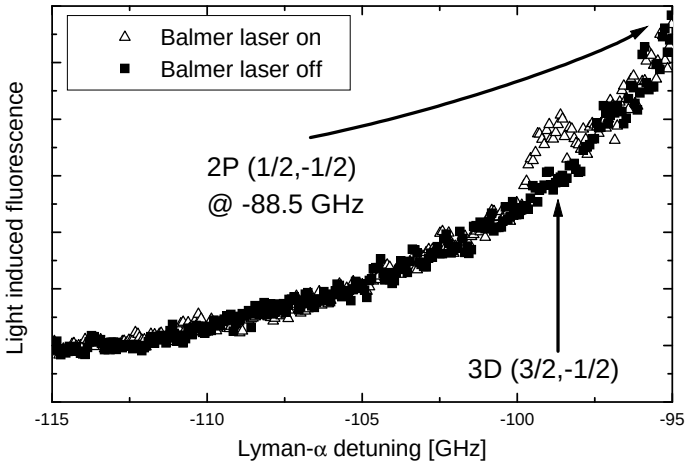

Figure 3.5: Resonance enhanced two-photon fluorescence spectrum of the hydrogen bulk gas in the compression cell. The Balmer-α source is positioned at a blue detuning of a few GHz from the $2P_{1/2,-1/2} \rightarrow 3D_{3/2,1/2}$ transition, while the Lyman-α laser is scanned in the red wing of the $1S_{1/2,-1/2} \rightarrow 2P_{1/2,-1/2}$ line. The polarizations are chosen such that the 'Zeeman free' two-photon transition $1S_{1/2,-1/2} \rightarrow 3D_{3/2,1/2}$, with resonant enhancer $2P_{1/2,-1/2}$, is excited.

A Zeeman free line which can be used to measure the hyperfine composition can be generated in a reliable way by resonance enhanced two-photon spectroscopy (RETS) [10, 29]. This is a scheme to excite levels in the 3S and 3D manifolds by combining

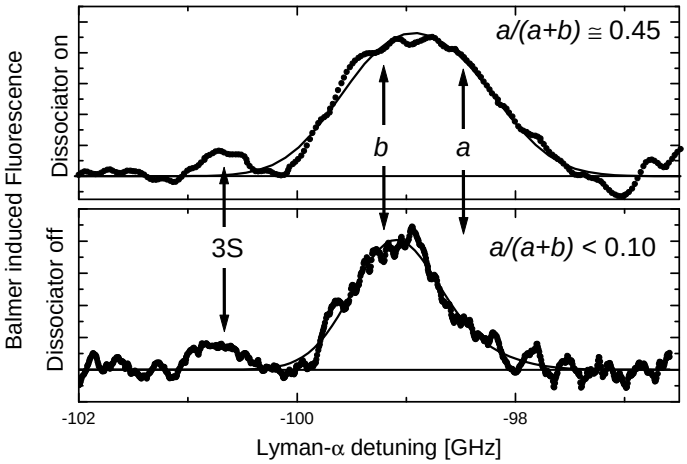

Figure 3.6: Resonance-enhanced two-photon fluorescence spectra of the gas in the compression cell (one photon contribution subtracted). The upper panel shows the spectrum while the dissociator is on and unpolarized gas is injected into the system. Arrows indicate the approximate positions of the (light shifted) resonance lines for the $a, b \rightarrow 3D_{3/2,-1/2}$ RETS transitions, and for the transition to the $3S_{1/2,-1/2}$ state. A fit to the lineshape indicates that 45(10)% of the atoms are in the a state. Lower panel: Spectrum after shutting of the dissociator and cooling the buffer volume for 500 s. The lineshape is narrower now, consistent with less than 10% of the atoms being in the a state.

two photons, one nearly resonant with the 1S-2P Lyman-α transition and one close to the 2P-3S/D Balmer-α transition at 656 nm. A more detailed discussion of the RETS method lies outside the scope of this thesis, the reader is referred to the thesis of Pinkse [10], which provides a full discussion. Using RETS, the 'Zeeman-free' $1S_{1/2,-1/2} \rightarrow 3S_{1/2,-1/2}$ and $1S_{1/2,-1/2} \rightarrow 3D_{3/2,-1/2}$ transitions can be excited, using two photons of opposite circular polarization. A typical spectrum is shown in Fig. 3.5. The signal shown is the light induced fluorescence of the hydrogen atoms. Only the ultraviolet fluorescence was detected, stray Balmer radiation was blocked by means of an optical filter. The signal is selective to atoms in the compression cell only because of the position of the fluorescence detector. We use the lineshape of these transitions to verify the nuclear spin polarization of the gas in the compression cell, as shown in figure 3.6. Due to the Doppler broadening of this two-photon line, excited with copropagating beams, the two hyperfine lines are not resolved, but they are far enough apart to allow determination of the hyperfine polarization to within 10%. As shown in figure 3.6, the RETS spectrum indicates that the gas in the compression cell is hardly hyperfine polarized while the dissociator is on, but becomes polarized to better than 90% after

the dissociator is stopped. This information complements the calculations shown in chapter 5, which indicate that the hydrogen gas reaches a high degree of nuclear polarization (see Fig. 5.5). We used the RETS scheme to verify the development of nuclear spin polarization in a small number of measurements. In the measurements presented in the following chapters the Lyman-α source was used in 'double seed laser' mode (see section 2.3.3), which is presently incompatible with RETS measurements.

References

[1] Jom Luiten, *Lyman-α spectroscopy of magnetically trapped atomic hydrogen*, Ph.D. Thesis, Amsterdam, 1993 (unpublished).

[2] O. J. Luiten, H. G. C. Werij, I. D. Setija, M. W. Reynolds, T. W. Hijmans, and J. T. M. Walraven, *Lyman-α spectroscopy of magnetically trapped atomic hydrogen*, Phys. Rev. Lett. **70**, 544 (1993).

[3] P.W.H. Pinkse, A.P. Mosk, M. Weidemüller, M.W. Reynolds, T.W. Hijmans, and J.T.M. Walraven, *One-dimensional evaporative cooling of magnetically trapped hydrogen*, Phys. Rev. A **57**, 4747 (1998).

[4] P.W.H. Pinkse, A. Mosk, M. Weidemüller, M.W. Reynolds, T.W. Hijmans, and J.T.M. Walraven, *Adiabatically changing the phase-space density of a trapped Bose gas*, Phys. Rev. Lett. **78**, 990 (1997).

[5] Irwan Setija, *Optical cooling of magnetically trapped atomic hydrogen*, Ph.D. Thesis, Amsterdam, 1995 (unpublished),
I.D. Setija, H.G.C. Werij, O.J. Luiten, M.W. Reynolds, T.W. Hijmans, and J.T.M. Walraven, Phys. Rev. Lett. **70**, 2257 (1993).

[6] B. V. Svistunov, T. W. Hijmans, G. V. Shlyapnikov and J. T. M. Walraven, *Resonant-light absorption and the problem of observing the Kosterlitz-Thouless transition in spin-polarized atomic hydrogen adsorbed on a liquid-He surface*, Phys. Rev. B **43**, 13412 (1991).

[7] Ad Lagendijk, Bernard Nienhuis, Bart A. van Tiggelen, and Pedro de Vries, *Microscopic approach to the Lorentz cavity in dielectrics*, Phys. Rev. Lett. **79**, 657 (1997).

[8] Eugene Hecht and Alfred Zajac, *Optics*, Addison-Wesley publishing, Reading, MA (1974).

[9] D. G. Fried, T. C. Killian, L. Willmann, D. Landhuis, S. C. Moss, D. Kleppner and T. J. Greytak, *Bose-Einstein condensation of atomic hydrogen*, Phys. Rev. Lett. **81**, 3811 (1998).

[10] Pepijn Pinkse, *Evaporatively cooled atomic hydrogen investigated by one- and two-photon optical methods*, Ph.D. Thesis, Amsterdam, 1997 (unpublished), chapter 5.

[11] R.G. Beausoleil, D.H. McIntyre, C.J. Foot, E.A. Hildum, B. Couillaud and T.W. Hänsch, Phys. Rev. A **35**, 4878 (1987).

[12] Hans A. Bethe and Edwin E. Salpeter, *Quantum Mechanics of One- and Two-Electron Atoms*, (Plenum Publishing Corporation, New York, 1977).

[13] Claude Cohen-Tannoudji, Jacques Dupont-Roc and Gilbert Grynberg, *Atom-Photon Interactions: Basic Processes and Applications*, (John Wiley & Sons, USA, 1992).

[14] M. Weitz, A. Huber, F. Schmidt-Kaler, D. Leibfried, W. Vassen, C. Zimmermann, K. Pachucki, T.W. Hänsch, L. Julien and F. Biraben, Phys. Rev. A **52**, 2664 (1995). This reference contains the latest value of Rydberg constant.

[15] M. W. Reynolds, estimate of the refractive index of He at 121 nm, private communication.

[16] H.F. Jones, *Groups, representations and physics*, Institute of Physics publishing, Bristol (1990).

[17] R. Eisenschitz and F. London, Zeitschr. f. Physik **60**, 491 (1930).

[18] G.W. King and J.H. van Vleck, *Dipole-Dipole resonance forces*, Phys. Rev. **55**, 1165 (1939).

[19] R.S. Mulliken, *The interaction of differently excited like atoms at large distances*, Phys. Rev **120**, 1674 (1960).

[20] Rodney Loudon, *The Quantum Theory of Light*, Oxford University Press, New York (1983).

[21] J. F. Bukta and W. J. Meath, *Long range interaction energies between ground and first excited state hydrogen atoms using a one centre method*, Mol. Phys. **25**, 1203 (1973).

[22] B.V. Svistunov and G.V. Shlyapnikov, *Resonance optics of the low-temperature quantum gases H and D*, Sov. Phys. JETP **70**, 460 (1990).

[23] A. Jabloński, *General theory of pressure broadening of spectral lines*, Phys. Rev. **68**, 78 (1945).

[24] J. H. Van Vleck and D. L. Huber, *Absorption, emission, and linebreadths: A semihistorical perspective*, Rev. Mod. Phys. **49**, 939 (1977).

[25] V. Weisskopf, Phys. Z. **34**, 1 (1933).

[26] Alan Corney, *Atomic and laser spectroscopy*, (Clarendon press, Oxford, 1977).

[27] Yu. Kagan, B. V. Svistunov and G. V. Shlyapnikov, *Quantum correlations in the optical characteristics of low-temperature H and D gases*, JETP Lett. **48**, 56 (1988).

[28] I. F. Silvera and J. T. M. Walraven, *Spin Polarized Atomic Hydrogen*, in *Progress in Low Temperature Physics*, edited by D. F. Brewer (Elsevier, Amsterdam 1986), Vol. 10, p. 139.

[29] P.W.H. Pinkse, A. Mosk, M. Weidemüller, M.W. Reynolds, T.W. Hijmans, J.T.M. Walraven and C. Zimmermann, *Resonance enhanced two-photon spectroscopy of magnetically trapped atomic hydrogen*, Phys. Rev. Lett., **79**, 2423 (1997).

[30] A. I. Safonov, S. A. Vasilyev, I. S. Yasnikov, I. I. Lukashevich, and S. Jaakkola, *Magnetic compression of two-dimensional spin-polarized atomic hydrogen* JETP Lett. **61**, 1032 (1995), same authors and E. Tjukanov, LT21, Czech. J. Phys. **46**, 539 (1996).

[31] G. Herzberg, *Molecular Structure and Molecular Spectra, I. Spectra of Diatomic Molecules*, D. van Nostrand, New York, 1950.

[32] R. van Roijen, *Atomic hydrogen in a magnetic trap*, Ph. D. thesis, University of Amsterdam (1989) (unpublished),
R. van Roijen, J.J. Berkhout, S. Jaakkola, and J.T.M. Walraven, Phys. Rev. Lett. **61**, 931 (1988).

[33] T. J. Greytak, in *Bose-Einstein condensation*, ed. A. Griffin, D. W. Stroke and S. Stringari, Cambridge University Press, Cambridge GB, (1995).

[34] A. P. M. Matthey, J. T. M. Walraven and Isaac F. Silvera, *Measurement of pressure of gaseous* H↓*: Adsorption energies and surface recombination rates on helium*, Phys. Rev. Lett. **46**, 668 (1981).

[35] M. W. Reynolds, I. Shinkoda, W. N. Hardy, A. J. Berlinsky, F. Bridges, and B. W. Statt, *Electron-spin-resonance studies of spin-polarized hydrogen on the surface of liquid* ^{4}He, Phys. Rev. B **31**, 7503 (1985).

[36] M. Morrow, R. Jochemsen, A. J. Berlinsky, and W. N. Hardy, *Zero-field hyperfine resonance of atomic hydrogen for* $0.18 < T < 1\,\mathrm{K}$*: The binding energy of* H *on liquid* ^{4}He, Phys. Rev. Lett **46**, 195 (1981).

Chapter 4

Optical excitation of atomic hydrogen bound to the surface of liquid helium

We have optically detected hydrogen atoms adsorbed on the surface of liquid helium, a system relevant for the study of Bose degeneracy in two dimensions. The atoms are excited by 121.6 nm light and detected both in fluorescence and in absorption. The excitation spectrum shows a resonance that is much broader than that of a free atom, and shifted to lower frequencies. From the absorption signal we determine that we have reached a surface density corresponding to one atom per square De Broglie wavelength. We also use the hydrogen fluorescence to probe the thermal contact between the free surface and the bulk of the liquid helium, which we compare with ripplon-phonon coupling theory.
[This chapter has been published as: A. P. Mosk, M. W. Reynolds, T. W. Hijmans and J. T. M. Walraven, Phys. Rev. Lett. **81**, 4440 (1998).]

4.1 Introduction

Spin-polarized atomic hydrogen adsorbed on the surface of liquid helium is a unique example of a two-dimensional (2D) atomic gas. This 2D gas is exceptionally stable which allows for the accumulation of large surface densities. In addition the atoms

are so weakly bound to the helium surface that is possible to maintain an equilibrium between the adsorbed gas and the 3D gas of non-adsorbed H atoms. These properties make it a ready model system for investigating quantum degenerate behavior in two dimensions.

The goal of reaching the quantum degenerate regime in the 2D Bose gas of adsorbed H has been the subject of several studies (see e.g. Refs. [1, 2]). Recently, this goal has been achieved [3]. Crucially however, in these experiments the 2D Bose gas itself has only been observed by indirect means. The surface density was inferred from recombination rates. The geometry required to approach degeneracy involves compressing the gas onto a small effective surface in a strongly inhomogeneous magnetic field, making magnetic resonance techniques (as used in e.g. Ref. [4]) unsuitable. As a consequence, direct observation of the 2D gas is a non-trivial matter. In this paper we present the first measurements in which we have direct access to the compressed surface gas in such a geometry. For this purpose we use resonant optical spectroscopy of the adsorbed H atoms near the 1S-2P (Lyman-α) transition. The adsorbed atoms were anticipated to give rise to a surface specific fluorescence signal [5, 6] but the precise frequency, line shape, and width of the resonance were not known in advance. In this letter we show that the fluorescence spectrum can be used to determine the surface density under the conditions relevant for studies of 2D quantum degeneracy.

In our experiments we obtain a 2D degeneracy parameter $n_2\Lambda^2$ close to unity, where n_2 is the surface density and Λ the thermal de Broglie wavelength. This means we are at the edge of the quantum degenerate regime. Theory predicts a Kosterlitz-Thouless (KT) type phase transition to superfluidity at $n_2\Lambda^2 \approx 4$. The formation of a quasi-condensate is predicted to occur close to this transition [5].

We use the adsorbed H atoms to probe the coupling between the excitations of the He surface (ripplons) and those of the bulk liquid (phonons) [7]. This coupling determines the temperature of the surface in the presence of recombination heating. The surface density depends exponentially on temperature. As a consequence the thermal resistance between the ripplons (to which the H atoms couple strongly) and phonons turns out the be the dominant constraint on achievable phase space densities. We find good agreement between our observations and theory describing ripplon-phonon coupling.

In our experiments we determine, in addition to n_2, two other relevant thermodynamic quantities: the temperature T, and the density n_3 of atoms in the 3D gas above the surface. The 3D gas density fixes the chemical potential, thus giving access to the equation of state of the 2D Bose gas. Following Ref. [5] this equation of state

can be written in the following slightly simplified form:

$$n_3\Lambda^3 = \left(1 - e^{-n_2\Lambda^2}\right) \exp\left(\frac{-E_b + (2-\Theta)\tilde{U}n_2}{k_{\rm B}T}\right). \tag{4.1}$$

Here $\Lambda \equiv (2\pi\hbar^2/mk_{\rm B}T)^{1/2}$ with m the atomic mass, $E_b/k_{\rm B} = 1.01$K [8] is the binding energy of H on ^{4}He, and $\tilde{U}/k_{\rm B} = 5 \times 10^{-15}$K cm^2 [9], is the calculated effective interaction vertex between adsorbed atoms. The parameter Θ is a measure of the quasi-condensate density; Θ is zero in the absence of a quasi-condensate and becomes approximately one when $T \to 0$. Hence, Eq. (4.1) can be used as a telltale for a possible transition to a Bose condensed state.

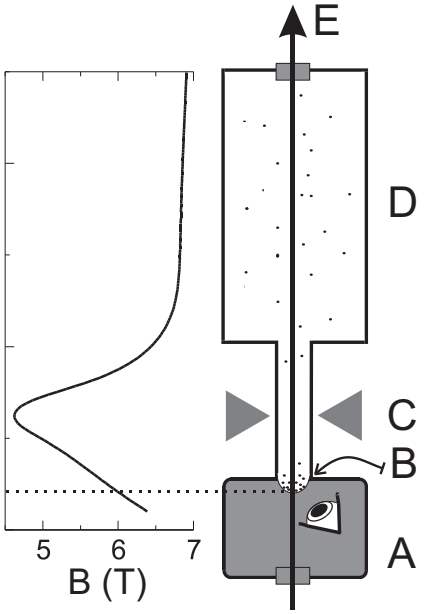

Figure 4.1: Schematic drawing of the cryogenic apparatus showing: **A** the He filled cell (T=0.08K, effective area 4 mm^2), **B** the He meniscus with the high density H, **C** the magnetic potential barrier (pinch), **D** the buffer volume (T=0.2 - 0.4K, effective volume 30 cm^3), **E** the path of the light beam. Plotted alongside is the magnitude of the magnetic field, B, on the axis of the system. The magnetic field is essentially vertical everywhere.

4.2 Apparatus

Our cryogenic apparatus [10] is shown schematically in Fig. 4.1. The H is stabilized by a magnetic field of several tesla and a liquid helium film wetting all surfaces. The apparatus consists of a small cold region called the cell, in which the atoms adsorb on a meniscus of bulk liquid helium, and a warmer buffer volume, which acts as a source of doubly (electron and nuclear spin) polarized H for the cell. The cell is cooled to 0.08 K, while the temperature of the buffer volume can be regulated between 0.15 and 0.4 K.

A superconducting magnet and iron pole pieces create a magnetic field profile as shown in Fig. 4.1. This provides a high field in the buffer volume, a strong field gradient in the cell and a deep dip in the field in between the buffer volume and the cell, which acts as a barrier for spin-down H atoms moving between the buffer volume and the cell.

A cryogenic dissociator in low field produces a flux of 10^{13} atoms per second into the buffer volume. These atoms are in the high field seeking a ($F = 0$) and b ($F = 1, m_F = -1$) hyperfine states. Importantly, although the cell is much smaller than the buffer volume, it determines the loss of atoms because it is at lower temperature. The two and three body decay rates are dominated by recombination on the surface. Hence, it follows from Eq. (4.1) that in the non-degenerate case they are proportional to $(n_2)^2 \propto \exp(2E_b/k_\mathrm{B}T)$ and $(n_2)^3 \propto \exp(3E_b/k_\mathrm{B}T)$, respectively.

The main two-particle recombination processes for adsorbed atoms are $a+a \rightarrow \mathrm{H}_2$ and $a + b \rightarrow \mathrm{H}_2$. The first leads to polarization of the gas to the b state, the second leads just to loss of density. The process $b + b \rightarrow \mathrm{H}_2$ is forbidden. Three body processes become dominant over the $a + b$ recombination only after a substantial degree of nuclear polarization has been achieved. Once the nuclear spin polarization is sufficient, we heat the buffer volume so that the flux of atoms to the cell increases. The density in the cell is then built up by this forward flux, until it reaches a stationary state due to the backward flux (from the cell to the buffer volume) and the three particle recombination process $b + b + b \rightarrow \mathrm{H}_2 + \mathrm{H}$ of the adsorbed atoms in the cell. Because the cell is much colder than the buffer volume, the backward flux is inhibited and the density in the cell becomes much higher than that in the buffer volume.

4.3 Spectroscopy

We use narrowband vacuum ultraviolet (VUV) light to determine the densities n_2 and n_3 and the temperature T in the cell as well as the density of the gas in the

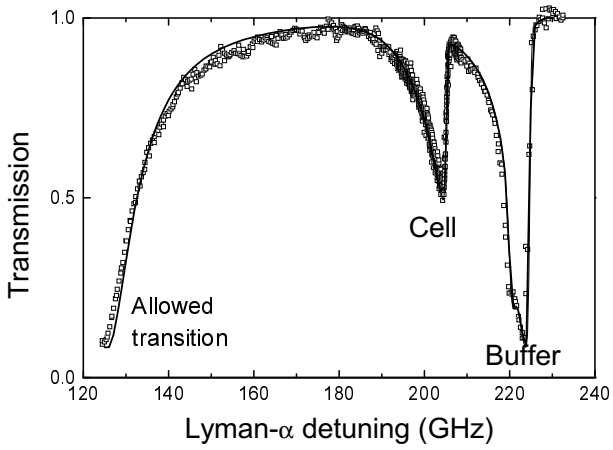

Figure 4.2: 3D H transmission spectrum on the nearly forbidden $1S_{1/2,-1/2} \rightarrow 2P_{3/2,1/2}$ transition. Squares: Experimental data, Line: Calculated spectrum for $T = 0.122$K, $n_3 = 1.3 \times 10^{15}\text{cm}^{-3}$, polarization of the light 93% σ_+ The strong feature on the left is the far wing of the allowed $1S_{1/2,-1/2} \rightarrow 2P_{1/2,1/2}$ line.

buffer volume. We produce this VUV radiation at 121.6 nm wavelength by frequency tripling of a pulsed UV laser source [11]. The VUV light traverses the compression cell and the buffer volume on the axis of the system. A room temperature photomultiplier tube (PMT) detects the transmitted light. We can also record light-induced fluorescence (LIF) spectra by scanning the laser frequency. The scattered light is frequency downconverted to visible wavelengths in the cell and guided to a second PMT by means of an optical fiber bundle.

As the magnetic field is parallel to the direction of propagation of the light, only σ_+ ($\Delta m_J = 1$) and σ_- ($\Delta m_J = -1$) transitions can be excited. Moreover, as the field is high ($> 6\,$T) spin-orbit coupling is weak and the $1S_{1/2,-1/2} \rightarrow 2P_{3/2,1/2}$ transition is strongly suppressed and remains nonsaturated even when allowed lines are extremely optically thick. In Fig. 4.2 we show a spectrum of this line. The different magnetic fields in the compression cell and the buffer volume split the line into two distinguishable components. The strongly inhomogeneous field in the cell gives rise to a temperature dependent Zeeman broadening (on the red wing of the cell line) which we fit against calculated spectra to determine the temperature of the 3D gas.

Our measurements of the spectrum of the adsorbed atoms, performed with σ_- polarization, show a ≈ 300 GHz broad line, which can be seen both in LIF and in

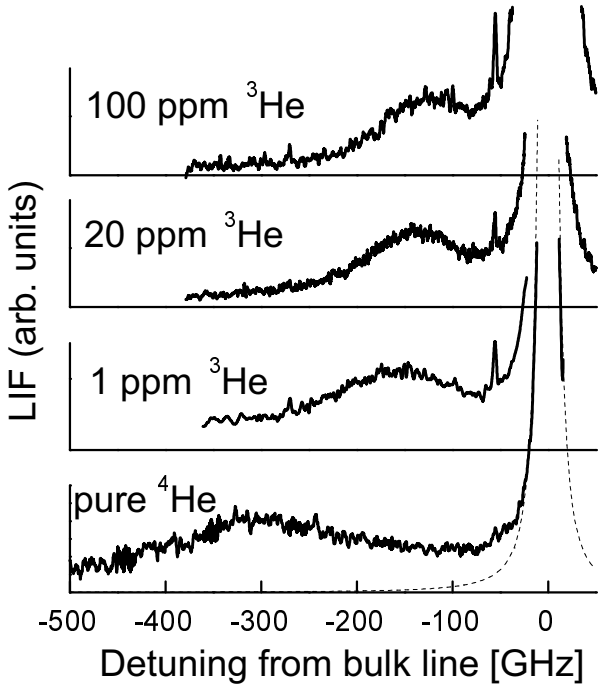

Figure 4.3: LIF excitation spectrum of the adsorbed atoms at different concentrations of ^{3}He. The dotted line is a Lorentzian fit to the bulk line. The narrow peak at -50 GHz is due to photoassociation of H atoms in the bulk.

transmission and which is shifted ≈ 300 GHz to the red of the allowed σ_- bulk line. A similar feature is observed with σ_+ light but it is obscured by a coincident 3D H line. The bottom panel in Fig. 4.3 shows the LIF signal of the σ_- surface line.

4.4 Surface density

The observed line shift and broadening are very small compared to the detunings with respect to all other optical transitions in H and He. Therefore, in analogy with pressure broadening in a gas, we assume that the He-H interaction conserves the oscillator strength of the Lyman-α transition to a good approximation. This assumption, together with the measurement of the optical extinction spectrum of the surface atoms enables us, in principle, to obtain an absolute calibration of n_2. However, parts of the line are masked by the much stronger 3D H lines, or lie outside the scanning range of our light source. Integrating the visible part of the 2D H optical

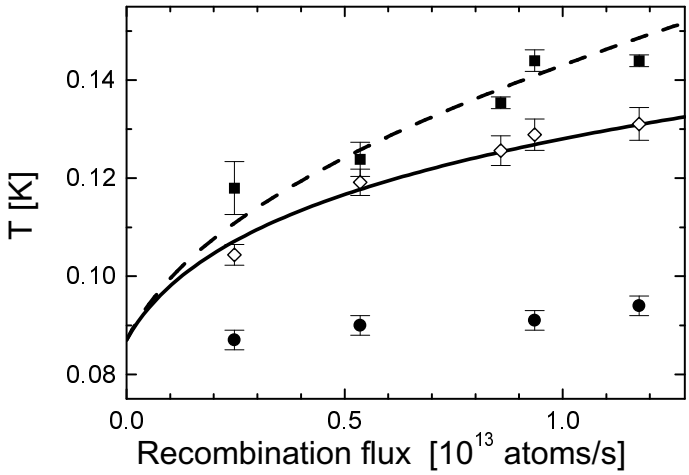

Figure 4.4: Temperatures of the 3D H (squares), the He surface (diamonds) and the He bulk (circles) as a function of the recombination flux. The solid curve is the surface temperature predicted by ripplon–phonon coupling theory [13], the dashed curve is the predicted 3D gas temperature. The He temperatures may be offset by $\pm 5\,\mathrm{mK}$ due to an uncertainty in the calibration of the thermometer.

resonance therefore provides us with a lower bound to n_2. We can also establish an upper bound to n_2 from the rate of recombination, as follows: In the case of perfect nuclear spin polarization, n_2 can be inferred from the known rate of $b + b + b$ recombination [12]. If the polarization is imperfect, the recombination is necessarily faster for a given n_2, and the inferred n_2 will be an upper bound. We find this upper bound to be only 25% higher than the lower bound determined optically.

4.5 Thermal boundary resistance

Eq. (4.1) suggests that quantum degeneracy will be reached if the flux from the buffer volume into the compression cell is simply increased at fixed cell temperature. This increases n_3 and n_2 will adjust accordingly. Unfortunately this picture is too simple because it neglects the temperature rise of the surface due to increased recombination. This temperature rise in turn reduces n_2. To interpret our measurements we introduce three temperatures: the temperature T_3 of the 3D gas, the temperature T_2 of the 2D gas, and the temperature T_{He} of the bulk helium. Two of these three temperatures are directly accessible experimentally: T_3 is determined spectroscopically (from the Zeeman broadened line shape) and T_{He} is measured with a resistance thermometer

inside the liquid. In addition we are able to determine T_2 from our spectroscopic measurements of n_2 and n_3. The temperature drop between the 3D H and the surface is small enough that solving Eq. (4.1) for T yields a good estimate of the surface temperature. For larger temperature drops, T_2 can be inferred from the more general equations in Ref. [5].

Fig. 4.4 shows the three temperatures T_3, T_2, and T_{He} as functions of the recombination rate. This rate follows directly from the decay of the total number of atoms in the apparatus. It is clearly seen that the temperatures become different as the recombination rate increases. This can be understood quantitatively as follows.

In a three-body recombination event only a small fraction (less than 1.4% [2]) of the 4.5eV binding energy of H_2 is deposited to the surface as heat, the rest is carried away as molecular internal energy. Subsequently, the excited molecule requires ≈ 150 wall collisions to release half its energy [12]. During its excited lifetime, the molecule may return to the helium meniscus and deposit part of its energy there. Assuming diffuse scattering of molecules from the walls, we calculate that in our cell the molecules deposit 3% of the recombination energy on the surface of the meniscus. This gives rise to a temperature drop between the surface and bulk of the liquid helium. The magnitude of the temperature drop we find here confirms that the ripplons of the He surface are weakly coupled to the phonons in the superfluid [7]. Using the theoretical boundary resistance between ripplons and phonons [13] we calculate the expected temperature of the helium surface. The result, with no adjustable parameters, is plotted in Fig. 4.4.

In addition to the surface being warmer than the bulk, the 3D H gas is warmer than the surface. This is due to direct heating of the H by collisions with excited H_2. The observed heating implies an *effective* cross section of $0.007\,\text{Å}^2$ for full (4.5 eV) energy release. Arvela et al. [14] reported a similar value.

The heating of the surface limits the presently attainable phase-space densities to the edge of the quantum degenerate regime. Our highest degeneracy parameter is $n_2\Lambda^2 = 0.9(1)$. To extend our experiments into the degenerate regime will require a cell with more opportunity for disposal of excited H_2 away from the recombination region. It is necessary to make the meniscus smaller to reduce the recombination area, and to change the geometry of the cell to reduce the probability for molecules to return to the meniscus. Based on our measurements of the thermal impedance, we expect that we can make these improvements while maintaining the ability to study the two-dimensional gas optically.

4.6 The spectrum of the adsorbed atoms

Finally, we comment on the nature of the adsorbed atom spectral line. As is seen in Fig. 4.3 the line shift and line width change when we add ^{3}He atoms. Apparently, the line width and shift are proportional to the binding energy of the ground state H atoms, which is reduced from 1.01K on ^{4}He to ≈ 0.4K on a surface saturated with ^{3}He [8]. The line shift is ≈ 15 times larger than this binding energy. Qualitatively, this factor can be attributed to the larger polarizability of the excited atom, leading to stronger van der Waals attraction.

In ref. [6], the possibility of the existence of long-lived bound states of the 2P atom on the He surface was examined theoretically. It was predicted that such a state would give rise to a sharp (only radiatively broadened) line at a red detuning of 180 GHz from the bulk line. The line shift is qualitatively correct, but the observed line is broader by a factor more than 1000. This broadening cannot be dominated by nonradiative decay (predissociation), as we find the fluorescent yield FY to be high, FY $= 0.5(1)$.

Also, at the densities encountered, line broadening by H-H interactions is neither expected nor observed. A possible line-broadening mechanism, suggested for alkali atoms adsorbed on helium clusters, is reconfiguration of the helium surface after optical excitation [15]. However, in this case nonradiative decay seems inevitable. In view of the high FY we propose another mechanism, viz., that a HeH* dimer is formed and is ejected from the surface (it can be formed in a state of ejection or it can be initially bound and eject itself from the surface while de-exciting vibrationally). As the polarization of the light is in the plane of the surface the dimer would be formed in the $B^2\Pi$ state preferentially. This state decays radiatively in vacuum [16].

This work is part of a research program of the Stichting voor Fundamenteel Onderzoek der Materie (FOM), which is a subsidiary of the Nederlandse Organisatie voor Wetenschappelijk Onderzoek (NWO). The research of MWR is supported by the Royal Netherlands Academy of Arts and Sciences (KNAW).

References

[1] A. I. Safonov, S. A. Vasilyev, I. S. Yasnikov, I. I. Lukashevich, and S. Jaakkola, *Magnetic compression of two-dimensional spin-polarized atomic hydrogen*, JETP Lett. **61**, 1032 (1995), same authors and E. Tjukanov, LT21, Czech. J. Phys. **46**, 539 (1996).

[2] A. Fukuda, M. Yamane, A. Matsubara, T. Arai, J.S. Korhonen, J. T. M. Walraven, and T. Mizusaki, *Cooling of two-dimensional spin-polarized atomic hydrogen*, LT 21, Czech. J. Phys. **46**, 541 (1996).

[3] A. I. Safonov, S. A. Vasilyev, I. S. Yasnikov, I. I. Lukashevich and S. Jaakkola, *Observation of quasicondensate in two-dimensional atomic hydrogen*, Phys. Rev. Lett. **81**, 4545 (1998).

[4] M. W. Reynolds, I. Shinkoda, W. N. Hardy, A. J. Berlinsky, F. Bridges, and B. W. Statt, *Electron-spin-resonance studies of spin-polarized hydrogen on the surface of liquid* ^{4}He, Phys. Rev. B **31**, 7503 (1985).

[5] B. V. Svistunov, T. W. Hijmans, G. V. Shlyapnikov and J. T. M. Walraven, *Resonant-light absorption and the problem of observing the Kosterlitz-Thouless transition in spin-polarized atomic hydrogen adsorbed on a liquid-He surface*, Phys. Rev. B **43**, 13412 (1991).

[6] M. W. Reynolds and J. T. M. Walraven, *Optical excitation of atomic hydrogen adsorbed on liquid helium*, Physica B **194-196**, 905 (1994). Note: The $A, C^2\Sigma^+$ curves were based on incorrect potentials; the $B^2\Pi$ curve relevant here is not affected.

[7] D. O. Edwards and W. F. Saam, *The Free Surface of Liquid Helium*, in *Progress in Low Temperature Physics*, edited by D. F. Brewer (North-Holland, Amsterdam 1978), Vol. VII, p. 284.

[8] I. F. Silvera and J. T. M. Walraven, *Spin Polarized Atomic Hydrogen*, in *Progress in Low Temperature Physics*, edited by D. F. Brewer (Elsevier, Amsterdam 1986), Vol. 10, p. 139.

[9] D. O. Edwards and I. B. Mantz, *The adsorption of atomic hydrogen to the surface of* ^{4}He, supplement **C7** of Journal de Physique **41**, 257 (1980).

[10] A. P. Mosk, P. W. H. Pinkse, M. W. Reynolds, T. W. Hijmans and J. T. M. Walraven, *Apparatus for the Optical Study of Atomic Hydrogen on the Surface of Liquid Helium* QFS97, J. Low Temp. Phys. **110**, 199 (1998). Note: the last term of Eq. (1) should read $(t^2/s^3)\ln[(\tilde{z}_1 + r_1 s + a_1 t)/(\tilde{z}_2 + r_2 s + a_2 t)]$.
The information in this article is included in chapter 2 of this thesis.

[11] O. J. Luiten, H. G. C. Werij, M. W. Reynolds, I. D. Setija, T. W. Hijmans and J. T. M. Walraven, Appl. Phys. B **59**, 311 (1994).

[12] S. A. Vasilyev, E. Tjukanov, M. Mertig, A. Ya. Katunin, and S. Jaakkola, *Distribution of Surface Recombination Energy of Spin-Polarized Hydrogen on Liquid Helium,* Europhys. Lett. **24**, 223 (1993).

[13] M. W. Reynolds, I. D. Setija and G. V. Shlyapnikov, *Energy transfer between ripplons and phonons in liquid helium at low temperatures,* Phys. Rev. B **46**, 575 (1992).

[14] P. Arvela, A. V. Frolov, S. Jaakkola, A. Ya. Katunin, I. I. Lukashevich, M. Mertig, M. W. Reynolds, A.I. Safonov, E. Tjukanoff, T. Tommila, and S. A. Vasilyev, Phys. Rev. B (*to be published*).

[15] F. Stienkemeier, J. Higgins, C. Callegari, S. I. Kanorsky, W. E. Ernst, and G. Scoles, Z. Phys. D **38**, 253 (1996).

[16] J. R. Peterson and Y. K. Bae, Phys. Rev. A **34**, 3517 (1986).

Chapter 5

Population dynamics and heat exchange

All quantum gases that have been created are metastable with respect to inelastic collisions between the atoms. In the case of adsorbed H these inelastic processes lead to formation of molecules, causing loss of atoms and production of heat. Typically the whole adsorbed hydrogen sample would be destroyed by recombination processes in a matter of milliseconds if the adsorbate would not be replenished from the surrounding bulk gas. In fact there is a continuous exchange of atoms and energy between the adsorbed gas and the surrounding bulk gas in the compression cell. The gas in the compression cell in turn exchanges atoms with the population in the buffer volume. These fluxes of atoms and heat can be modeled, as many of the elementary processes that occur have been measured in dedicated experiments, or can be predicted with confidence from theory. Models of the population dynamics, in the form of a set of rate equations, have been used successfully to describe the results of experiments with high-density H in cryogenic cells, as for example in Ref. [35] and [10]. A detailed model of the population dynamics and heat exchange in our apparatus serves three purposes:

- First and foremost, it enables us to understand the behavior of the gas sample. We made several measurements of gas densities, temperatures and their time dependence. The processes by which hydrogen atoms are transported through the cell, adsorb, desorb and recombine are relatively well understood, and the measured behavior should agree with the behavior expected from the population dynamics model.

- Secondly, it gives insight into limitations of the present apparatus, and it can be used to generate improvements. The maximum attainable phase space density in our apparatus depends critically on the transport of atoms and heat through the system. If the atoms lost due to recombination cannot be replaced quickly enough, or if the recombination heat cannot be removed from the sample efficiently enough, the range of phase space densities that can be reached is severely limited. In the present compression cell, the degenerate regime was found to be just out of reach. A detailed model of the transport properties in the present apparatus can be used to improve the design of the compression cell.
- Thirdly, the model allows us to study recombination losses in the sample. The recombination rate constants depend on two- and three atom correlators which are sensitive to quantum effects. By comparing the recombination processes to model predictions, we will obtain more information about a prospective degenerate sample. In fact, in the experiment by Safonov *et al.* [4], in which the first degenerate two-dimensional atomic hydrogen sample was produced, the recombination processes were the major source of information about the sample.

Our apparatus has strongly inhomogeneous magnetic fields inside it, and a large temperature difference between the buffer volume and the compression cell. As a consequence, the rate equations describing the population dynamics model will be rather complicated, and involve many rate constants. Nevertheless, since hydrogen is a well-studied system, most rate constants are well known, and predictions of the population dynamics depend only on a few parameters. Moreover, it will be shown that in steady state, the density in the gas sample is stabilized by strong negative feedback: Attempts to increase the density of the gas in the compression cell will also increase the temperature, which will lead to a reduction of the density of the adsorbed gas. Therefore, the steady state temperature and density do not depend critically on any parameter in the model, and the predictions are relatively robust.

5.1 Outline of this chapter

The description of the population dynamics starts by defining the relevant variables and rate equations in section 5.2. Effective volumes are introduced in section 5.2.3, and the correct temperature dependence of the effective area is analyzed in section 5.2.4. The adsorption equation, which describes adsorption and desorption of H atoms, is discussed in section 5.3, where we also analyze corrections to the adsorption equation due to imperfect hyperfine polarization of the gas, temperature gradients

and recombination loss.

In section 5.4 we discuss all other terms in the rate equations which model the compression cell, and in section 5.6 we examine the predictions of this model, and compare them to experimental data. It is found that the rate equations describe the behavior of the gas sample accurately, and that they also offer insight into the limitations on the phase-space density.

Finally, in section 5.7 we apply our model to the design of an improved compression cell. An important unknown parameter for this design is the fraction of energy released at the site of recombination in a recombination event, f_{dir}. It is shown that for realistic values of f_{dir}, heat removal by ripplons (thermal surface waves) is essential for achieving quantum degeneracy. In section 5.7.1 an estimate of the efficiency of ripplon heat conductance followed by ripplon-phonon conversion is made. In section 5.7.2, an estimate of f_{dir} is made on the basis of an experiment conducted by the Turku group [16]. Finally this estimate is used to predict the effect of modifications of compression cell, which have been proposed for future experiments. According to the present model, it should be possible to reach quantum degeneracy in a revised compression cell.

5.2 Definitions

5.2.1 Population numbers and rate equations

To model the sample in our apparatus we keep track of the populations of atoms in each hyperfine state in the compression cell and the buffer volume. In the compression cell the atoms can be either in the bulk gas or adsorbed to the surface, while in the buffer the number of adsorbed atoms is always negligible. Therefore there are six relevant population numbers $N_i^{(h)}$. Here h denotes the hyperfine state (a or b) and the index i indicates the subpopulation, where $i = 2$ refers to the adsorbate, $i = 3$ to the bulk gas in the cell and $i = B$ refers to the atoms in the buffer volume. Figure 5.1 schematically indicates these populations, as well as the exchange fluxes $\Phi_{i\to j}^{(h)}$ between them, and the loss fluxes $R_j^{(h)}$ due to recombination. A rate equation for each of the population numbers $N_i^{(h)}$ reflects the following processes:

- The production of atoms by the dissociator, producing Φ_D atoms/s,
- The flux of atoms from buffer volume to compression cell ,$\Phi_{B\to 3}$ [atoms/s],
- The flux of atoms from cell to buffer volume ,$\Phi_{3\to B}$ [atoms/s],

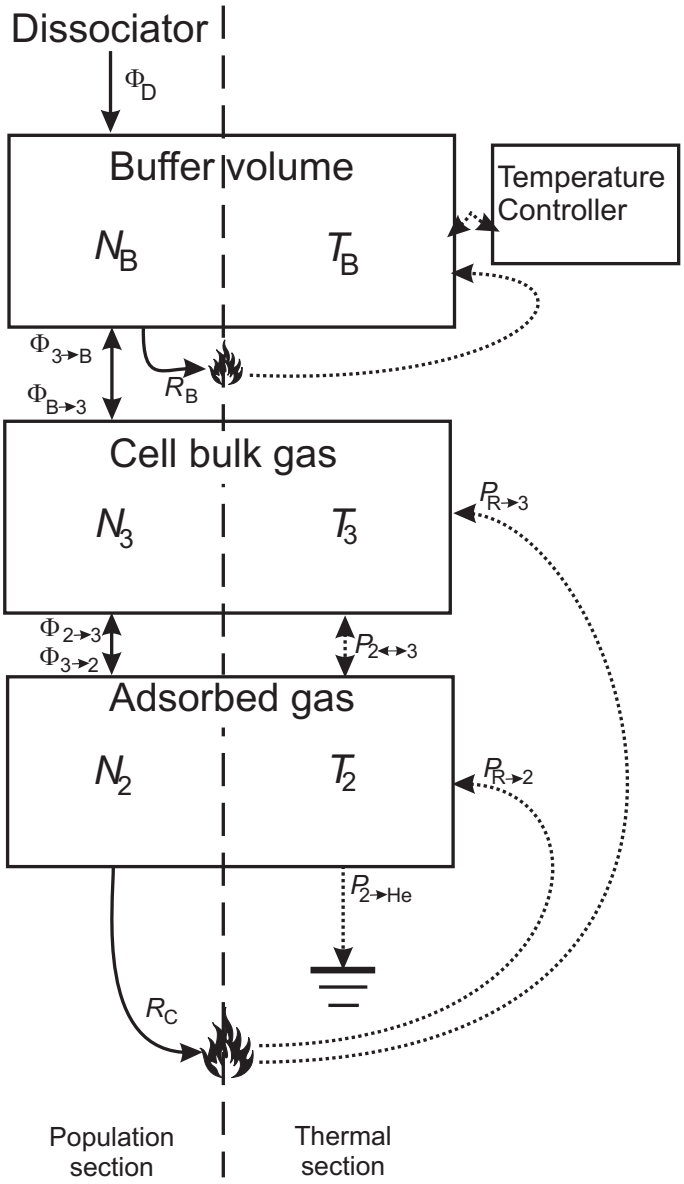

Figure 5.1: Schematic showing the populations and atom fluxes (solid arrows, left panel) in the apparatus, as well as the heat fluxes (dashed arrows, right panel). The dissociator is a source of atoms, the recombination processes 'burn' atoms (leading to a loss of $R_B + R_C$ atoms per second) and generate heat, indicated by the recombination powers $P_{R\to i}$.

- The adsorption flux $\Phi_{3\to 2}$, which represents the number of atoms per second adsorbing to the helium surface, and the desorption flux $\Phi_{2\to 3}$,
- Atom loss due to recombination in the buffer volume, leading to a loss of R_B atoms/s,
- Recombination loss on the cell surface, leading to a loss of R_C atoms/s,
- Depolarization of the nuclear spins in buffer volume and cell.

Taking all terms into account the rate equations for the populations $N_3^{(h)}$ in the cell bulk gas, $N_2^{(h)}$ on the surface and $N_B^{(h)}$ in the buffer volume read

$$\frac{d}{dt}N_3^{(a,b)} = \Phi_{B\to 3}^{(a,b)} - \Phi_{3\to B}^{(a,b)} - \Phi_{3\to 2}^{(a,b)} + \Phi_{2\to 3}^{(a,b)} - G_{\text{cell}}^{\text{eff}}(N_3^{(b,a)} - N_3^{(a,b)}), \quad (5.1)$$

$$\frac{d}{dt}N_2^{(a,b)} = \Phi_{3\to 2}^{(a,b)} - \Phi_{2\to 3}^{(a,b)} - R_C^{(a,b)}, \quad (5.2)$$

$$\frac{d}{dt}N_B^{(a,b)} = \frac{1}{2}\Phi_d - \Phi_{B\to 3}^{(a,b)} + \Phi_{3\to B}^{(a,b)} - R_B^{(a,b)} + G_B^{\text{eff}}(N_B^{(b,a)} - N_B^{(a,b)}). \quad (5.3)$$

Here G_B^{eff},G_C^{eff} are the effective rate constants for nuclear spin relaxation. We assume that this relaxation is dominated by the effects of impurities in the walls, and therefore this is taken to be a one-atom effect. The G's represent the probability per second for each atom that its nuclear spin will be flipped by interaction with an impurity. Although the nuclear spin relaxation is probably only relevant for adsorbed atoms, it is more convenient to represent it as an effective bulk rate.

5.2.2 Heat exchange equations

In the recombination process a large amount of heat is released, approx. 26000 K $\times k_{\text{B}}$ per atom. This heat flux will change the temperature locally, and thereby influence the exchange fluxes. As a result, the population rate equations cannot be viewed independently from the heat exchange in the apparatus. There are several thermal reservoirs, which may be at different temperatures, as indicated in figure 5.1:

- The buffer volume, which is externally temperature controlled at temperature T_B. The contact surface between the walls of this volume and the gas inside it is large, and the recombination rate inside it is low, so that we expect the gas inside to be in thermal equilibrium with the walls at T_B.
- The bulk helium liquid in the compression cell. The temperature T_{He} of this liquid is determined by means of an immersed thermometer.
- The helium surface and the adsorbate, at temperature T_2. The temperature of the helium surface may be different from that of the bulk liquid as the thermal contact between the surface excitations (ripplons) and the bulk excitations

(phonons) is very weak [12]. The surface excitations couple very well to the adsorbed H atoms [23], therefore we expect them to be at the same temperature.

- The bulk H↓ gas in the compression cell, at temperature T_3. This gas is heated by excited molecules which are formed in recombination processes on the surface. The thermal contact between the gas and the helium surface is rather poor [3, 11], therefore T_3 will in general be higher than the surface temperature.

We assume that each of these subsystems is in internal thermal equilibrium.

The heat capacity of these subsystems determines the timescale of their response to changes in the heat-loads. The heat capacity C_3 of the bulk gas in the cell at constant number of particles is easily calculated using the expression from [20],

$$C_3 \equiv \left(\frac{\partial E}{\partial T}\right)_N = \frac{5}{2} k_{\mathrm{B}} \left(N_3^{(a)} + N_3^{(b)}\right). \tag{5.4}$$

At a typical density of $n = 10^{15}$ cm^{-3} this yields a heat capacity of $C_3 \approx 2 \times 10^{-12}$ J/K.

The heat capacity at constant area of the ripplons on the helium surface, $C_2 \equiv (\partial E/\partial T)_A$, can be calculated using the theory of Atkins [6] for the surface entropy. We find for $T < 0.3$ K

$$C_2/A = 2 \times 10^{-5} (T[\mathrm{K}])^{4/3}\ \mathrm{J\,K^{-1}\,m^{-2}}, \tag{5.5}$$

which we can approximate around $T = 0.15$ K by $C_2 \approx 2 \times 10^{-11}$ J/K. The heat capacity of the adsorbed H atoms is negligible in the nondegenerate regime. The heat capacity of the helium surface is so low that the response of the surface temperature T_2 to a change in thermal load can be considered instantaneous for all practical purposes.

On the other hand, the heat capacities of the buffer volume and the helium liquid in the cell are sufficiently large that the temperatures of these objects do not significantly change during the experiment. Since we use a temperature controller to regulate the temperature of the buffer volume, its heat capacity is effectively infinite. We will treat the liquid helium temperature T_{He} and the temperature of the buffer volume T_B as external parameters.

The heat exchange is modeled by an additional set of differential equations, which models the following heat generation and transport phenomena:

- Heating of the helium surface in the cell by energetic molecules formed by recombination, $(P_{R\to 2})$,
- Heating of the bulk gas in the cell by these molecules,$(P_{R\to 3})$,
- Heat transport between the bulk gas and the surface, $(P_{3\leftrightarrow 2})$, and

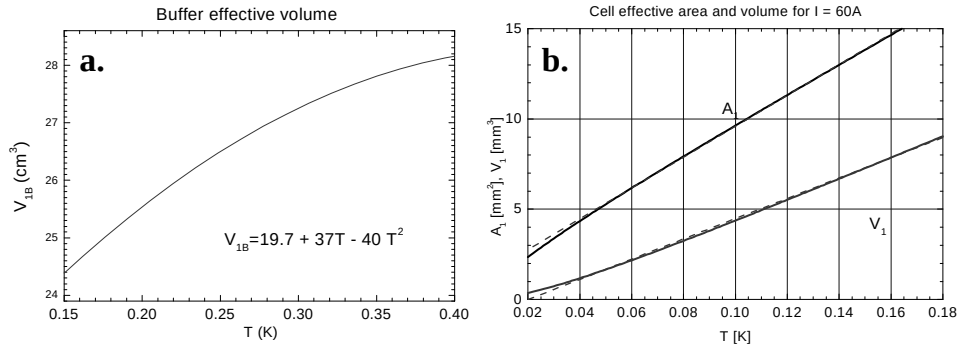

Figure 5.2: (a) Effective volume of the buffer volume versus temperature. (b) Solid lines: Effective volume and surface area of the cell versus temperature. The effective surface area for n-atom processes $A_n(T)$ is equal to $A_1(T/n)$. These curves are valid in the Boltzmann regime. Dashed lines: Linear approximations valid in the temperature range relevant for the experiment. $A_1[\mathrm{mm}^2] \approx 1.05 + 85.4T[\mathrm{K}]$, $V_{1C}[\mathrm{mm}^3] \approx 56.1T[\mathrm{K}] - 1.13$.

- Conversion of surface heat into bulk liquid excitations,$(P_{2\to\mathrm{He}})$.

The heat exchange equations are

$$\frac{d}{dt}T_B = 0, \tag{5.6}$$

$$\frac{d}{dt}T_{\mathrm{He}} = 0, \tag{5.7}$$

$$\frac{d}{dt}T_3 = \frac{1}{C_3}\left(P_{R\to 3} - P_{3\leftrightarrow 2}\right), \tag{5.8}$$

$$\frac{d}{dt}T_2 = \frac{1}{C_2}\left(P_{3\leftrightarrow 2} + P_{R\to 2} - P_{2\to\mathrm{He}}\right). \tag{5.9}$$

The heat exchange equations (5.6 - 5.9) and the rate equations for the atom populations (5.1 - 5.3) are solved simultaneously by a numerical method.

5.2.3 Effective areas and volumes

As a result of the compression of the hydrogen by strong field gradients, the gas density in the cell is very inhomogeneous. In such a strongly inhomogeneous system, the physical volume is not a useful concept, since a reasonable density of atoms only exists in a small part of the system. Atom trapping experiments show an extreme case of this inhomogeneity: the size of the sample is determined by the trapping field and the temperature of the sample, while the physical volume containing the trap is

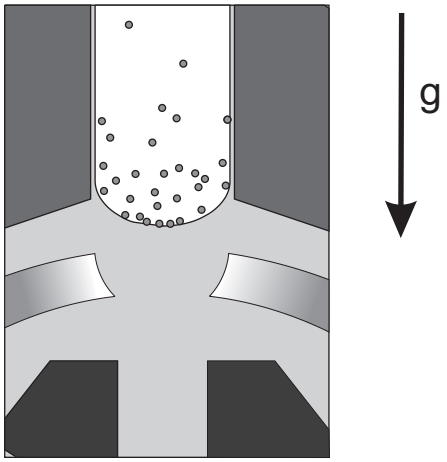

Figure 5.3: Impression of the atmospheric gas distribution in the cell. The magnetic field gradient acts as an 'effective gravity' $g = 10^6$ m/s^2 for the H$\downarrow$ atoms. This effective gravity drives the adsorbed atoms towards the lowest point the curved meniscus. The black shape in the bottom indicates the magnetic field compressor with optical access.

totally irrelevant. The effective volume V_1 the atoms occupy is defined by $N = V_1 n$, where N is the total number of atoms and n is the highest density of atoms, i.e. in our case the density at the field maximum. Remarkably, the effective volume is closely related to the partition function of the gas [15] and a subtle change of effective volume can even be used to compress a trapped gas into the degenerate regime [20, 27].

For an ideal Boltzmann gas of H$\downarrow$, the one-body effective volume is

$$V_1 = \int_V e^{\mu_B (B(\mathbf{x}) - B_0)/k_B T} d^3x, \tag{5.10}$$

where the integral is taken over the volume V that is accessible to the atoms, and B_0 is the highest field occurring in this volume. The effective volumes of the buffer volume and compression cell are shown in figure 5.2.

In our compression cell the magnetic field gradient is practically vertical, so that $B = B(z)$. On the curved surface of the helium meniscus there is therefore a potential gradient, just as in the case of a curved surface in a homogeneous gravity field, see figure 5.3. The one-body effective area A_1 of such a curved surface is defined similarly to the effective volume: $N_2 = A_1 n_2$. In the Boltzmann regime this leads to

$$A_1 = \int_S e^{\mu_B (B(\mathbf{x}) - B_0)/k_B T} d^2x. \tag{5.11}$$

Here B_0 is the maximum field on the surface, and the integral is taken over the curved inner surface S of the container. To calculate the rate of multi-particle interactions in an inhomogeneous system we introduce the m-body effective surface A_m, which is defined so that the rate of the m-body process is $A_m K_m (n_2)^m$, where K_m is the rate constant for the process and n_2 is the maximum density. The effective area is given by

$$A_m = \int_S \left[\frac{n_2(\mathbf{x})}{n_2} \right]^m d^2x. \tag{5.12}$$

In the Boltzmann regime we find that $A_m(T) = A_1(T/m)$. The effective area of the compression cell is shown in figure 5.2 (b).

The effective surface area of the buffer volume A_{1B} is only weakly temperature dependent. One may approximate $A_{1B} \approx A_{2B} \approx 60$ cm^2 at all relevant temperatures, with an error of less than 10%. Due to surface roughness, the effective adsorption area may be slightly larger than this geometrical area.

5.2.4 Local adsorption equilibrium

Since the transfer of energy between the bulk gas and the surface is very inefficient the temperature T_3 of the bulk gas is higher than the temperature T_2 of the adsorbate. For a significant temperature difference, the question rises which of these temperatures determines the density profile of the adsorbate. The answer depends on the migration of the atoms along the surface, and one can distinguish two limiting cases:

case **a.** *Migration through the bulk gas*
If the temperature is high, the average time an atom spends on the surface τ_a is short and the mean free path of a surface adsorbed atom with respect to scattering off ripplons is very short [13], see table 5.1. In this case we may assume that no transport of adsorbed atoms along the surface takes place. In this high temperature limit the bulk gas and the adsorbate are in local adsorption equilibrium, therefore the density profile of adsorbed atoms depends on the *bulk* temperature T_3.

case **b.** *Migration along the helium surface*
In the low-temperature limit the surface residency time is long and the mean free path of an adsorbed atom is large. Therefore, adsorbed atoms are easily transported along the surface and the surface density profile depends only on the ripplon temperature T_2. The surface and the bulk are not in local adsorption equilibrium in this case. The atoms adsorb on an area which is the effective

T(K)	$\tau_{\rm a}$(s)	$\tau_{\rm kin}$(s)	ℓ(m)	$v_{\rm dr}$(m/s)	$d_{\rm dr}$(m)	$d_{\rm dif}$(m)
0.08	6.9×10^{-3}	4.4×10^{-8}	1.9×10^{-6}	2.2×10^{-2}	1.5×10^{-4}	7.3×10^{-4}
0.1	3.5×10^{-4}	2.4×10^{-8}	1.1×10^{-6}	1.2×10^{-2}	4.2×10^{-6}	1.4×10^{-4}
0.2	5.7×10^{-7}	4.2×10^{-9}	2.8×10^{-7}	2.1×10^{-3}	1.2×10^{-9}	3.3×10^{-6}
0.3	4.7×10^{-8}	1.6×10^{-9}	1.3×10^{-7}	8.0×10^{-4}	3.7×10^{-11}	7.1×10^{-7}
0.4	1.1×10^{-8}	8.7×10^{-10}	8.2×10^{-8}	4.4×10^{-4}	4.9×10^{-12}	3.0×10^{-7}

Table 5.1: Time- and length scales for H atom adsorption at various temperatures. $\tau_{\rm a}$ is the mean surface residency time[3], $\tau_{\rm kin}$ the momentum relaxation time [13], ℓ is the mean free path, $v_{\rm dr}$ the drift velocity in a field of 10^6 m/s^2, $d_{\rm dr} = v_{\rm dr}\tau_{\rm a}$ is the distance an atom drifts during τ_a, and $d_{\rm dif} = \ell(\tau_{\rm a}/\tau_{\rm kin})^{1/2}$ the average distance an atom diffuses during the time $\tau_{\rm a}$.

area at T_3, but they distribute themselves over the effective area $A_1(T_2)$, which is usually smaller. Calculations of the surface density profile must include thermally driven migration of atoms along the surface.

In the present compression cell case **a** is prevalent. In general, case **b** is expected to occur when the atoms move a distance of the same order as the system size between the position where they adsorb and where they desorb.

There are basically two mechanisms by which the atoms move along the surface: drift due to the magnetic field gradient, over an average distance $d_{\rm dr}$, and random diffusion due to scattering of ripplons [13], over an average distance $d_{\rm dif}$. These distances are shown in table 5.1.

As shown in figure 5.3, the magnetic field gradient drives the adsorbed atoms towards the centre of the helium meniscus. The atoms experience an acceleration $\mathbf{a} = \mathcal{P}_2(\nabla|\mathbf{B}| \times \mu_{\rm B}/m_H)$. Here, $\mathcal{P}_2$ is the projection operator that projects a vector in the tangential plane, i.e., it removes any component nornal to the surface. The drift due to the acceleration $\mathbf{a}$ is described by the Drude conduction formula [14]. In the presence of an acceleration the atoms will acquire a mean drift velocity $\frac{1}{2}\mathbf{a}\tau_{\rm kin}$, where $\tau_{\rm kin}$ is the mean scattering time. At the edges of the helium meniscus the acceleration due to the field gradient is maximal, $a \approx 10^6$ m/s^2. Table 5.1 lists the values of $\tau_{\rm a}$ and $\tau_{\rm kin}$ for a number of temperatures, and the resulting values for the mean free path ℓ and the mean drift velocity $v_{\rm dr}$. The drift will cause the atoms to desorb at a position which is on average shifted by $d_{\rm dr} = v_{\rm dr}\tau_{\rm a}$ from the location where they adsorbed. It is seen that $d_{\rm dr}$ is much smaller than the size of our system (which is of order 1 mm) at all temperatures.

In the absence of an accelerating field the atoms diffuse randomly. The RMS distance between the position where they adsorb and the position of desorption is $d_{\rm dif} = \ell(\tau_{\rm a}/\tau_{\rm kin})^{1/2}$. In the relevant temperature range ($T > 100$ mK) this diffusion length is also much smaller than the size of the system. Since the transport of particles along the surface does not significantly influence their distribution, the adsorbate will be in local flux equilibrium with the bulk gas everywhere and we calculate the effective area of the cell at the bulk temperature T_3.

5.3 Adsorption equation

The interaction of H atoms with the surface of liquid helium is a rich subject, which has been studied extensively, and reviewed in e.g. Ref. [23]. Hydrogen atoms may interact with the helium surface in various ways: they can reflect specularly from the helium surface (quantum reflection) as was observed by Berkhout *et al.* [18], they may collide inelastically, or they may stick and remain adsorbed for some time. The sticking process was studied for a large range of gas temperatures: from 0.4 K down to 100 μK [3, 26, 24]. At these lowest temperatures the influence of long-range van der Waals forces due to the substrate may strongly affect the sticking process on helium films [25].

Some time after sticking, the atoms will desorb again (recombination processes will be taken into account later). In this section we will obtain a general expression for the mean surface residency time $\tau_{\rm a}$, the mean time between sticking and desorption. This problem has been analyzed by Svistunov *et al.* in Ref. [21] for a one component Bose gas, and we will follow their analysis and extend it to the situation of a two-component Bose gas. The analysis makes use of the fact that in thermal equilibrium the adsorption and desorption fluxes are balanced,

$$\Phi_{2\to 3} = \Phi_{3\to 2}, \tag{5.13}$$

while at the same time the densities of the bulk gas and the adsorbed gas are related through the adsorption isotherm.

In the dilute limit, the sticking process is determined only by the bulk gas [3, 17], the state of the adsorbate hardly influences the sticking process. Only at densities near monolayer coverage ($n_2^{\rm sat} \approx 10^{14}{\rm cm}^{-2}$) will the adsorbate influence the sticking process [19]. The densities relevant in our experiment are an order of magnitude below $n_2^{\rm sat}$, so we may neglect the influence of the adsorbate on the adsorption process. The

number of atoms which stick on a surface area A per second is given by

$$\Phi_{3\to 2} = \frac{1}{4} A s(T_3) \bar{v}(T_3) n_3, \tag{5.14}$$

where $s(T_3)$ is the sticking coefficient, and where $\bar{v}(T_3)$ is the average atomic velocity at T_3, see Eq. (A.2). In the temperature range relevant for our experiment, it was found that $s(T_3) \approx 0.3 T_3[\mathrm{K}]$ [26, 3].

In contrast to the adsorption flux, which can be calculated using the above formulae regardless of the thermal equilibrium between surface and bulk, the desorption flux cannot be calculated straightforwardly when the surface and the bulk gas are out of thermal equilibrium. Following Svistunov *et al.* we calculate the desorption flux in such a case by first considering the relation between bulk and surface density in thermal equilibrium, and generalizing in a later stage to the case of a temperature difference between the bulk gas and the surface.

The adsorption isotherm for H on l-He relates the bulk density to the adsorbate density. It is obtained by equating the chemical potential μ_3 in the bulk gas phase to the chemical potential μ_2 of the adsorbed phase. In our experiments, the bulk gas is far from quantum degeneracy, so that the ideal Boltzmann gas expression

$$\mu_3 = k_\mathrm{B} T \ln(n_3 \Lambda^3) \tag{5.15}$$

may be used, where Λ is the thermal de Broglie wavelength (A.1). Since the adsorbate is close to the degenerate regime, we have to use the expression for the chemical potential of a Bose gas. The chemical potential for an ideal two-dimensional Bose gas is given by

$$\mu_2 = k_\mathrm{B} T \ln[1 - \exp(n_2 \Lambda^2)] - E_\mathrm{a}, \tag{5.16}$$

where E_a is the adsorption energy, $E_\mathrm{a}/k_\mathrm{B} = 1.00(5)\mathrm{K}$ [36]. It is seen that for small values of the degeneracy parameter, the first term reduces to the Boltzmann expression $k_\mathrm{B} T \ln(n_2 \Lambda^2)$. For a weakly interacting non-condensed Bose gas, the interactions can be incorporated as a mean field term of value $2\tilde{U} n_2$, where $\tilde{U}/k_\mathrm{B} \approx 5 \times 10^{-15} \mathrm{K\,cm}^2$ [22, 23] is the calculated effective interaction vertex between adsorbed atoms.

For a Bose condensed two-dimensional sample, the chemical potential is obtained differently. For a pure Bose-Einstein condensate at $T = 0$, the interactions form the only contribution to the chemical potential, and the effective interaction strength is reduced by a factor 2 with respect to the non-condensed phase [28, 29], so that we find

$$\mu_2(T = 0) = \tilde{U} n_2 - E\mathrm{a}. \tag{5.17}$$

It is shown in Ref.[21] that the temperature dependence of μ_2 is negligible in the entire region where the two-dimensional condensate exists ($n_2\Lambda^2 \gtrsim 4$). This leads to the approximate expression for the chemical potential of an interacting Bose gas,

$$\mu_2 = k_{\rm B}T \ln[1 - \exp(n_2\Lambda^2)] - E_{\rm a} + (2 - \Theta)\tilde{U}n_2. \tag{5.18}$$

The first term is very small for large values of the degeneracy parameter, we may therefore leave it in the expression even when $\theta > 0$.

The parameter Θ is a measure of the condensate density; Θ is zero in the absence of a condensate and becomes approximately one when the two-dimensional gas Bose condenses. The exact dependence of Θ on the phase-space density in the transition region is unknown.

Setting $\mu_2 = \mu_3$ leads to the equation for the adsorption isotherm for a one-component gas in thermal equilibrium,

$$n_3\Lambda^3 = \left(1 - e^{-n_2\Lambda^2}\right) \exp\left(\frac{-E_{\rm a} + (2 - \Theta)\tilde{U}n_2}{k_{\rm B}T}\right). \tag{5.19}$$

This relates the bulk density to the surface density at a given temperature $T = T_2 = T_3$. In the limit of low n_2, the adsorption isotherm reduces to the well-known expression for an ideal Boltzmann gas,

$$n_2^{(a,b)} = n_3^{(a,b)}\Lambda e^{E_{\rm a}/k_{\rm B}T}; \;\; (\text{for } n_2\Lambda^2 \ll 1). \tag{5.20}$$

Remarkably, this simple expression is good to within 25 % up to a phase-space density of unity. This is due to a partial cancellation of the interaction term and the quantum-statistical corrections. The simple Boltzmann formula may therefore be used to gain insight into the behavior of the surface density, even close to quantum degeneracy. However, for numerical evaluation of the rate equations we use the full expressions.

In practice, the bulk gas and the adsorbate are never in perfect thermal equilibrium, as the thermal contact between these two systems is poor. We therefore extend the approach to steady state situations with $T_2 \neq T_3$. The surface residency time $\tau_{\rm a}$ is then found by the requirement that in steady state the desorption flux equals the adsorption flux, so that

$$n_2 = \Phi_{3\to 2}\tau_{\rm a}/A. \tag{5.21}$$

The surface residency time only depends on surface temperature and density - not on the state of the bulk gas. We may therefore *calculate* the value of $\tau_{\rm a}$ in thermal equilibrium, and then *use* this value even when $T_2 \neq T_3$. In thermal equilibrium at $T = T_2 = T_3$ we find

$$\tau_{\rm a} = \frac{An_2(n_3, T)}{\Phi_{3\to 2}(n_3, T)}, \tag{5.22}$$

where we have explicitly indicated the fact that n_2 and $\Phi_{3\to 2}$ are functions of n_3 and T. By substitution, we find the expression for $\tau_{\rm a}$,

$$[\tau_{\rm a}(n_2,T_2)]^{-1} = \frac{k_{\rm B}T_2}{2\pi\hbar}s(T_2)\frac{1-\exp(-n_2\Lambda_2^2)}{n_2\Lambda_2^2}\exp\left(\frac{-E_{\rm a}+(2-\Theta)\tilde{U}n_2}{k_{\rm B}T_2}\right). \quad (5.23)$$

Here, Λ_2 is the thermal de Broglie wavelength at T_2. We have explicitly written the surface residency time $\tau_{\rm a}$ as a function of the state of the surface only, as it should not depend on the state of the bulk gas. Note the appearance of the sticking coefficient $s(T_2)$ at the *surface* temperature. The expression simplifies considerably in the Boltzmann regime [3],

$$\tau_{\rm a} = \frac{2\pi\hbar}{k_{\rm B}T_2 s(T_2)}\exp\left(\frac{E_{\rm a}}{k_{\rm B}T_2}\right); \quad (\text{for } n_2\Lambda^2 \ll 1). \quad (5.24)$$

The single component steady state adsorption equation then assumes the form [21]

$$\frac{1}{4}s(T_3)\bar{v}(T_3)n_3 = \frac{k_{\rm B}T_2}{2\pi\hbar}s(T_2)\frac{1-\exp(-n_2\Lambda_2^2)}{\Lambda_2^2}\exp\left(\frac{-E_{\rm a}+(2-\Theta)\tilde{U}n_2}{k_{\rm B}T_2}\right). \quad (5.25)$$

The above equation holds for a gas that is ideally polarized in a single hyperfine state. In realistic gas samples, polarizations of more than 99% of the atoms into the stable b hyperfine state have been achieved, but a small fraction of atoms in the a hyperfine state is always present. These atoms may be insignificant in number, but still contribute significantly to the rate equations due to the fact that their rate constant for recombination with b-state atoms is large. At low density, there is no difference between the adsorption behavior of atoms in the a and b hyperfine states. The large density of b atoms, which is present in experiments aiming at quantum degeneracy, causes an asymmetry in mean-field interactions between atoms in the a and b states. In a non-condensed sample, the repulsive interactions between two atoms in the same hyperfine state are enhanced by a factor 2 due to symmetrization of the wavefunctions. Therefore, in a dense, non-condensed b-polarized gas, an atom in the a state will experience a smaller mean-field interaction potential. Remarkably, in a condensate of b-state atoms, an atom in the a-state will experience the same mean field interaction term as a b-state atom from the condensate.

To correctly track the behavior of the reactive a-state atoms in a high density sample one must generalize the adsorption equations to hold for hyperfine mixtures. This generalization is rather straightforward, one can neglect terms which are of higher order in the density of a-state atoms. The residency times for the two hyperfine

components then follow,

$$
\begin{aligned}
1/\tau_{\rm a}^{(b)} &= \frac{k_{\rm B}T_2}{2\pi\hbar}s(T_2)\frac{1-\exp(-n_2^{(b)}\Lambda_2^2)}{n_2^{(b)}\Lambda_2^2}\exp\left(\frac{-E_{\rm a}+(2-\Theta)\tilde{U}n_2^{(b)}+\tilde{U}n_2^{(a)}}{k_{\rm B}T_2}\right), \\
1/\tau_{\rm a}^{(a)} &= \frac{k_{\rm B}T_2}{2\pi\hbar}s(T_2)\exp\left(\frac{-E_{\rm a}+\tilde{U}n_2^{(b)}}{k_{\rm B}T_2}\right). \qquad (5.26)
\end{aligned}
$$

The steady-state adsorption equations can easily be found from equating the adsorption and desorption fluxes, $n_2^{(a,b)} = \Phi_{3\to2}^{(a,b)}\tau_{\rm a}^{(a,b)}/A$.

The influence of atom loss due to recombination has so far been neglected. Especially in the case a few percent of the atoms is in the a-state, the recombination loss flux may influence the steady-state adsorbate density. Correct steady-state expressions can be straightforwardly obtained by equating the adsorption fluxes with the sum of the desorption flux and the recombination loss flux,

$$\Phi_{3\to2}^{(a,b)} = \Phi_{2\to3}^{(a,b)} + R_C^{(a,b)}. \qquad (5.27)$$

Here R_C stands for the surface recombination loss flux.

5.4 Atom fluxes

In this section we will explicitly derive all atom fluxes appearing in the rate equations (5.1-5.2). As H$\downarrow$ is a relatively simple and very well-studied system, we are able to find quantitative expressions for most atom fluxes.

Dissociator flux:
The dissociator produces a flux of $\Phi_d \approx 2.5\times10^{13}$ atoms per second into the buffer volume, as was determined from measurements of the increase of the buffer volume density just after turning on the dissociator. It was also found that the value of the dissociator flux can vary by as much as a factor 2, probably depending on the amount of solid H_2 available near the position of the discharge. The atoms that come from the dissociator in to the buffer volume are electron spin polarized, as the low-field seeking atoms are blocked out by the magnetic field gradient in between the dissociator and the buffer volume. The nuclear spin remains unpolarized, i.e. half of the atoms are in the a hyperfine state and half are in the b-state.

Injection flux:
The flux of atoms from the buffer volume to the compression cell consists of atoms in the a and b states, described by the fluxes $\Phi_{B\to3}^{(a)}$ and $\Phi_{B\to3}^{(b)}$. These fluxes are

proportional to the number of atom that enter the tube, a Boltzmann factor and an effective Clausing factor.

$$\Phi_{B\to 3}^{(a,b)} = \frac{1}{4} K^* \bar{v}(T_B) A_{\rm inj} \frac{N_B^{(a,b)}}{V_{1B}} e^{-\mu_{\rm B}(B_{\rm max}^{\rm buf} - B_{\rm min}^{\rm inj})/k_{\rm B}T_B}. \tag{5.28}$$

Here, $A_{\rm inj}$ is the 3.14 mm^2 area of the injector tube and $B_{\rm max}^{\rm buf} - B_{\rm min}^{\rm inj}$ is the difference between the field maximum in the buffer volume and the minimum in the injector tube. The effective Clausing factor K^* that appears in this equation differs strongly from the Clausing factor that would appear for the injector tube ($L/r \approx 25$) in a homogeneous field. This can be understood qualitatively by noting that normal Knudsen flow only occurs in the region of the tube where the effect of the field gradient on the motion of the atoms between wall collisions is small. In our experiment, this is the case only in a region with a length of ≈ 2 tube radii. From a full numerical calculation [39] it follows that $K^* \approx 0.5$.

Escape flux:
The reverse flux $\Phi_{3\to B}^{(a,b)}$ can be calculated from the same effusion formula in the reverse direction,

$$\Phi_{3\to B}^{(a,b)} = \frac{1}{4} K^* \bar{v}(T_3) A_{\rm inj} \frac{N_3^{(a,b)}}{V_{1C}} e^{-\mu_{\rm B}(B_{\rm max}^{\rm cel} - B_{\rm min}^{\rm inj})/k_{\rm B}T_3}, \tag{5.29}$$

where $B_{\rm max}^{\rm cel}$ is the maximum field in the compression cell. Note that the reverse flux depends on the cell temperature T_3 while the injector flux depends on the (higher) buffer temperature T_B. This difference in temperatures gives rise to thermal compression of atoms into the compression cell.

Adsorption flux:
The flux of atoms that adsorb to the surface $\Phi_{3\to 2}^{(a,b)}$ is given by (cf. Eq. 5.14)

$$\Phi_{3\to 2}^{(a,b)} = \frac{1}{4} A_1 s(T_3) \bar{v}(T_3) N_3^{(a,b)} / V_{1C}. \tag{5.30}$$

Here, A_1 is the one-body effective surface area of the cell.

Desorption flux:
The desorption fluxes for the different hyperfine states are easily expressed in terms of the surface residency times $\tau_{\rm a}^{(h)}$, as

$$\Phi_{2\to 3}^{(a,b)} = N_2^{(a,b)} / \tau_{\rm a}^{(a,b)}. \tag{5.31}$$

Recombination loss flux:
The recombination losses in the sample are dominated by the region of highest density, in our case the adsorbate in the compression cell, which is effectively orders of

magnitude denser than the bulk gas. The most important recombination processes are surface catalyzed $a + a$, $a + b$ and $b + b + b$ recombination. Since the density of atoms in the a-state is much smaller than that of atoms in the b-state, the influence of $a + a + a$ and $a + a + b$ processes is very small, and even the $a + b + b$ process was found to be negligible with respect to the $a + b$ process [4]. The flux of atoms in the a state lost from the compression cell due to recombination is

$$R_C^{(a)} = A_2 \left[2(n_2^{(a)})^2 K_{aa}^{\rm s} + n_2^{(a)} n_2^{(b)} K_{ab}^{\rm s} \right], \tag{5.32}$$

the recombination flux of b atoms from the compression cell is

$$R_C^{(b)} = A_2 \left[n_2^{(a)} n_2^{(b)} K_{ab}^{\rm s} \right] + A_3 L_{bbb}^{\rm s} (n_2^{(b)})^3. \tag{5.33}$$

Here A_2 is the effective surface area for two-atom processes and $n_2^{(a,b)} = N_2^{(a,b)}/A_1$. The rate constant for an unpolarized gas, $K^{\rm s} = (K_{ab}^{\rm s} + K_{aa}^{\rm s})/2$ has been determined in several experiments [7, 8], see table 5.1 in Ref. [10] for an overview. Most experimental values are consistent with $K^{\rm s} T^{1/2} B^2 = 5.6(5) \times 10^{-8}$ cm^{2}K$^{-1/2}$ T^{2}s^{-1}. To extract the state dependent recombination constants, the fraction $\gamma = K_{aa}^{\rm s}/K_{bb}^{\rm s}$ must be known. In Ref. [10] an overview of a number of measurements of γ is given. There is significant discrepancy between different measurements, they all fall in the range $2 < \gamma < 3.5$. The temperature dependence of γ is not clear. We will assume $\gamma = 2.5$, independent of temperature.

Recently, direct measurements of $K_{ab}^{\rm s}$ by recombination in a gas of b atoms were reported [16, 4] yielding $K_{ab}^{\rm s} T^{1/2} B^2 = 4(1) \times 10^{-8}$ cm^{2}K$^{-1/2}$T^{2}s^{-1}. This rate is consistent with the earlier measurements of $K^{\rm s}$. In our rate equations we use the following values, which are consistent with most experiments,

$$K_{ab}^{\rm s} = 3 \times 10^{-8} \sqrt{T[{\rm K}]}/(B[{\rm T}])^2 {\rm cm}^2{\rm s}^{-1} \tag{5.34}$$

$$K_{aa}^{\rm s} = 2.5 K_{ab}^{\rm s}. \tag{5.35}$$

The recombination loss flux of b atoms includes a third order recombination term $L_{bbb}^{\rm s}(n_2^{(b)})^3$ [9]. The third order surface recombination-loss constant $L_{bbb}^{\rm s}$ was first measured by Hess *et al.* [31], who found $L_{bbb}^{\rm s} = 2.0(6) \times 10^{-24}$ cm^4/s. Sprik *et al.* [1, 2] and, more recently, Safonov *et al.* [16] found similar values. The very recent determination by Safonov *et al.* [4] yielded a value of $8(4) \times 10^{-24}$ cm^4/s, approximately a factor two smaller. In their experiment the effective area for recombination is very small, which may contribute a systematic error on their determination of the rate constant, therefore we chose to use the previously determined value in our rate equations.

In each three-body recombination event, two of the atoms form a molecule, and are therefore lost from the sample. The third atom may also be lost, as it may flip its spin and recombine with another atom from the sample. This way, four atoms may be lost due to a three-body event. The third atom has a probability $\xi \approx 0.8$ [2] of undergoing an electron spin flip to the c state. The c-state atom will recombine quickly with an atom (in the a or b state) from the sample. In practice, $b+b+b$ recombination becomes the dominant process only when the sample is hyperfine polarized into the b-state. We may therefore assume that any atoms that have undergone a spin flip to the c state will recombine with a b-state atom from the sample. Therefore, only atoms in the b state are destroyed due to the three-body process. In each event, $(2+2\xi)$ atoms are destroyed. The loss-rate constant $L^{\rm s}_{bbb}$ is therefore a factor $(2+2\xi)$ larger than the event rate constant.

When the sample becomes quantum degenerate, both the three-body effective area and the effective recombination constant $L^{\rm s}_{bbb}$ change due to quantum correlations. These effects have not been incorporated into our model of the compression cell, as too little is known about the behavior of the gas in the transition region.

Recombination loss in the buffer volume:
The only important recombination processes in the buffer volume are surface catalyzed $a+a$ and $a+b$ recombination. The loss-flux of atoms due to these processes is

$$\begin{aligned} R_B^{(b)} &= \frac{A_{2B}}{V_{1B}^2}\Lambda^2 e^{2E_{\rm a}/k_{\rm B}T_B} K_{ab} N_B^{(a)} N_B^{(b)}, \\ R_B^{(a)} &= \frac{A_{2B}}{V_{1B}^2}\Lambda^2 e^{2E_{\rm a}/k_{\rm B}T_B} \left(K_{ab} N_B^{(a)} N_B^{(b)} + 2K_{aa} (N_B^{(a)})^2 \right), \end{aligned} \tag{5.36}$$

where Λ is the thermal de Broglie wavelength at T_B.

Nuclear spin relaxation:
A final term concerns relaxation of the nuclear spins. In a dense gas, nuclear spin relaxation can be the "bottleneck" which determines the life-time of the gas sample [5]. In the present geometry, the main contribution to nuclear spin relaxation is relaxation due to magnetic impurities in the cell and buffer volume walls. These impurities cause the nuclear spins of the atoms to depolarize, thereby converting atoms in the b-state to the a-state and vice versa. The relaxation is modeled by an effective bulk interconversion rate $G^{\rm eff}$ for the a and b hyperfine states, so that the number of b atoms in the compression cell that relaxes to the a-state per second is $G^{\rm eff}_{\rm cell} N_3^{(b)}$. In our numerical model, the nuclear spin relaxation process enters as an effective bulk rate, as this is more convenient. However, the actual process is dominated by the adsorbed atoms. This leads to a strong (exponential) contribution

to the temperature dependence of the rate constants.

The nuclear relaxation rate constants $G^{\text{eff}}_{\text{cell,buff}}$ depend on the purity of the material walls. This cannot be determined *a priori*, the relaxation constants have to be obtained from hydrogen decay measurements. For the buffer volume a straightforward measurement is possible by over-filling the compression cell with liquid helium. This measurement is discussed in section 5.6.1, and yields $(G^{\text{eff}}_{\text{buff}})^{-1} \approx 14000$ s at $T = 250$ mK. The rate constant for the compression cell can not be obtained directly, since it is impossible to completely isolate the compression cell. This rate constant therefore remains a free parameter, which will be determined by a fit to measured data in section 5.6.2.

5.5 Heat fluxes in the compression cell

Almost all equations in the above section depend strongly on temperature, and the model can only have descriptive value if we have values for the temperatures of the different subsystems. The thermal section of our model of the cell predicts these temperatures based on the thermal deposition and transport processes than happen in the cell. It reflects the deposition of recombination heat, its transport between the surface and the bulk gas and its conversion into phonons in the liquid helium.

Recombination heating: The recombination events on the surface create excited molecules, these molecules then lose their energy in collisions with the helium surface and the hydrogen gas atoms. Only a tiny fraction ($f_{\text{dir}} < 0.01$ [32, 33]) of the binding energy is deposited directly at the place where the recombination event occurs. In section 5.7.1 it will be shown that a realistic estimate is $f_{\text{dir}} = 0.006$. It was determined by Vasilyev *et al.* that it takes approximately 150 wall collisions, and possibly slightly more, for a molecule to dissipate half its energy [32]. Since the cell walls are not very smooth, the molecule is scattered diffusively in each collision. A certain fraction of the molecules will return one or more times to the meniscus, and release some energy there, in addition to the energy released in the recombination event. With the assumption that a constant fraction of the molecule's internal energy is transferred to the helium film in each collision, one can calculate the heat-load these returning molecules deposit on the helium surface. From a Monte-Carlo type calculation it follows that for our cell geometry the scattered molecules deposit a fraction $f_{\text{ret}} = 0.032$ of their recombination heat on the area of the meniscus, $A_{\text{men}} = 11.6$ mm^2. This leads to a heat-load on the meniscus of

$$P_{R\to 2} = (f_{\text{ret}} + f_{\text{dir}})\frac{1}{2} D_{H_2}(R_C^{(a)} + R_C^{(b)}), \tag{5.37}$$

where D_{H_2} is the dissociation energy of the hydrogen molecule (See Eq. A.3). It should be noted that there is some uncertainty in $f_{\rm ret}$. The numerical collision assumed a constant fraction of the molecule's energy is transferred in each wall collision, this is probably an oversimplification. In addition, as discussed in [32], the number of wall collisions the molecule needs to release half its energy could be larger than the quoted 150. However, the numerical calculation is only sensitive to the square root of this number.

Ripplon to phonon conversion: As discussed in section 4.5 of this thesis, the adsorbed atoms are thermally coupled to the ripplons on the helium surface, which are very weakly coupled to the phonons in the bulk liquid. We use the following approximation to the expression derived by Reynolds, Shlyapnikov and Setija to calculate the power converted to phonons:

$$P_{2\rightarrow He} = \kappa_{rp} A_{\rm men} (T_2^{20/3} - T_{\rm He}^{20/3}). \tag{5.38}$$

Here $\kappa_{rp} = 8.4 \times 10^3\,{\rm W\,m^{-2}K^{-20/3}}$ is the ripplon phonon coupling constant [12]. The measurements presented in chapter 4 quantitatively support this ripplon-phonon coupling theory. The temperature $T_{\rm He}$ of the liquid helium is below 85 mK in the experiments aiming at high phase space density. At typical power fluxes that occur in the experiment the surface temperature $T_2 > 0.1$ K. Due to the 20/3 power law the converted power becomes independent of $T_{\rm He}$. In the thermal model of the compression cell we use $T_{\rm He} = 0.07$ K, which is the base temperature of the present apparatus. Heat conductance along the surface, which is investigated in section 5.7.1, does not contribute to the cooling of the meniscus, because the most important heat-load, that due to the scattered molecules, is distributed rather homogeneously over the surface area. Therefore, a term describing this contribution is not included in Eq. 5.9.

Bulk gas temperature:
The bulk gas in the compression cell is heated by the excited molecules that form in recombination processes. Such molecules traverse the cell approximately 150 times, and during their flight they may collide with atoms from the bulk gas and transfer some of their kinetic energy. These collisions will be rather rare, as at $n_3 \approx 10^{15}$ atoms/cm^3 the bulk gas is relatively dilute, and the H-H_2 scattering cross-section is small (see chapter 4). Only a small fraction $f_{\rm bulk}$ of the recombination heat will be dissipated in the gas. From the measurements presented in section 4.5 we estimate $f_{\rm bulk} \approx 1.3 \times 10^{-16} N_3$, which is about 3×10^{-3} under typical conditions. This heat is carried away by thermalization of the bulk gas atoms with the helium surface.

The thermal contact between the hydrogen bulk gas and the helium surface is

rather poor. Heat transfer is dominated by sticking of atoms on the helium surface, which is proportional to the number of atoms that collide with the surface. The accommodation coefficient α describes the efficiency of the energy transfer. The net heat flux at small temperature difference $T_3 - T_2$ is

$$P_{3\to 2} = \alpha\,(T_3 - T_2)\frac{1}{4}A_1(T_3)\frac{N_3}{V_{1C}}\bar{v}(T_3). \tag{5.39}$$

The thermal accommodation coefficient α was measured in the relevant temperature range by a number of groups, (See e.g., [3, 11]), yielding $\alpha \approx 0.5T_3$[K]. The temperature of the bulk gas is then determined by the requirement that the heat-load dissipated by molecules in the bulk gas equals the heat transfer of the bulk gas to the surface, $P_{R\to 3} = P_{3\to 2}$. Since the thermal contact is so poor, even the small fraction $f_{\rm bulk}$ of the recombination heat-load gives rise to a 10-20% temperature rise of the bulk gas over the surface temperature.

5.6 Model of the gas sample

The atom flux and heat exchange equations (5.1 -5.3 and 5.6 - 5.9), together with the expressions for the fluxes in the preceding section, form a numerical model of the gas sample in the apparatus. Now that we have constructed this model, we can use it to simulate the behavior of the gas. From this simulation we can obtain predictions of important variables such as the maximum achievable phase space density and the lifetime of the sample.

In principle, if all constants that appear in the equations were known exactly, and all physical processes were adequately included, one should obtain a precise prediction for the behavior of the sample. In practice, as discussed in the preceding section, some constants are only approximately known, or suffer from large experimental uncertainties. In addition, it is important to observe that this model was constructed *a posteriori*, using data from the experiment itself. Experimental data was used to obtain the estimate for the amount of bulk gas heating, and to confirm the theory of ripplon-phonon coupling for heat transport through the helium surface.

Another source of uncertainty in any experiment with H$\downarrow$ is the magnetic purity of the apparatus, on which the nuclear spin relaxation constants $G^{\rm eff}_{\rm cell,buf}$ depend. A determination of $G^{\rm eff}_{\rm buf}$, using a hydrogen sample, is given in section 5.6.1, the nuclear spin relaxation rate constant $G^{\rm eff}_{\rm cell}$ remains the only adjustable parameter in the model.

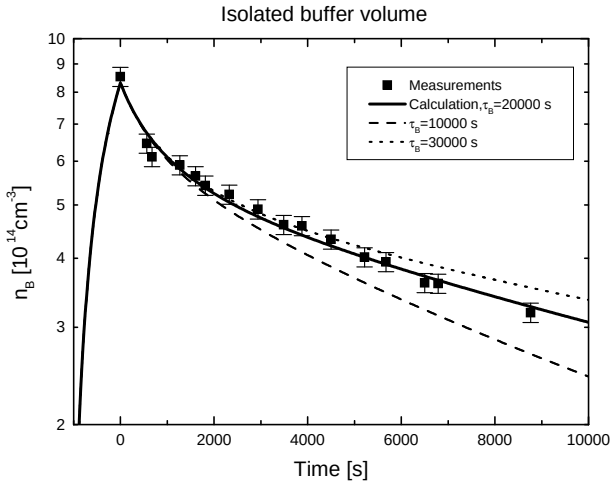

Figure 5.4: Density of atoms in the isolated buffer volume as a function of time. The compression cell was overfilled with helium for this measurement. The dissociator was turned off at $t = 0$. Points: Experimental data, $T_B = 0.25$ K. Solid line: Model calculation, with nuclear spin relaxation time $\tau_B = 20000$ s. Dashed/dotted lines: Calculations with $\tau_B = 10000, 30000$ s.

5.6.1 The isolated buffer volume, nuclear spin relaxation

In one experiment we over-filled the compression cell with liquid helium, so that the gas in the buffer volume could be studied without communication with the cell. We studied the decay of the gas in this simple system to obtain the time constant for nuclear relaxation τ_B. By fitting model decay curves to the experimental ones (as shown in Fig. 5.4 we find $\tau_B = 2.0(5) \times 10^4$ s at $T_B = 0.25$ K and $\tau_B = 8(1) \times 10^3$ s at $T_B = 0.20$ K. This agrees well with the $T^{1/2} e^{E_a/T}$ behavior one would expect for an essentially temperature independent surface induced relaxation process. The nuclear spin relaxation time in the buffer volume is well described by

$$\tau_B = 6 \times 10^5 \,\mathrm{s} \times (T_B[\mathrm{K}])^{-1/2} e^{-1.01/(T_B[\mathrm{K}])}. \tag{5.40}$$

5.6.2 Time evolution of the gas sample

By simultaneously solving the population and heat exchange equations for the compression cell and the buffer volume we obtain the time evolution of all thermodynamical variables in the experiment, which we can compare to the experimental data. A typical time series is shown in figures 5.5 and 5.6. In this experiment, the dissociator

was run for one hour, after which it was turned off and the buffer volume was temperature stabilized to 293 mK. The helium in the compression cell was cooled to obtain the lowest possible temperature under these circumstances, $T_{\mathrm{He}} \approx 85$ mK. In figure 5.5 we see the density of the gas in the buffer volume, which contains most of the atoms, together with the temperatures in the compression cell. Figure 5.6 shows the evolution of the bulk gas and adsorbate densities in the compression cell, as well as the calculated evolution of the nuclear spin polarization (a-state fraction). The nuclear spin polarization was not measured in this experiment. Note that the bulk gas and adsorbate densities are related through the adsorption equation, see section 5.3. The experimental surface temperatures in figure 5.5 were calculated from the measured densities by inverting the adsorption equation. The measured and calculated values are seen to agree qualitatively and quantitatively (note the systematic uncertainty in the lower panel of figure 5.6).

It is seen that initially the number of atoms in the buffer volume decreases slowly, while the temperatures in the compression cell are much above the liquid helium temperature. After approximately 1000 seconds the temperatures in the compression cell decrease faster, and the characteristic time of the decay of the sample in the buffer volume becomes shorter. The explanation of this behavior is found in the overheating of the compression cell, which leads to a steady state with strong negative feedback. At high buffer density, a large flux $\Phi_{B\to 3}$ of atoms is injected into the compression cell, which gives rise to a high recombination flux, and therefore a high temperature in the compression cell. This high temperature allows atoms to escape over the potential barrier, back into the buffer volume. The return flux $\Phi_{3\to B}$ will reduce the net flux into the cell.

If the cell is magnetically pure, the returning atoms will be substantially better hyperfine-polarized than the injected gas, as the a atoms recombine preferentially in the dense adsorbate. In the absence of impurity relaxation, the return flux from the cell will lead to improved polarization of the gas in the buffer volume, and the lifetime of the sample will be very long. On the other hand, in the presence of magnetic impurities, the returning flux will not be hyperfine-polarized, and the sample will decay faster.

Therefore, the long-time behavior of the densities depends strongly on the magnetic purity of the compression cell, i.e., on the nuclear spin relaxation rate constant $G_{\mathrm{cell}}^{\mathrm{eff}}$. This parameter was adjusted to reproduce the observed long-timescale behavior of the buffer density. The curves shown were calculated using $G_{\mathrm{cell}}^{\mathrm{eff}} = 0.05\ \mathrm{s}^{-1}$. As the nuclear relaxation rate constant is a free parameter, it is possible that the effect of errors in other quantities has been absorbed in the fit value. The predicted evolution

of the sample agrees well with the observations, which indicates that the behavior of the hydrogen sample in our apparatus is well-understood.

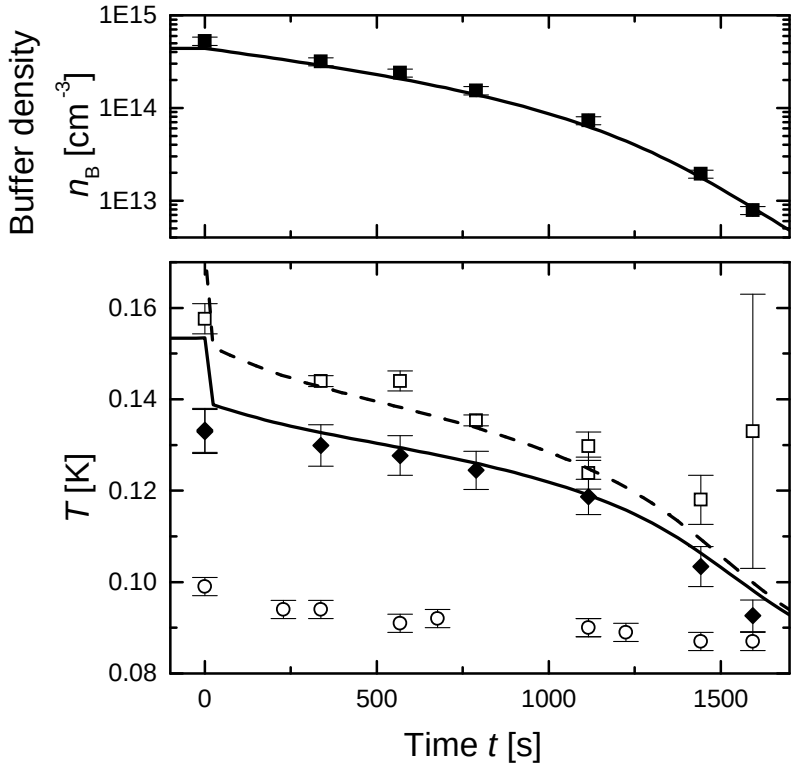

Figure 5.5: Time evolution of cell temperatures and buffer density. Upper panel: the density of atoms in the buffer. Line: Model prediction, squares: Experimental data. Lower panel: Temperatures in the compression cell. Open squares: Bulk gas temperature T_3, closed diamonds: surface temperature T_2. Open circles: Helium temperature T_{He}. At $t = 0$ the dissociator is turned off and the buffer volume is cooled, which causes a jump in all temperatures.

5.6.3 The sample in the compression cell

The time-scales on which the sample in the compression cell reaches a steady state is of the order of milliseconds, much faster than the evolution of the buffer density. In the rate equations it is therefore possible to separate the dynamics, and treat the buffer as a steady source of polarized H atoms. This offers an important simplification of the presentation of the model predictions. Only two independent variables suffice

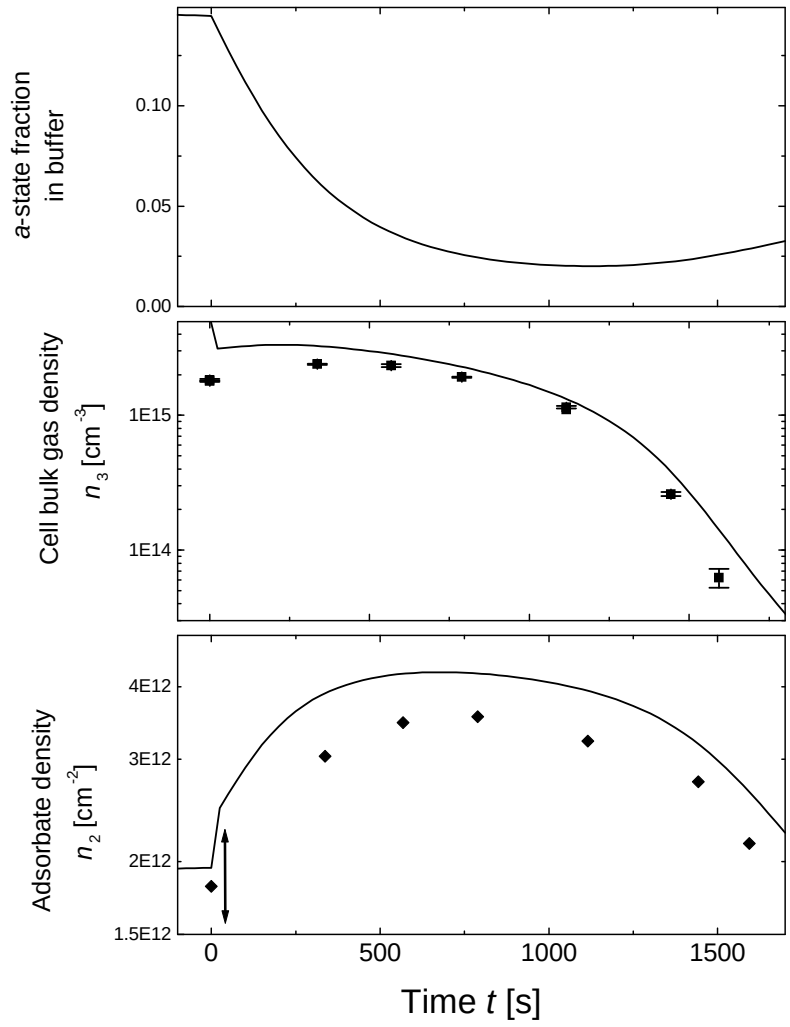

Figure 5.6: Time evolution of bulk gas and adsorbate density. Lines: Model prediction, symbols: Experiment. Upper panel: Predicted fraction f_a of atoms in the a hyperfine state in the buffer volume. This quantity was not measured directly. Middle panel: Bulk gas density n_3 in the compression cell. Lower panel: Adsorbate density n_2. The measurements of n_2 suffer from a systematic uncertainty, indicated by the arrow. The statistical uncertainty is much smaller, of the order of the symbol size.

to calculate the state of the sample in the compression cell: The flux of atoms that is injected from the buffer volume, $\Phi_{B\to 3}$, and the degree of hyperfine polarization

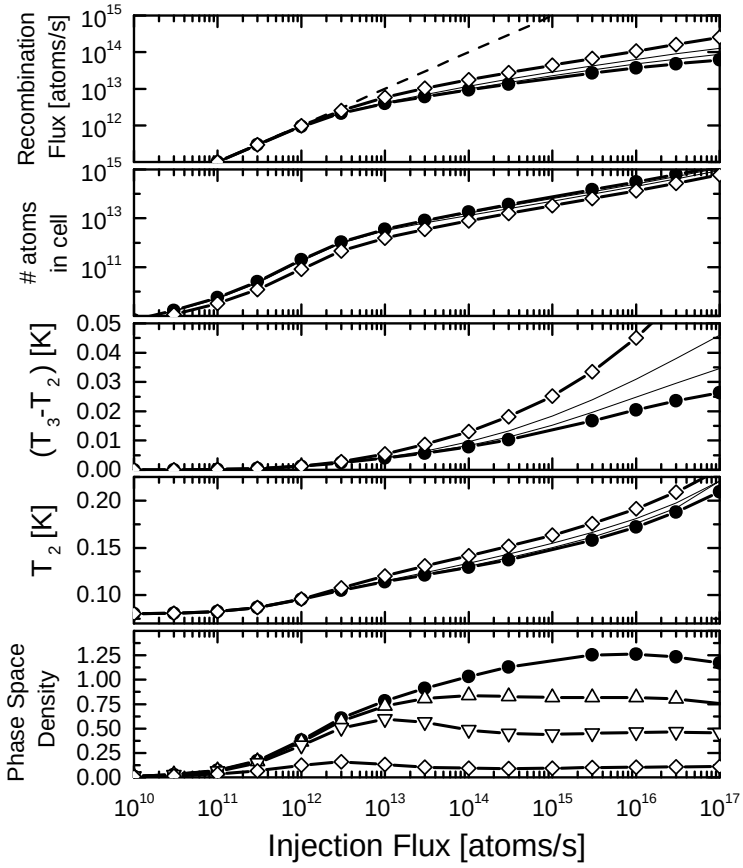

Figure 5.7: Calculated steady-state behavior of the present compression cell. The graph shows various thermodynamic quantities, calculated as a function of injection flux $\Phi_{B\to 3}$. Black dots: injection of pure b-state atoms, $\triangle$: injection of 3% a-state atoms, ∇: 10 % a, $\diamondsuit$: 50 % a. The straight line in the upper panel corresponds to a recombination flux equal to the injection flux. The experimentally accessible range for the injection flux is $10^{12}/\mathrm{s} \lesssim \Phi_{B\to 3} \lesssim 10^{16}/\mathrm{s}$.

(fraction f_a of a-state atoms) of the injected atoms. The injection flux is not only a convenient independent variable in our population rate equations, it is also a variable which can be controlled in an experiment, by changing the temperature of the buffer volume. The a-state fraction f_a cannot be controlled so easily.

In figure 5.7, predicted thermodynamic variables in the compression cell are shown as a function of the injection flux. A number of values for the fraction f_a has been

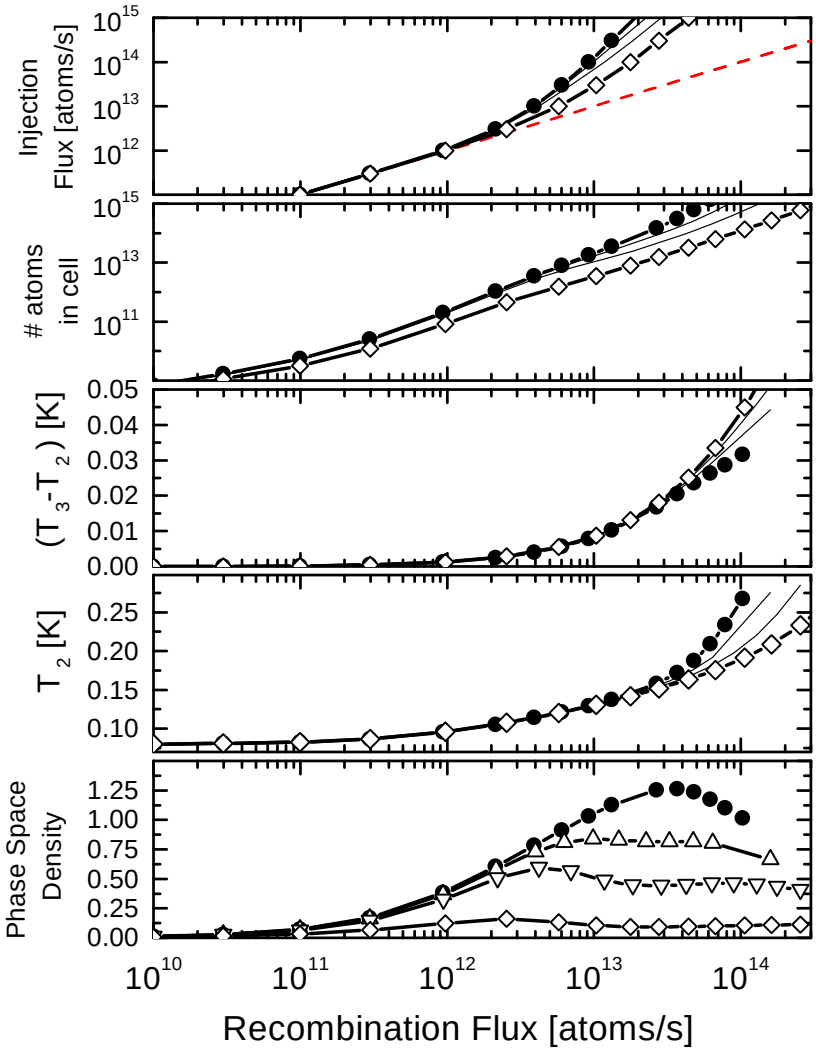

Figure 5.8: Predicted thermodynamic variables of the gas in the compression cell as a function of the recombination flux R_C. Black dots: injection of pure b-state atoms, $\triangle$: injection of 3% a-state atoms, ∇: 10 % a, $\diamondsuit$: 50 % a. The straight line in the upper panel corresponds to a recombination flux equal to the injection flux.

plotted. In the experiment f_a is between zero and 3%. Obviously, the highest density occurs when all the atoms that are injected into the cell are in the stable b hyperfine state. It is seen that at an injection flux of 10^{13} atoms/s the recombination flux

deviates from the injection flux, i.e. a fraction of the atoms that are injected into the cell leave without recombining.

This is an illustration of the negative feed-back due to overheating: Recombination leads to heating of the helium surface, mainly because excited molecules collide with the surface. As the atoms in the cell acquire more thermal energy, their probability to escape over the potential barrier and return to the buffer is increased. Injecting more atoms will not increase the density proportionally, instead the temperature will increase so that most of the extra injection flux will be returned to the buffer volume. This increase of the temperature has an important consequence for the phase-space density, since $n_2\Lambda^2 \propto n_2/T$. In the overheated regime, the density increases only very slowly with injection flux, while the temperature rises quickly. This leads to a stagnation, and even a decrease of the phase-space density at high injection flux.

The experimentally accessible range of the injection flux is between 10^{12} and 10^{15} atoms/s, and it is seen that the phase space density has a maximum value of $n_2\Lambda^2 \approx 1.25$ in this range. Increasing the injection flux does not improve this value. The results shown use the value for the nuclear spin relaxation rate constant $G_{\rm cell}^{\rm eff}$ as determined in section 5.6.2. The results depend only very weakly on $G_{\rm cell}^{\rm eff}$, as the negative feedback reduces the sensitivity to any parameter.

Although the injection flux can easily be controlled in an experiment, it cannot be measured very accurately. If one measures the decay of the number of atoms in the buffer volume, one finds the total recombination loss flux, which can differ strongly from the injection flux as argued above. It is therefore useful to represent the same data as a function of the recombination flux, as is done in figure 5.8. In Fig. 5.9 we show the same predictions on a different scale, together with experimental data. The measured and predicted temperatures T_2 and T_3 are seen to agree. The fraction $f_{\rm bulk}$ in our model is in fact an adjustable parameter, which is determined from a similar graph in section 4.5. The predicted surface temperature does not depend on any free parameters, and the agreement with the measured points is satisfactory.

The design of the present compression cell was optimized for detection of the fluorescence of the adsorbed gas. To facilitate LIF spectroscopy the sample area is relatively large, which has the additional advantage that heat fluxes and effective areas can be accurately determined. The disadvantage is that magnetic compression and heat-load handling are not optimal. The maximum attainable phase space density could not be accurately determined on the basis of *a priori* calculations. The simulations presented in figures 5.7 and 5.8 show that in the present compression cell the phase space density does not exceed 1.25, which is approximately a factor three short of the Kosterlitz-Thouless transition. These simulations rely partially on

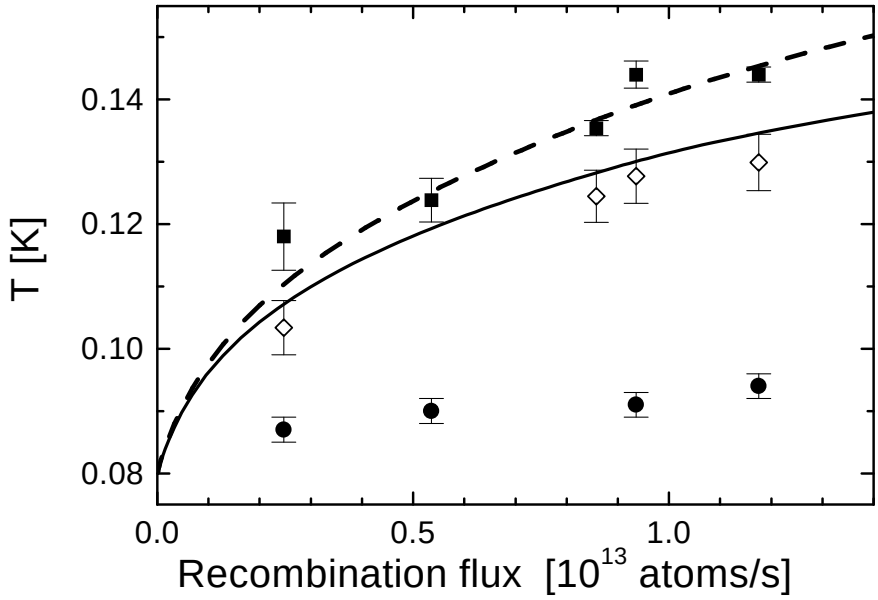

Figure 5.9: The temperatures T_3 of the bulk gas (squares) and the adsorbate (circles) as a function of recombination rate. Solid line: prediction of T_2 from the population dynamics model. Dashed line: prediction of T_3. The calculated curves are insensitive to the degree of polarization of the nuclear spins.

insights and data that have become available in the experiment itself, and in recent related experiments. The model of the present compression cell is very successful in describing the behavior of the present apparatus and its limitations, and it is therefore an excellent tool for the design of a new apparatus.

5.7 Considerations for the design of an improved apparatus

The analysis in section 5.6.3 shows that the main limitation on the phase space density in the present compression cell results from energy dissipation by vibrationally excited molecules. We can therefore expect an important improvement in the maximum phase space density if we reduce the probability for molecules to return to the meniscus. This can be accomplished by allowing more room for the molecules to dissipate their energy, and by reducing the effective area for recombination. In this

way, the probability for an excited molecule to return to the surface can be made negligible ($< 10^{-5}$). In this case a different heating mechanism will become dominant, namely, the direct release of energy in the recombination event. The fraction $f_{\rm dir}$ of the recombination energy released at the position of the event is below 1%, but above approximately 0.3%, as shown in section 5.7.2. This has an important consequence for the possibility to attain quantum degeneracy: in a system where all the directly dissipated heat load has to pass through the ripplon-phonon barrier, there is a *minimum* temperature for reaching quantum degeneracy. We will use the phase space density corresponding to the Kosterlitz-Thouless transition [21] as our criterion for reaching quantum degeneracy,

$$n_2 \Lambda^2 = 4. \tag{5.41}$$

The recombination loss flux density (loss flux per unit area) is $\mathcal{R} = n_2^3 L^{\rm s}_{bbb}$, and we find for the recombination heat load density $\mathcal{P} = f_{\rm dir} D_{\rm H_2} \mathcal{R}/2$. From the ripplon-phonon coupling theory [12] we then find the temperature, $T_2 = (\mathcal{P}/K_{rp})^{3/20}$, assuming the liquid substrate is much colder than the surface. From these relations we easily find the surface temperature as a function of the density,

$$T_2 = \left(\frac{L^{rms}_{\rm bbb} f_{\rm dir} D_{\rm H_2}}{2 K_{rp}} \right)^{3/20} n_2^{9/20}. \tag{5.42}$$

In figure 5.10, we plot the conditions (5.41) and (5.42), in a n_2 versus T_2 graph. The figure shows that the inequality (5.41) can only be fulfilled for $T_2 > T_2^*$, with

$$\begin{aligned} T_2^* &= \left(\frac{2 m_{\rm H} k_{\rm B}}{\pi \hbar^2} \right)^{9/11} \left(\frac{L^{\rm s}_{bbb} f_{\rm dir} D_{\rm H_2}}{2 K_{rp}} \right)^{3/11} \\ &\approx f_{\rm dir}^{3/11} \times 1.08\,{\rm K}. \end{aligned} \tag{5.43}$$

For the estimated value $f_{\rm dir} = 0.006$ we find $T_2^* = 0.268$ K, and this value depends only very weakly on the exact value of $f_{\rm dir}$. This high temperature introduces many experimental complications, for example magnetic compression will be much less efficient at high temperature and the bulk gas density will be extremely high. Therefore, to enter the degenerate regime it is essential that part of the recombination energy be carried away along the surface, by ripplons.

5.7.1 Ripplon cooling

The ripplons moving along the surface of the helium transport energy, and can therefore contribute to the cooling of the spot. The question is: how much cooling power

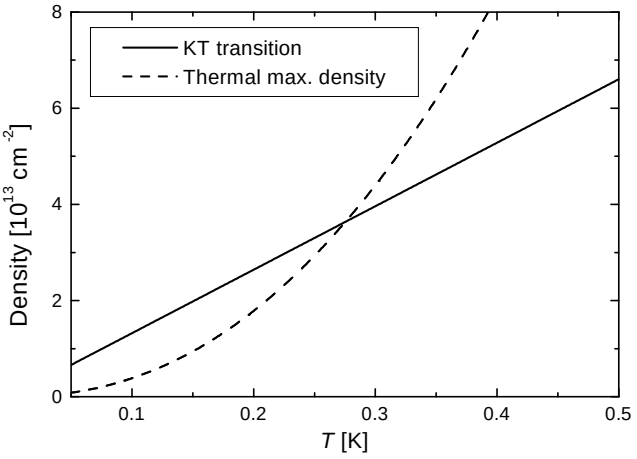

Figure 5.10: Solid line: two-dimensional density of atoms at the KT phase transition as a function of the surface temperature. Dashed line: Maximum density of the adsorbate where ripplon-phonon coupling can remove the dissipated recombination energy in the homogeneous case. The helium liquid temperature is assumed to be much lower than the surface temperature, and we have assumed $f_{\rm dir} = 0.006$. The experimentally accessible region is the region under the dashed line.

do they contribute? At the low temperatures under consideration, ripplons are long-lived excitations with a wave-like dispersion relation. This dispersion relation ensures that the energy flux is proportional to the momentum density. Collisions between ripplons do not alter the local momentum density and therefore do not interfere with the transport of heat along the surface. Hence, in principle, the thermal conductivity of the ripplon gas on the surface of pure superfluid helium should be infinite. Energy carried away by ripplons should travel without diffusion, until it reflects from a boundary or is converted to phonons.

However, if ^{3}He atoms are present, they will scatter the ripplons and reduce the thermal conductivity. The same is true for H atoms. Moreover, for helium films, interactions with the substrate cause additional thermal resistivity.

The thermal conductivity of helium films was measured by Mantz, Edwards and Nayak [34], for helium films on smooth surfaces, with different concentrations of ^{3}He impurities. No measurements of the heat conductivity of the ripplons on bulk helium has been made (this is experimentally difficult). It was found that $K_{rr}^{\rm eff} \approx 40$ nW/K for 100 Å ^{4}He films in the relevant temperature regime. For bulk helium with a low amount of ^{3}He, the ripplon conductivity was extrapolated from the film data, and

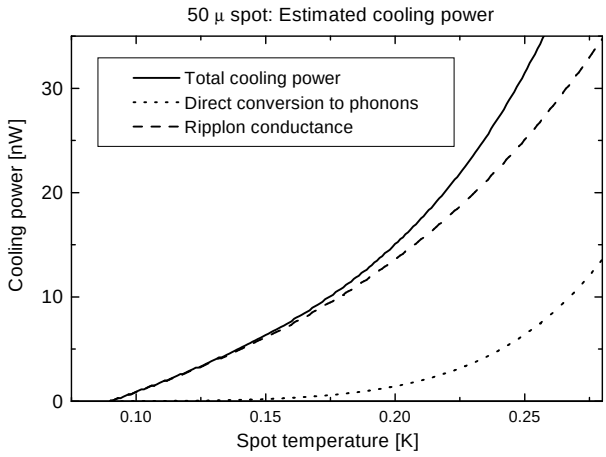

Figure 5.11: Calculated cooling power for a spot with radius 50μ, as a function of spot temperature. A value of $K_{rr}^{\rm eff} = 40nW/K$ has been assumed for the ripplon conductivity. It is seen that direct conversion to phonons (i.e., ripplon-phonon conversion on the spot) is very inefficient with respect to ripplon conduction. The bulk helium temperature is 0.09 K.

found to be inversely proportional to ^{3}He surface density:

$$K_{rr}^{eff} = 4.5\,\mathrm{kWK}^{-1}/(n_{3s}[\mathrm{cm}^{-2}]), \tag{5.44}$$

where n_3s is the surface density of ^{3}He atoms. For the case of the purified ^{4}He in our cell, n_{3s} is probably of order 10^{10} cm^{-2} or smaller, hence the ripplon heat conductivity on bulk helium should be better than ≈ 500 nW/K.

In case of a finite conductivity, the power flux on the surface is related to the temperature gradient,

$$\vec{\mathcal{P}}(\vec{r}) = -K_{rr}^{\rm eff}\nabla T(\vec{r}), \tag{5.45}$$

where $K_{rr}^{\rm eff}$ is the effective heat conductivity due to impurities and surface effects.

The ripplon-phonon conversion process acts like a sink for the power flux,

$$\nabla \cdot \vec{\mathcal{P}} = -K_{rp}(T^{20/3} - T_{\rm He}^{20/3}). \tag{5.46}$$

In the presence of large amounts of ^{3}He other processes, such as 'evaporation' of ^{3}He into the helium liquid, may also contribute to the heat transport. The above equations can be used to estimate the efficiency of ripplon heat transport, and the effective area over which the recombination heat is smeared out before it is converted to phonons. For a recombination spot with radius of 50μ, and a rather pessimistic estimate of the

effective conductivity, $K_{rr}^{\text{eff}} = 40$ nW/K, the solution for the cooling power is shown in figure 5.11. In addition, the cooling power due to "direct" conversion, i.e. ripplon-phonon conversion on the area of the spot, is shown. This term is seen to be much smaller than the ripplon conductance term in the low temperature regime. This curve corresponds to a fixed effective area for recombination, with a homogeneous temperature.

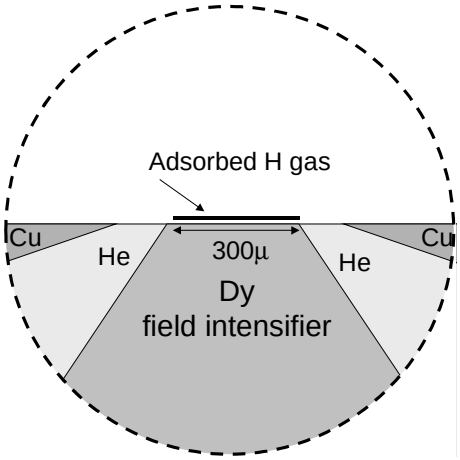

Figure 5.12: Schematic drawing of the Turku Dysprosium compression cell [16]. The radius of the high density spot is 150μ.

5.7.2 Estimation of f_{dir}

The fraction of the recombination energy that is dissipated at the position of the recombination event, f_{dir}, is an important unknown parameter in our experiments. An upper bound on f_{dir} has been established for the case of $a + b$ recombination in experiments in Harvard [38], where it was found that $f_{\text{dir}} < 0.04$, and in Turku [32], where a lower upper bound was found, $f_{\text{dir}} < 0.02$, with a most probable value of 0.01. In our experiment, the most important recombination process is three-body $b + b + b$ recombination, for which the value of f_{dir} may be different. An upper limit, $f_{\text{dir}} < 0.014$, was found for three-body recombination in the "cold-spot" experiment in Kyoto [33, 37]. In this experiment a large heat-load that was not related to recombination was present, and an independent estimate of f_{dir} for three-body recombination would be useful.

An approximate lower bound can be obtained from the data taken in a magnetic compression experiment performed by the Turku group [16], using our measurement

of the ripplon-phonon coupling. The geometry of the experiment is shown in figure 5.12. An adsorbed gas of H$\downarrow$ was compressed to the edge of quantum degeneracy ($n_2\Lambda^2 \approx 2$) on a high density spot. This spot was in fact the helium-coated tip of a Dysprosium (Dy) needle, which locally intensifies the magnetic field. The tip of the needle was circular, with radius $r_{\rm spot} = 150\mu$, and it was surrounded by a ring of bulk liquid helium and copper heat conductors. The geometry in this experiment was such that the probability for an excited molecule to return to the needle tip was negligible, i.e., one can safely neglect the heat flux deposited on the spot by molecules. In the relevant temperature regime ($T_{\rm spot} \approx 0.2$K), the Kapitza resistance between the liquid He film and the metal is expected to be even larger than the ripplon-phonon barrier, so the dominant cooling channel is expected to be heat conduction by ripplons towards the liquid helium pool. We obtain an estimated lower bound to the power carried away by the ripplons by making the following assumptions:

- The ripplons on the liquid helium pool are in thermal equilibrium with those on the high-density spot. This is realistic as the ripplon heat conductivity on the bulk helium is expected to be large.
- The ripplon conductivity on the helium films on the copper heat conductors is zero, i.e., no heat is transported there. This is not a realistic assumption, but allows us to obtain a lower bound. In fact the heat conductivity here will be much lower than on the bulk helium, but probably not negligible.

Using these assumptions, we find that a lower limit for the cooling power of this system is

$$P_{\rm min} = A_{\rm pool} K_{rp} T^{20/3}. \tag{5.47}$$

In the experiment, the recombination power was measured as a function of the spot temperature. For the conditions described in [16], $T_{\rm spot} = 225(7)$ mK, $n_2 = 2.2(5) \times 10^{13}$ cm^{-2}, we find, using the recombination constant K_{bbb} determined in the same paper, that the total recombination power $P_{\rm rec} = 0.5 D_{\rm H_2} K_{bbb} n_2^3 A \approx 5\,\mu$W.

The ripplon cooling power at the same temperature, estimated using the above assumptions, is $\gtrsim 35$ nW. This leads to an estimate $f_{\rm dir} \gtrsim 0.006$. The error bars on the experimental data suggest an uncertainty of approximately 50% in this value, mainly due to the temperature uncertainty in the measured data. A true lower bound is therefore $f_{\rm dir}^{\rm min} = 0.003$. The estimated lower bound of $f_{\rm dir}$ thus obtained agrees well with the upper bound established by the Kyoto group, $f_{\rm dir}^{\rm max} = 0.014$ [33].

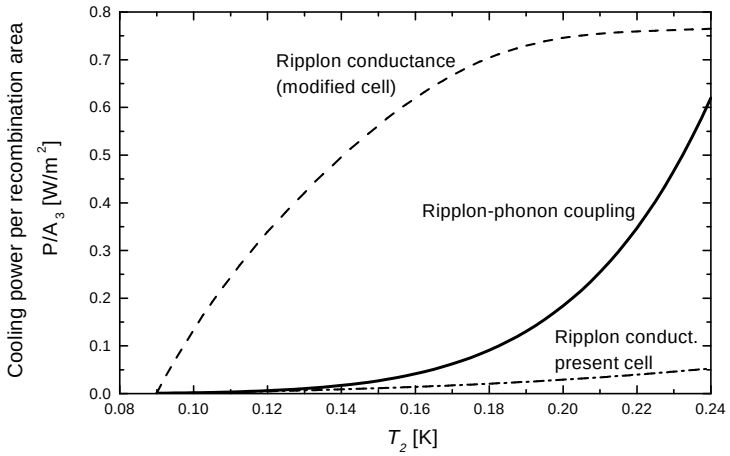

Figure 5.13: Calculated cooling power per effective recombination area, for a modified compression cell with a smaller effective area, and for the present cell. A value of 40 nW/K was used for the heat conductance of the helium surface. Solid line: Ripplon-phonon coupling contribution (The ripplon-phonon cooling power per effective area is independent of size). The bulk helium temperature is 0.09 K.

5.7.3 Model of an improved compression cell

The above considerations have led to the design of a revised compression cell, with a much smaller effective area for recombination and at the same time a larger area for the excited molecules to dissipate their energy [30]. A full account of this design is outside the scope of this thesis. In this section the improved design will be analyzed by applying the population dynamics and heat transport equations to it.

The proposed new compression cell is based on a helium meniscus with radius of curvature $R_c = 200\mu$ in a field gradient of 6T/mm [30]. This yields a circularly symmetric two-dimensional gas with an effective third-order recombination area $A_3 \approx 7 \times 10^{-3}$ mm^2 at 100 mK, which is three orders of magnitude smaller than the present effective area. The estimated cooling power for such a spot is shown in figure 5.13, and it is obvious from this graph that the cooling power is fully dominated by ripplons for $T < 0.2$ K. In the present compression cell, ripplon cooling was always negligible. The following changes in the heat transport model for the compression cell have been made:

- The contribution of ripplon conductance has been included in the heat exchange equation (5.9). A relatively pessimistic ripplon conductivity of 40 nW/K has

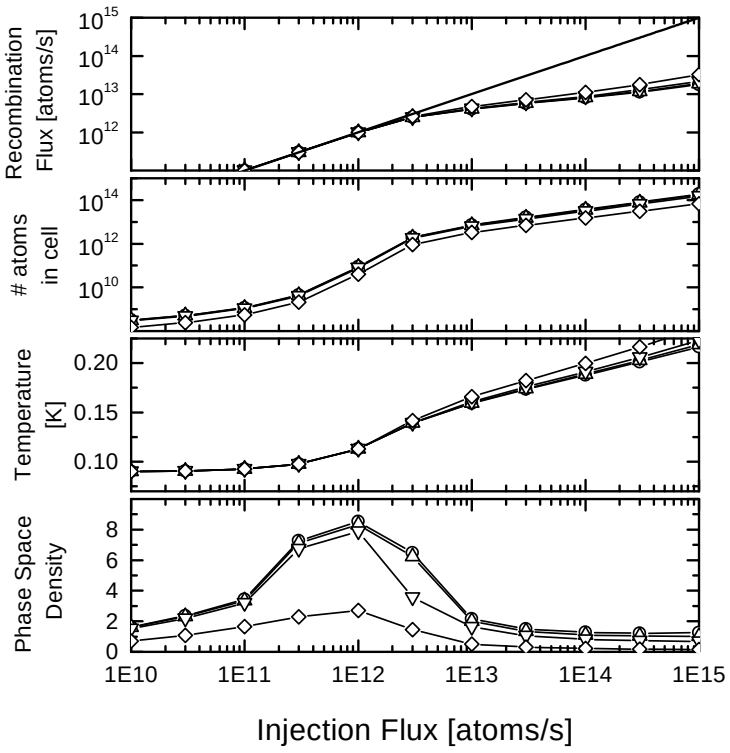

Figure 5.14: Calculated steady-state behavior of the improved compression cell, using the estimate $f_{\mathrm{dir}} = 0.006$. Circles: injection of pure b-state atoms, $\triangle$: injection of 3% a-state atoms, ∇: 10 % a, $\diamondsuit$: 50 % a. The straight line in the upper panel corresponds to a recombination flux equal to the injection flux.

been assumed. The high density spot will be surrounded by bulk helium, on which the conductivity may be much higher.

- The dominant heating mechanism is now direct heat release in the recombination event, the amount of heat released by molecules that return to the meniscus can be ignored.
- The amount of heat transferred to the bulk gas can be ignored, as the number of bulk gas atoms is much lower, and the excited molecules dissipate their energy away from the bulk gas.

This adapted model predicts that the phase-space density reached in the modified compression cell will be an order of magnitude higher than in the present apparatus, as shown in figure 5.14. This maximum is reached at an injection flux of approximately

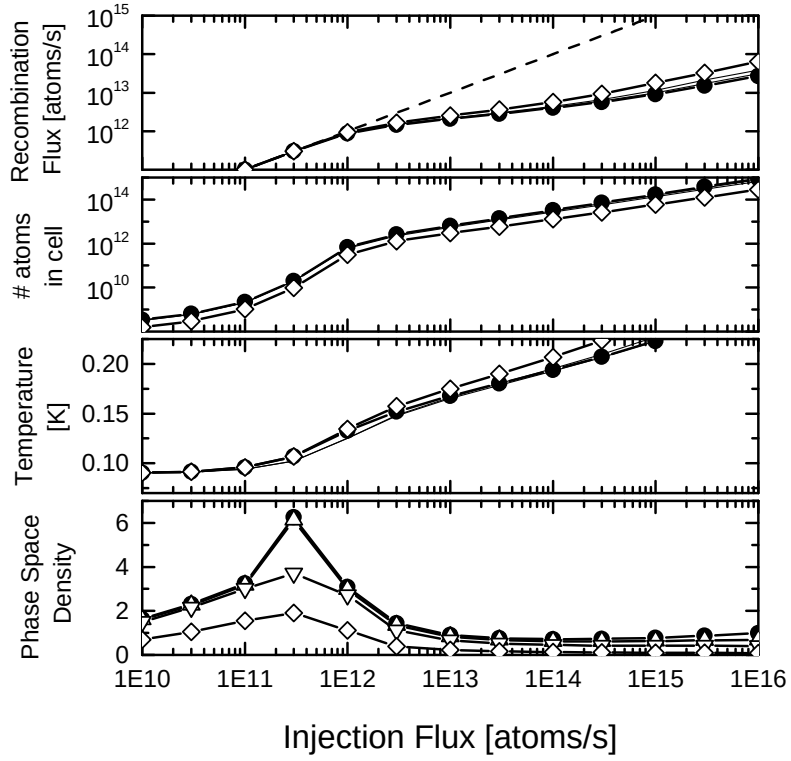

Figure 5.15: Behavior of the improved cell at the established upper bound for direct energy release, $f_{\rm dir} = 0.014$. Black dots: injection of pure b-state atoms, open diamonds 50 % a atoms, intermediate curves for 3% and 10 % a-impurities. The dashed line in the upper panel corresponds to a recombination flux equal to the injection flux.

3×10^{11} atoms per second, and if the injected gas is hyperfine polarized, the adsorbate will become degenerate. Remarkably, one has to tune the injection flux accurately in order to obtain a degenerate sample, as when the injection flux is too high the recombination heat will cause the sample to become non-degenerate again. As can be seen from the temperatures shown in figure 5.14, in the modified cell this overheating will only become important when a high phase-space density already has built up.

In figure 5.14, the estimate $f_{\rm dir} = 0.006$ for the fraction of recombination heat released directly to the surface was used. The fraction $f_{\rm dir}$ might be larger, but even at the upper bound, $f_{\rm dir} = 0.014$ it is still possible to reach a phase space density of $n_2\Lambda^2 \approx 6$, as shown in figure 5.15. However, the injection flux will need to be tuned carefully to obtain this density. At this phase-space density a two-dimensional Bose

condensate will have formed, and third order recombination rates will be suppressed by a factor ≈ 6. This will lead to a reduction in recombination heating, and therefore even higher phase-space densities may be possible.

Based on this model of the heat transport and population dynamics, we conclude that the prospects for creating a two-dimensional Bose condensate in a modified version of the compression cell are very good. The phase space density in the new compression cell will be well above $n_2\Lambda^2 = 3.3$, the value where the condensate was observed to form in the experiments by Safonov *et al.* [4].

References

[1] Rudolf Sprik, *Experiments on spin-polarized hydrogen at high density* , Ph.D. thesis, Universiteit van Amsterdam, 1986 (unpublished).

[2] R. Sprik, J. T. M. Walraven, G. H. van Yperen and Isaac F. Silvera, *Experiments with "doubly"-spin-polarized atomic hydrogen*, Phys. Rev. B **34**, 6172 (1986).

[3] J. J. Berkhout, *Atomic hydrogen and the surface of liquid helium*, Ph.D. Thesis, Universiteit van Amsterdam, 1994 (unpublished).

[4] A. I. Safonov, S. A. Vasilyev, I. S. Yasnikov, I. I. Lukashevich and S. Jaakkola, *Observation of quasicondensate in two-dimensional atomic hydrogen*, Phys. Rev. Lett. **81**, 4545 (1998).

[5] J. W. Statt and A. J. Berlinsky, *Theory of spin relaxation and recombination in spin-polarized atomic hydrogen*, Phys. Rev. Lett. **45**, 2105 (1980).

[6] D. O. Edwards and W. F. Saam, *The Free Surface of Liquid Helium*, Progress in Low Temperature Physics, edited by D. F. Brewer (North-Holland, Amsterdam 1978), Vol. VII, p. 284.

[7] R. Sprik, J. T. M. Walraven , G. H. van Yperen and Isaac F. Silvera, *State-dependent recombination and suppressed nuclear relaxation in atomic hydrogen*, Phys. Rev. Lett. **49**, 153 (1982).

[8] R.W. Cline, T.J. Greytak, and D. Kleppner, *Nuclear polarization of spin-polarized hydrogen*, Phys. Rev. Lett. **47**, 1195 (1981).

[9] Yu. Kagan, I. A. Vartanyants and G. V. Shlyapnikov, *Kinetics of decay of metastable gas phase of polarized atomic hydrogen at low temperatures*, Sov. Phys. JETP **54**, 590 (1981).

[10] I. F. Silvera and J. T. M. Walraven, *Spin Polarized Atomic Hydrogen*, in *Progress in Low Temperature Physics*, edited by D. F. Brewer (Elsevier, Amsterdam 1986), Vol. 10, p. 139.

[11] J. Helffrich, M. P. Maley, M. Krusius and J. C. Wheatley, *Measurement of thermal accomodation of spin-polarized hydrogen on a saturated ^{4}He film at 0.18-0.4 K*, Phys. Rev. B **34**, 6550 (1986).

[12] M. W. Reynolds, I. D. Setija and G. V. Shlyapnikov, *Energy transfer between ripplons and phonons in liquid helium at low temperatures,* Phys. Rev. B **46**, 575 (1992). *Theoretical discussion of the thermal contact between the surface and bulk of liquid He.*

[13] D. S. Zimmerman and A. J. Berlinsky, *Diffusion of H atoms on the surface of liquid* ^{4}*He,* Can. J. Phys. **62**, 590 (1984), and Erratum, Can. J. Phys. **62**, 1177 (1984).

[14] Marcelo Alonso and Edward J. Finn, *Physics*, Addison-Wesley publishing (1992).

[15] Jom Luiten, *Lyman-α spectroscopy of magnetically trapped atomic hydrogen*, Ph.D. Thesis, Universiteit van Amsterdam, 1993 (unpublished).

[16] A. I. Safonov, S. A. Vasilyev, I. S. Yasnikov, I. I. Lukashevich, and S. Jaakkola, *Magnetic compression of two-dimensional spin-polarized atomic hydrogen* JETP Lett. **61**, 1032 (1995), same authors and E. Tjukanov, LT21, Czech. J. Phys. **46**, 539 (1996).

[17] D. S. Zimmerman and A. J. Berlinsky, *The sticking probability for hydrogen atoms on the surface of liquid* ^{4}He, Can. J. Phys. **61**, 508 (1983).

[18] J.J. Berkhout, O.J. Luiten, I.D. Setija, T.W. Hijmans, T. Mizusaki and J.T.M. Walraven, *Quantum reflection: Focusing of hydrogen atoms with a concave mirror*, Phys. Rev. Lett. **63**, 1689 (1989).

[19] Yu. Kagan, N.A. Glukhov, B.V. Svistunov and G.V. Shlyapnikov, *Kapitza resistance in* H↓ *gas at limiting surface density*, Phys. Lett A **143**, 477 (1990).

[20] P.W.H. Pinkse, A. Mosk, M. Weidemüller, M.W. Reynolds, T.W. Hijmans, and J.T.M. Walraven, *Adiabatically changing the phase-space density of a trapped Bose gas*, Phys. Rev. Lett. **78**, 990 (1997).

[21] B. V. Svistunov, T. W. Hijmans, G. V. Shlyapnikov and J. T. M. Walraven, *Resonant-light absorption and the problem of observing the Kosterlitz-Thouless transition in spin-polarized atomic hydrogen adsorbed on a liquid-He surface*, Phys. Rev. B **43**, 13412 (1991).

[22] D. O. Edwards and I. B. Mantz, *The adsorption of atomic hydrogen to the surface of* ^{4}*He*, supplement **C7** of Journal de Physique **41**, 257 (1980).

[23] J. T. M. Walraven, *Atomic hydrogen and liquid helium surfaces*, in *Fundamental systems in quantum optics*, Les Houches summer school LIII, 1990, ed. J. Dalibard, J. M. Raimond and J. Zinn-Justin, (Elsevier Science, Amsterdam, 1992).

[24] J. M. Doyle, J. C. Sandberg, I. A. Yu, C. L. Cesar, D. Kleppner, and T. J. Greytak, *Hydrogen in the submillikelvin regime: Sticking probability on superfluid* ^{4}He, Phys. Rev. Lett. **67**, 603 (1991).

[25] T. W. Hijmans, J. T. M. Walraven, and G. V. Shlyapnikov, *Influence of the substrate on the low-temperature limit of the sticking probability of hydrogen atoms on* He *films*, Phys. Rev. B **45**, 2561 (1992).

[26] J. Helffrich, M. Maley, M. Krusius and J. C. Wheatley, *Measurement of thermal accommodation of spin-polarized hydrogen on a saturated* ^{4}He *film at 0.18 - 0.4* K, Phys. Rev. B **34**, 6550 (1986).

[27] D. M. Stamper-Kurn, H.-J. Miesner, A. P. Chikkatur, S. Inouye, J. Stenger, and W.

Ketterle, *Reversible formation of a Bose-Einstein condensate*, Phys. Rev. Lett. **81**, 2194 (1998).

[28] E. M. Lifshitz and L. P. Pitaevskii, *Statistical physics part 2*, volume 9 of Landau and Lifshitz, *Course of theoretical physics*, Butterworth-Heinemann, Oxford (1980, 1996).

[29] J. T. M. Walraven, in *Quantum dynamics of simple systems*, proceedings of SUSSP44, ed. G. L. Oppo, S. M. Barnett, E. Riis and M. Wilkinson, (SUSSP publishing, Edinburgh and IOP publishing, Bristol, 1996).

[30] M. W. Reynolds and T. W. Hijmans, private communication.

[31] Harald F. Hess, David A. Bell, Gregory P. Kocjanski, Daniel Kleppner, and Thomas J. Greytak, *Temperature and magnetic field dependence of three-body recombination in spin-polarized hydrogen*, Phys. Rev. Lett. **52**, 1520 (1984).

[32] S. A. Vasilyev, E. Tjukanov, M. Mertig, A. Ya. Katunin, and S. Jaakkola, *Distribution of Surface Recombination Energy of Spin-Polarized Hydrogen on Liquid Helium,* Europhys. Lett. **24**, 223 (1993).

[33] A. Fukuda, M. Yamane, A. Matsubara, T. Arai, J.S. Korhonen, J. T. M. Walraven, and T. Mizusaki,*Cooling of two-dimensional spin-polarized atomic hydrogen*, LT 21, Czech. J. Phys. **46**, 541 (1996).

[34] I. B. Mantz, D. O. Edwards and V. U. Nayak, *Ripplons,* ^{3}He*, and heat conduction on the surface of superfluid* ^{4}He, Phys. Rev. Lett **44**, 663 (1980).

[35] D. A. Bell, H. F. Hess, G. P. Kochanski, S. Buchman, L. Pollack, Y. M. Xiao, D. Kleppner and T. J. Greytak, *Relaxation and recombination in spin-polarized atomic hydrogen*, Phys. Rev. B **34**, 7670 (1986).

[36] W. N. Hardy, M. D. Hürlimann and R. W. Cline, *Application of atomic hydrogen at low temperature: The recirculating cryogenic hydrogen maser*, LT-18, Japan. J. Appl. Phys. **26**, 1065 (1987).

[37] A. Matsubara, T. Arai, J. S. Korhonen, T. Suzuki, A. Masaike, J. T. M. Walraven, T. Mizusaki and A. Hirai, *Cooling of polarized atomic hydrogen adsorbed on liquid helium*, Proceedings of LT20, Physica B **194-196**, 899 (1994).

[38] Eric S. Meyer, Zuyu Zhao, John C. Mester, and Isaac Silvera, *Nonlocal distribution of the recombination energy in spin-polarized atomic hydrogen*, Phys. Rev. B **50**, 9339 (1994).

[39] M. W. Reynolds, private communication.

Chapter 6

Photoassociation of Spin-polarized Hydrogen

Using Lyman-α spectroscopy we observe photoassociation of spin-polarized hydrogen atoms to bound vibrational levels of the triplet $a^3\Sigma_g^+$ potential. At a density of 10^{16} atoms per cm^3 we directly observe light absorption and fluorescence in the photoassociation process. The observed line positions agree with ab initio calculations to within the precision of present theory. Magnetic sublevels in the photoassociation spectra indicate an effective internal field which we identify with a nonadiabatic term in the Hamiltonian, describing redistribution of angular momentum between the nuclei and the electrons. We present quantitative models for the magnetic field dependence of the molecular energy and the photoassociation lineshape.
[This chapter has been published as: A. P. Mosk, M. W. Reynolds, T. W. Hijmans and J. T. M. Walraven, Phys. Rev. Lett. **82**, 307 (1999).]

6.1 Introduction

Photoassociation, the process in which a pair of unbound atoms is excited optically into a bound molecular state, is a dramatic form of optical collision. It is also an extremely precise tool for probing the highest energy levels in a molecular potential. Photoassociation (PA) has been observed in laser cooled alkali gases (see e.g. [1, 2, 3]), where it has been used to accurately characterize interatomic interactions and to

obtain valuable insights into the physics of these gases. The determination of the ground state scattering lengths of alkali atoms, and the effect of optical and magnetic fields on collision processes are based on PA spectra (see e.g. [4]).

In this letter we present the first observation of PA in atomic hydrogen (H). The case of H is particularly interesting for several reasons. Firstly, experimental results can be used to test the ab initio calculations of ground state and excited state collision properties which claim very high accuracy for this simplest molecule (see e.g. [5]). Moreover, in contrast to alkali systems, in H spin-orbit (LS) coupling is very small. In addition, nonadiabatic effects due to the finite mass of the nuclei are most readily investigated in the lightest molecule. In a dense gas of H [6] the PA lines can serve as a sensitive probe of the gas density. PA spectroscopy may also be of use to explore the properties of degenerate samples of H [7], since it probes the two particle correlator.

In contrast to PA experiments in alkali gases, we reach densities that are high enough that we can directly detect the PA process via light absorption and subsequent fluorescence. We obtain these high densities by confining *high field seeking* H (H$\downarrow$) in a cryogenic sample cell [8]. Our measurements take place in a magnetic field that we can vary between 4 and 7 T. The line positions we observe are in agreement with the existing ab initio theory. However, the theory needs to be extended to include magnetic field dependence to allow for a full comparison. We find that the excited H_2 molecule displays an internal field of order 1 T, which we identify with a nonadiabatic term in the hamiltonian.

6.2 Apparatus

The apparatus we use to cool and compress H$\downarrow$ is described in the literature [9, 6]. It consists of two volumes with liquid helium coated walls: a 0.3 K buffer volume, which we use to precool atoms generated in a cryogenic discharge, and a smaller cold cell, with a wall temperature of 0.1 K. Through preferential recombination almost all atoms in the sample are in the $f = 1$, $m_f = -1$ state. Consequently, the ground state atoms interact via the $b^3\Sigma_u^+$ interatomic potential, which has no bound states. The atoms in the buffer volume can escape over a magnetic field barrier towards the cell. Once thermalized to the cell temperature the atoms lack the thermal energy to return across the barrier to the buffer. By this mechanism the atoms are effectively compressed into the cell. A gas density of 10^{16} atoms per cm^3 at a temperature of 0.15 K is reached routinely in this way. We determine the density and temperature of the gas by spectroscopy on the Lyman-α transition at $\lambda \approx 122\,\mathrm{nm}$ [10]. We measure both transmission and light induced fluorescence (LIF) spectra by scanning the fre-

quency of the Lyman-α light source. The fluorescent light is detected after conversion to visible wavelengths.

6.3 Observations

PA lines appear in the absorption and LIF spectra at densities higher than $\approx 10^{15}$ atoms per cm^3. An example is given in Fig. 6.1. The detuning Δ is measured with respect to the centroid ω_{2P} of the 2P fine structure multiplet. As discussed below, in the molecules under consideration fine structure plays no role. Therefore, when discussing binding energies of the PA levels we will suppress the effect of fine structure on the dissociation limit by defining the level energies relative to ω_{2P}. The fluorescence peak at detuning $\Delta = -134\,\mathrm{GHz}$ is attributed to PA in the cell. A corresponding dip in the transmission signal is observed. The stronger transmission dip at $-141\,\mathrm{GHz}$ is due to PA in the buffer; it is Zeeman shifted from the cell line as the field in the

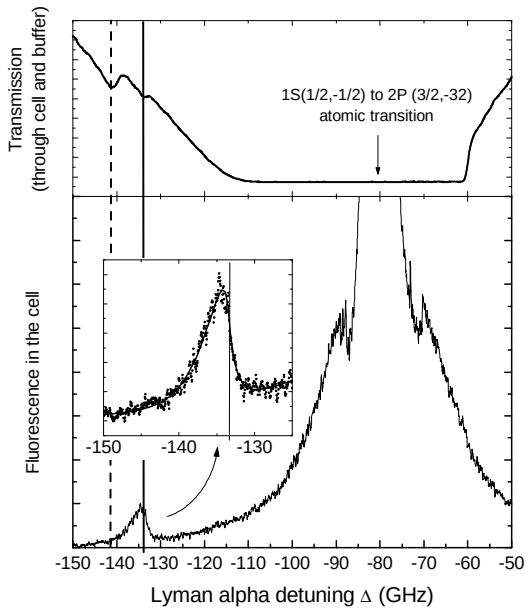

Figure 6.1: Transmission and fluorescence spectra of H at $n \simeq 10^{16}\,\mathrm{cm}^{-3}$. The feature at $\Delta = -134$ GHz is a PA line. The large structure dominating the fluorescence spectrum around $\Delta = -80\,\mathrm{GHz}$ is the atomic transition. Insert: The PA lineshape is fit to Eq. (6.6). The vertical line denotes the inferred position of the unbroadened line. The magnetic field is 6 T in the cell and 1 T higher in the buffer.

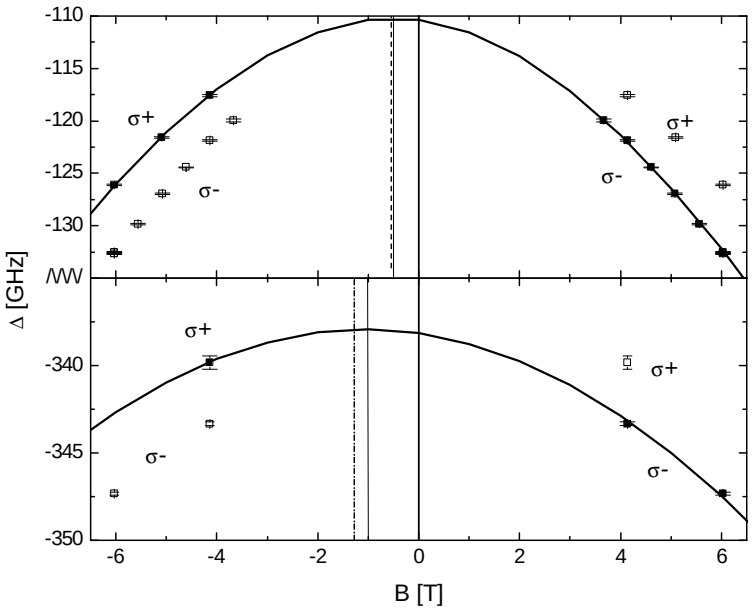

Figure 6.2: Magnetic field dependence of $v = 20$ and $v = 19$ PA lines. The data points are shown twice, once reflected in the $B = 0$ axis with the opposite polarization. The error bars indicate the relative precision of the data points, the absolute frequency accuracy is 1 GHz. The curves are model calculations, with only an overall energy shift as a free parameter. The effective internal field B_i, as estimated from Eq. (6.3) is indicated (dashed vertical line), as well as the actual symmetry axis of the curve (full line).

buffer is 1 T higher. There is no fluorescence signal corresponding to this dip because the fluorescence detector is not visible from the buffer volume. For a given field, we observe three PA peaks separated by a few hundred GHz. The positions of the PA lines are field dependent, as shown in Fig. 6.2. Apparently, there is a strong second order Zeeman effect and a significant polarization dependence of the Zeeman shifts.

6.4 Identification of the levels

Lyman-α light can excite a pair of atoms from the $b^3\Sigma_u^+$ state to the $a^3\Sigma_g^+$ and $c^3\Pi_g^-$ states [11]. The $c^3\Pi_g^-$ state is repulsive at long range, leaving only the $a^3\Sigma_g^+$ as a candidate upper state for free-bound transitions. Figure 6.3 shows the positions of the PA lines which we have found. To compare with existing theory, the line positions have been extrapolated to zero field in a way discussed below. Figure 6.3 also shows

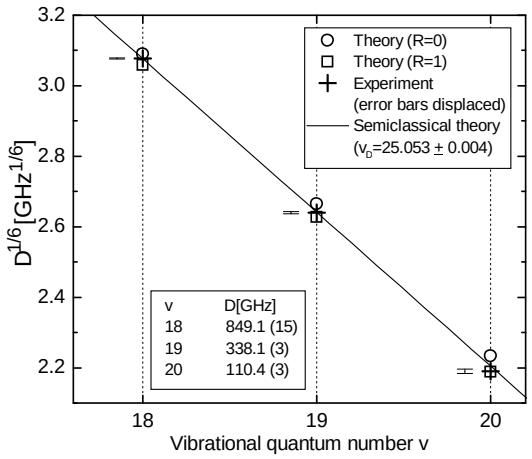

Figure 6.3: Molecular binding energy in the $a^3\Sigma_g^+$ potential to the one-sixth power as function of vibrational quantum number. The theory points shown are the bound states in the adiabatic approximation [5] with nuclear motional angular momentum R = 0 and 1, the line is a fit of quasiclassical theory to our data. The indicated uncertainty is statistical. Insert: experimental dissociation energies, extrapolated to B=0.

the dissociation energies of the calculated $R = 0$ and $R = 1$ bound states as obtained by ab initio calculation [5]. (R is used to indicate the angular momentum of nuclear motion). From Fig. 6.3, we identify the observed lines as free-bound transitions to the $v = 18, 19, 20$ vibrational levels of the $a^3\Sigma_g^+$ potential. The potential by Kołos and Rychlewski [5] was calculated with the aim to describe tightly bound molecules, experimental data up to $v = 6$ are discussed in [5]. Apparently it still describes the $v = 20$ molecule well. Quasiclassical theory [12] predicts that in the potential $V(r) = -2C_3/r^3$ the molecular binding energy D scales with v as $D^{1/6} = \hbar\mu^{-1/2}2^{-1/3}C_3^{-1/3}(v_D - v)$. Here, μ is the reduced mass (half the mass of the H atom). This theory does not predict the vibrational quantum number at dissociation v_D. We obtain $v_D = 25.05$ from a fit to the data, as shown in Fig. 6.3. This quasiclassical theory may break down near the dissociation limit due to LS coupling, as has been observed, e.g. in Ref. [13], in the related $B\,^1\Sigma_u^+$ state.

6.5 Magnetic field dependence

We will now discuss the physics which produces the observed field dependence. For the range of internuclear distances (20-35 a_0) of interest, the resonant dipole interaction

is the dominant term in the hamiltonian. It is more than an order of magnitude larger than LS terms, (the LS splitting in H is 10.97 GHz) and all first order LS terms cancel in a Σ state (Hund's case (b) [14]). Therefore, LS coupling can be neglected, and the spins will remain aligned to the magnetic field in the ground state as well as in the excited state. The Zeeman effect must therefore be caused by orbital motion of the electrons. At 0.15 K, s-wave collisions between H atoms are dominant, so the initial $b^3\Sigma_u^+$ quasimolecule has total motional angular momentum $N = 0$ [15]. After absorbing a $\sigma_\pm$ polarized photon the molecule has $N = 1, M = \pm 1$. Because the light propagates parallel to the magnetic field, π transitions are not excited. In the absence of LS coupling, reversing the polarization of the light (and therefore the M of the final state molecule) is physically equivalent to reversing the applied magnetic field, while leaving M unchanged. This allows us to treat the σ_+ data points as if they were σ_- points taken at a negative field (see Fig. 6.2). The polarization dependent Zeeman shift shows that M couples quite strongly to the magnetic field, which indicates that on average a significant fraction of the angular momentum M must be in the electron orbital motion, even in zero field.

When the nuclei are far apart, there are no shared electrons and the molecule consists of two atoms, bound by exchanging virtual photons. Since one of these atoms is in the 2P state, the molecule has L=1 and we can express the molecular state in a basis of atomic (m_L) states. Coupling to the nearby 2S state is ignored in this long-range approximation, as it does not have resonant dipole interaction. The Schrödinger equation of the molecule acts on three-component vector wavefunctions $\mathbf{\Psi}(r, \theta, \phi)$ where the components of $\mathbf{\Psi} = (\Psi_{-1}, \Psi_0, \Psi_{+1})$ represent the different m_L states of the excited atom, r is the internuclear distance and θ and ϕ are the angles between the internuclear axis and the laboratory frame. The quantization axis for L is taken in the laboratory frame to show more clearly the implications of angular momentum conservation. To transform the vector between the laboratory frame and the molecular frame, where m_L becomes Λ, one must use a three-dimensional representation $D^{(1)}(0, \theta, \phi)$ of the rotation group [14]. The resonant dipole interaction, which is attractive as $-2C_3/r^3$ for the $^3\Sigma_g$, is repulsive as C_3/r^3 for the $^3\Pi_g$ state [16]. The Schrödinger equation in the laboratory frame reads

$$\begin{aligned} E\mathbf{\Psi} &= -\frac{\hbar^2}{2\mu}\nabla^2\mathbf{\Psi} \\ &\quad + \frac{C_3}{r^3} D^{(1)}(-\phi, -\theta, 0) \begin{pmatrix} 1 & & \\ & -2 & \\ & & 1 \end{pmatrix} D^{(1)}(0, \theta, \phi)\mathbf{\Psi} \end{aligned} \tag{6.1}$$

$$+\mu_B B \begin{pmatrix} -1 & & \\ & 0 & \\ & & 1 \end{pmatrix} \mathbf{\Psi}.$$

In the molecular states we observe, the interaction term is dominant, the magnetic field term and commutators of the Laplacian and the $D^{(1)}$ matrices can be treated as perturbations. In good approximation, a Σ wavefunction with $N = 1, M = \pm 1$ can be written in the lab frame as

$$\mathbf{\Psi}_M(r, \theta, \phi) \approx \Psi(r) Y_{1,M}(\theta, \phi) D^{(1)}(-\phi, -\theta, 0) \begin{pmatrix} 0 \\ 1 \\ 0 \end{pmatrix}. \tag{6.2}$$

When substituting Eq. (6.2) in Eq. (6.1) the action of the ϕ derivative in the Laplacian on the D matrices gives rise to an extra term, of a tensor form similar to the Zeeman term. This term acts like an effective internal magnetic field B_i. Derivatives of the $D^{(L)}$ transformation matrices are often neglected; in heavy or tightly bound molecules this is a good approximation. However, here we need to keep track of these terms.

We have obtained the curves in Fig. 6.2 by solving Eq. (6.1) in a way we briefly sketch here: First, the ϕ dependence is eliminated from Eq. (6.1). Then we transform the equation to the molecular frame, where the dominant term is diagonal. The r derivatives of the orientation of $\mathbf{\Psi}$ can be neglected (cf. Eq. (6.2)), we also neglect its θ derivatives, which contribute only a small energy shift. The equation now assumes a scalar form, which is easily solved. The resulting curves are in very good agreement with the data. Apart from an overall frequency shift the calculation has no free parameters. We use the zero field values of this calculation to compare with $B = 0$ theory in Fig. 6.3.

6.6 Approximation for the internal field

To gain insight we compare the ϕ derivative term in Eq. (6.1) to the Zeeman term, which leads to an analytical approximation of the internal field B_i,

$$\mu_B B_i \approx -M \frac{3\hbar^2}{4\mu} \frac{1}{r_{\text{eff}}^2}. \tag{6.3}$$

For the effective radius r_{eff} we take the most probable r (the maximum of the $B = 0$ wavefunction in the adiabatic approximation). This leads to an estimated $B_i = 0.6\,\text{T}$ for the $v = 20$ state and $B_i = 1.2\,\text{T}$ for the $v = 19$ state. The simple estimate (6.3) agrees well to both experiment and the calculated field dependence (see Fig. 6.2).

By combining B_i with the second order Zeeman effect it is possible to define an effective magnetic moment, which is $0.041\,\mu_B$ for the $v = 20$ state and $0.029\,\mu_B$ for $v = 19$. This is almost two orders of magnitude larger than the nuclear magneton. This internal field is not unique to H_2 molecules. In fact, Eq. (6.3) holds for any molecule that resembles a S and P pair of (not even necessarily identical!) atoms, as long as LS coupling is small. When LS coupling is large a similar effect arises due to the $D^{(S)}$ matrices that transform the spin part of the wavefunction. In the lightest alkali, Li, for a typical state excited in PA ($1\,^3\Sigma_g^+, v = 59$) the internal field is high (≈ 0.08 T), but due to the weak second order Zeeman effect the magnetic moment is only of the order of the nuclear magneton.

6.7 Polarization dependence of excitation probabilities

From the eigenvectors of Eq. (6.1) we can infer the relative excitation probabilities of the different transitions. For the $v = 20$ state at $B = 6$ T we predict an excitation cross-section that is 4.4 times larger for the σ_- transition than for the σ_+ transition. Experimentally we find a ratio of 6 ± 1.5 to 1.

6.8 Lineshape

To obtain accurate line positions from the asymmetrically broadened lines (see Fig. 6.1) it is crucial that we understand the lineshape in detail. The lines are broadened due to the kinetic energy distribution of the colliding atoms (to the red) and due to the Zeeman effect (to the blue). The kinetic energy broadening reflects the thermal energy that the atoms have in the initial state. The excitation takes place around the outer turning point r_0, so that the probability to excite the atoms is proportional to the initial ground state wavefunction $\Psi_0(r_0)$ squared. The initial state is an s-wave, $\Psi_0(r) \propto \sin(kr)/r$ (the s-wave scattering length of the ground state is ignored here), the thermal probability that the system will be found in this state is $\propto \exp(-\hbar^2 k^2/2\mu k_B T)$, which leads to the kinetic energy lineshape function

$$f_k(\delta\omega) \propto |\delta\omega|^{-1/2} \sin^2(r_0(2\mu|\delta\omega|/\hbar)^{1/2}) e^{-\hbar|\delta\omega|/k_B T} \tag{6.4}$$

for $\delta\omega < 0$, zero otherwise. The magnetic field gradient in our system is approximately constant, with the highest field ($B_{\max}$) occurring at the cell bottom ($z = 0$). The density profile of H$\downarrow$ atoms in such a field is exponential, $n(z)=n(0)e^{-\mu_B z|\partial B/\partial z|}/k_B T$,

and the PA absorption probability varies as $n(z)^2$. Around $B_{\max}$, the field dependence of the PA line position can be linearized to $\hbar\delta\omega \approx 2g\mu_B(B - B_{\max})$, where $2g\mu_B$ is the field derivative of the line position at $B = B_{\max}$. The Zeeman lineshape follows,

$$f_z(\delta\omega) = e^{-\hbar\delta\omega/gk_BT} \tag{6.5}$$

for $\delta\omega > 0$ and zero otherwise. The lineshape is the convolution of f_k and f_z, and can be expressed in error functions:

$$F(\delta\omega) \propto e^{-\hbar\delta\omega/gk_BT}(\mathrm{erfc}(k_0) - e^{-b^2}\,\mathrm{Re}\,\mathrm{erfc}(k_0 + ib)) \tag{6.6}$$
$$b = \sqrt{\frac{2\mu r_0^2 k_B T}{\hbar^2(1+1/g)}}\,;\; k_0 = \mathrm{Re}\sqrt{\frac{-\hbar\delta\omega(1+1/g)}{k_B T}}.$$

Doppler, lifetime and instrumental broadening are neglected. This lineshape is shown in Fig. 6.1. The PA lineshape for alkali gases in a magneto-optical trap, derived in [17], is different due to the much lower temperature in those experiments.

6.9 Weakly bound and dissociative levels

The fluorescence side peaks in the red and blue wing of the atomic transition (Fig. 6.1) might be due to PA to very shallow levels. Adiabatic theory predicts that there are bound states up to $v = 25$, but these states may be strongly perturbed by the magnetic field and LS coupling. The peak in the blue wing of the atomic transition suggests there may be PA to a dissociative level [13].

Acknowledgments

The authors would like to thank Wim van der Zande, Hugo Boesten, Boudewijn Verhaar and Pepijn Pinkse for valuable discussions, Otto Höpfner, Joost Overtoom, Michiel Groeneveld and Bert Holsbeeke for technical support. This work is supported by the Stichting voor Fundamenteel Onderzoek der Materie (FOM). The research of MWR is supported by the Royal Netherlands Academy of Arts and Sciences.

References

[1] P. D. Lett, K. Helmerson, W. D. Phillips, L. P. Ratliff, S. L. Rolston and M. E. Wagshul, *Spectroscopy of Na_2 by photoassociation of laser-cooled Na*, Phys. Rev. Lett. **71**, 2200 (1993).

[2] J. D. Miller, R. A. Cline and D. J. Heinzen, *Photoassociation spectrum of ultracold Rb atoms*, Phys. Rev. Lett. **71**, 2204 (1993).

[3] E. R. I. Abraham, W. I. McAlexander, J. M. Gerton, R. G. Hulet, R. Côté and A. Dalgarno, *Triplet s-wave resonance in ^6Li collisions and scattering lengths of ^6Li and ^7Li*, Phys. Rev. A **55**, R3299 (1997).

[4] A. J. Moerdijk, B. J. Verhaar and A. Axelson, *Resonances in ultracold collisions of ^6Li, ^7Li and ^{23}Na*, Phys. Rev. A **51**, 4852 (1995).

[5] W. Kołos and J. Rychlewski, *The $a^3\Sigma_g^+$ state of the hydrogen molecule*, J Mol. Spec. **169**,341 (1995). *The dissociation energies of the $v > 17$ states of H are incorrectly calculated in this paper. We have recalculated them using the potentials from this reference, employing a larger range of integration.*

[6] A. P. Mosk, M.W. Reynolds, T. W. Hijmans and J.T.M. Walraven, *Optical excitation of atomic hydrogen bound to the surface of liquid helium*, chapter 4 of this thesis, Phys. Rev. Lett. **81**, 4440 (1998).

[7] D. G. Fried, T. C. Killian, L. Willmann, D. Landhuis, S. C. Moss, D. Kleppner and T. J. Greytak, *Bose-Einstein condensation of atomic hydrogen*, Phys. Rev. Lett. **81**, 3811 (1998).

[8] I. F. Silvera and J. T. M. Walraven, *Spin Polarized Atomic Hydrogen*, in *Progress in Low Temperature Physics*, edited by D. F. Brewer (Elsevier, Amsterdam 1986), Vol. 10, p. 139.

[9] A. P. Mosk, P.W.H. Pinkse, M.W. Reynolds, T.W. Hijmans and J.T.M. Walraven, *Apparatus for the optical study of atomic hydrogen on the surface of liquid helium*, J. Low Temp. Phys. **110**, 199 (1998), see also chapter 2 of this thesis.

[10] O.J. Luiten, H.G.C. Werij, I. D. Setija, M.W. Reynolds, T.W. Hijmans and J.T.M. Walraven, *Lyman-α spectroscopy of magnetically trapped atomic hydrogen*, Phys. Rev. Lett. **70**, 544 (1993)

[11] See, e.g., G. Herzberg, *Molecular Structure and Molecular Spectra, I. Spectra of Diatomic Molecules*, D. van Nostrand, New York, 1950.

[12] R. J. LeRoy and R. B. Bernstein, J. Chem. Phys. **52**, 3869 (1970).

[13] C. H. Cheng, J. T. Kim , E. E. Eyler and N. Melikechi, *Line shapes and decay dynamics of dissociative resonances above the second dissociation limit of molecular hydrogen*, Phys. Rev. A **57**, 949 (1998).

[14] L.D. Landau and E.M. Lifshitz, *Quantum Mechanics*, Pergamon Press, New York (1977), chapter VIII.

[15] The quantum number of total motional angular momentum, which we denote as N, with z-projection M, is denoted K, m_K in Ref. [14, 11].

[16] J. F. Bukta and W. J. Meath, *Long range interaction energies between ground and first excited state hydrogen atoms using a one centre method*, Mol. Phys. **25**, 1203 (1973).

[17] R. Napolitano, J. Weiner, C. J. Williams, and P. S. Julienne, *Line shapes of high resolution photoassociation spectra of optically cooled atoms*, Phys. Rev. Lett. **73**, 1352 (1994).

Appendix A

Useful constants

A.1 Fundamental constants of nature

Quantity	**Symbol**	**Value**	**Units**	**±(ppm)**
Speed of light in vacuum	c	2.997 924 58	10^{8} m/s	exact
Planck constant	$\hbar$	1.054 572 66	10^{-34} J s	0.6
— in wavenumbers	$2\pi\hbar c$	1.986 447 44	10^{-23} Jcm	
Boltzmann constant	k_{B}	1.380 658	10^{-23} J/K	9
— in gigahertz	$k_{\mathrm{B}}/2\pi\hbar$	20.836 74	GHz/K	
— in wavenumbers	$k_{\mathrm{B}}/2\pi\hbar c$	0.695 038 7	cm^{-1}/K	
Avogadro constant	N_{A}	6.022 136 7	$10^{23}\,\mathrm{mol}^{-1}$	0.6
Bohr magneton	$\mu_{\mathrm{B}} = e\hbar/2m_e$	9.274 015 4	10^{-24} J/T	.3
— in wavenumbers	$\mu_{\mathrm{B}}/2\pi\hbar c$	0.466 864 37	cm^{-1}/T	0.3
— in kelvin	$\mu_{\mathrm{B}}/k_{\mathrm{B}}$	0.671 709 9	K/T	9
— in gigahertz	$\mu_{\mathrm{B}}/2\pi\hbar c$	13.996 241 8	GHz/T	0.3
Electron charge	e	1.602 177 33	10^{-19} C	0.3
Electron mass	m_e	9.109 389 7	10^{-31} kg	0.6
Electron magnetic moment	μ_e/μ_{B}	1.001 159 652 193		10^{-5}
Electron g-factor	g_e	2.002 319 304 386		10^{-5}
Proton mass	m_{p}	1.672 623 1	10^{-27} kg	0.6
— in m_e	m_{p}/m_e	1836.152 701		0.02
Proton magnetic moment	$\mu_{\mathrm{p}}/\mu_{\mathrm{B}}$	1.521 032 202	10^{-3}	.01

The 1986 recommended values of several fundamental constants of nature [1]

A.2 Atomic units

Quantity	**Symbol**	**Value**	**Units**	**±(ppm)**	Remarks
Bohr radius	a_0	0.529 177 249	10^{-10} m	0.045	
Hartree Energy	E_h	4.359 748 2	10^{-18} J	0.6	
– in eV	$E_\mathrm{h}/\{e\}$	27.211 396 1	eV	0.3	
Atomic unit of magnetic field	a.u.	1715.3	T		
Planck constant	$\hbar$	1	a.u.		by def.
Electron charge	e	1	a.u.		by def.
Electron mass	m_e	1	a.u.		by def.

The atomic units, and some constants expressed in a.u.

A.3 Properties of H

Thermal de Broglie wavelength of a H atom:

$$\Lambda_\mathrm{th} = \sqrt{\frac{2\pi\hbar^2}{m_\mathrm{H} k_\mathrm{B} T}} \approx 1.74\,\mathrm{nm}/\sqrt{T[\mathrm{K}]}. \tag{A.1}$$

Thermal velocity of a H atom:

$$\bar{v} = \sqrt{\frac{8k_\mathrm{B}T}{\pi m_H}} = 145.0\sqrt{T[\mathrm{K}]}\ [\mathrm{m/s}]. \tag{A.2}$$

Dissociation energy of the ground state H_2 molecule [2]:

$$D_{H_2} = 7.17471 \times 10^{-19}\,\mathrm{J} = 36118.3(3)\,2\pi\hbar c\,\mathrm{cm}^{-1}. \tag{A.3}$$

A.3.1 Energy levels

Center of gravity of the Lyman-α transition [3]

$$E_{2P} = 2466067.668\,\mathrm{GHz} = 82259.16304\,\mathrm{cm}^{-1} \tag{A.4}$$

Fine structure constant of the $2P$ state [3]

$$\Delta_{2P} = 10.96905\,\mathrm{GHz} \tag{A.5}$$

Fine structure cross-over field for the 2P state (Fine structure dominates for $B < B_\mathrm{LS}$), and the dimensionless field parameter x used in table 3.1.3 :

$$B_\mathrm{LS} = \frac{\Delta_{2P}}{(g_e - 1)\mu_B} = 0.781900\,\mathrm{T}\,;\ x = B/B_\mathrm{LS} \tag{A.6}$$

Hyperfine constant of the 1S ground state

$$a_h = 0.068 k_B\,\mathrm{K} = 9.388 \times 10^{-25}\,\mathrm{J} = 0.101 \mu_B\,\mathrm{T} = 1.42\,\mathrm{GHz} \times 2\pi\hbar \qquad \text{(A.7)}$$

References

[1] E. Richard Cohen and Barry N. Taylor, *The fundamental physical constants*, Phys. Today supplement August 1997, page BG7-BG11.

[2] G. Herzberg, J. Mol. Spectrosc. **33**, 147 (1970).

[3] Pepijn Pinkse, *Evaporatively cooled atomic hydrogen investigated by one- and two-photon optical methods*, (chapter 5), Ph.D. Thesis, Universiteit van Amsterdam, 1997 (unpublished).

Samenvatting

De kwantummechanische eigenschappen van de materie worden duidelijker zichtbaar bij lage temperaturen. Bij temperaturen beneden één Kelvin, echter, is de evenwichtstoestand van alle materialen vast of vloeibaar, en de veelvuldige interacties tussen de atomen in deze gecondenseerde fasen overschaduwen vele kwantummechanische effecten. Men zou deze effecten liever bestuderen in een eenvoudig, verdund systeem. Koude, ijle gassen van atomen zijn precies zulke systemen, en hoewel ze niet in absoluut thermisch evenwicht verkeren, zijn ze stabiel genoeg om afgekoeld te worden tot temperaturen waarbij men kwantumeffecten kan bestuderen. Daarom noemt men zulke gassen *Kwantumgassen*. Atomair waterstof (H) was het eerste kwantumgas dat gestabiliseerd werd, door Silvera en Walraven in 1980 [1], en sindsdien is het aantal experimenten met ultrakoude gassen snel gestegen, voornamelijk dankzij de ontwikkeling van lasertechnieken om atomen te koelen en op te sluiten.

De best bekende voorbeelden van kwantumgassen zijn tegenwoordig de Bose-gecondenseerde atomaire gassen. Wanneer een gas zo diep gekoeld wordt dat de kwantummechanische onzekerheid in de positie van de atomen groter wordt dan de afstand tussen de atomen, worden macroscopische kwantumeffecten zichtbaar. In een Bose-gas condenseert dan een aanzienlijk deel van de atomen in een enkele kwantumtoestand, het Bose-Einstein condensaat. Bose-condensatie werd voor het eerst waargenomen in 1995, door drie Amerikaanse onderzoeksgroepen [2]. Het eerste Nederlandse Bose-condensaat is dit jaar waargenomen [3].

Atomair waterstof heeft een bijzondere plaats onder de kwantumgassen. Het waterstofatoom is het enige dat zo eenvoudig is dat men alle eigenschappen zonder meer kan berekenen. Bovendien is H het enige gas dat in contact met (met vloeibaar helium beklede) materiële wanden kan bestaan bij temperaturen beneden één Kelvin. Op het oppervlak tussen het vloeibaar helium en het waterstofgas ontstaat een uniek tweedimensionaal kwantumgas van geadsorbeerde waterstofatomen. Dit kwantumgas is vrijwel in thermisch evenwicht met het waterstof bulk-gas, zelfs onder de omstandigheden waarbij men kwantumontaarding voorspelt.

In twee dimensies vindt geen Bose-condensatie plaats: een ideaal (niet-wisselwerkend) twee-dimensionaal Bose-gas zal zich zelfs bij de laagste temperaturen slechts subtiel anders gedragen dan een klassiek gas. Het tweedimensionale geval is echter een grensgeval, zelfs het opsluiten van het gas in een val maakt de faseovergang weer

mogelijk. Ook de interacties tussen de deeltjes kunnen aanleiding geven tot vorming van een tweedimensionaal condensaat. Dit wordt meestal beschreven in termen van de Berezinskiĭ-Kosterlitz-Thouless (KT) theorie voor tweedimensionale superfluïditeit. De KT theorie analyseert de voorwaarden voor superfluïditeit in termen van vortices (draaikolken) in het lokale Bose-condensaat. De KT theorie voorspelt het gedrag van bijvoorbeeld helium-films uitstekend, maar geeft geen uitsluitsel over de vorming van het lokale condensaat, en de verschillende theorieën spreken elkaar tegen.

Metastabiele kwantumgassen, zoals waterstof en lasergekoelde alkali-atomen, lenen zich goed voor het bestuderen van de vorming van het lokale Bose-condensaat. In tegenstelling tot vloeibaar helium kunnen deze gassen optisch bestudeerd worden, en de vervalprocessen leveren informatie over de kwantum-correlaties in het systeem. Superfluïditeit is in deze systemen veel moeilijker te observeren, en in deze zin zijn experimenten met geadsorbeerd waterstof een aanvulling op de experimenten met helium-films.

In hoofdstuk 2 wordt een beschrijving gegeven van de cryogene en optische apparaten die bij de experimenten gebruikt zijn. De belangrijkste onderdelen zijn de lichtbron, die het benodigde licht bij een golflengte van 121,6 nm produceert, en de cryostaat die het koude gas bevat. Het waterstofgas bevindt zich in twee reservoirs, een compressiecel waarin door magnetische compressie hoge gasdichtheden worden behaald, en een buffervolume dat dient als een opslagvolume voor waterstofatomen.

Hoofdstuk 3 bevat een theoretische beschouwing van de voortplanting van licht in een gas van H$\downarrow$. De voortplanting van licht in een ijl gas wordt bestudeerd, en correcties ten gevolge van de hoge dichtheden in ons experiment (één atoom per kubieke optische golflengte) worden geanalyseerd. Te verwachten afwijkingen zijn botsingsverbreding en lichtbrekingseffecten. Uit de analyse blijkt dat geen van beide afwijkingen belangrijk zijn in ons experiment.

Hoofdstuk 4 betreft de waarnemingen die gedaan zijn aan het geadsorbeerde gas. De maximale faseruimtedichtheid die door ons bereikt is, is ongeveer één deeltje per vierkante De Broglie golflengte, dicht bij het regime waar een twee-dimensionaal Bose-condensaat gevormd wordt.

In hoofdstuk 5 wordt verder ingegaan op het transport van deeltjes en energie door onze compressiecel. Er worden deeltjes uitgewisseld tussen het adsorbaat en het driedimensionale gas, en er wordt warmte uitgewisseld tussen het gas, het adsorbaat, het heliumoppervlak en de helium-bulk. De transportprocessen bepalen uiteindelijk de maximale faseruimtedichtheid. Het blijkt dat het gedrag van de bestaande compressiecel nauwkeurig gesimuleerd kan worden. Gebruikmakend van deze simulaties kunnen we de maximale faseruimtedichtheid in een nieuw te bouwen compressiecel

voorspellen.

Tot slot wordt in hoofdstuk 6 de waarneming van foto-associatie in het bulk-waterstofgas in de compressiecel beschreven. Foto-associatie is het proces waarbij onder invloed van het Lyman-α licht twee waterstofatomen een (elektronisch geëxciteerd) molecuul vormen. De vorming van moleculen geeft aanleiding tot lijnen in het absorptie-spectrum. De geëxciteerde moleculen vervallen vervolgens weer, hetgeen aanleiding geeft tot lijnen in het lichtgeïnduceerde-fluorescentie (LIF) spectrum. Uit de lijnposities kan men de bindingsenergieën van de moleculaire toestanden afleiden, deze blijken in goede overeenstemming met de theorie. De snelle rotatie van het waterstofmolecuul geeft aanleiding tot een onverwacht groot magnetisch moment. Om dit te begrijpen voeren we een versimpeld theoretisch model van het waterstofmolecuul in een magneetveld in.

Referenties

[1] I.F. Silvera and J.T.M. Walraven, *Stabilization of atomic hydrogen at low temperature*, Phys. Rev. Lett. **44**, 164 (1980).

[2] De volgende publikaties beschrijven de eerste waarnemingen van Bose-condensatie
M.H. Anderson, J.R. Ensher, M.R. Matthews, C.E. Wieman, and E.A. Cornell, Science **269**, 198 (1995),
K.B. Davis, M.-O. Mewes, M.R. Andrews, N.J. van Druten, D.S. Durfee, D.M. Kurn, and W. Ketterle, Phys. Rev. Lett. **75**, 3969 (1995).
C.C. Bradley, C.A. Sackett, and R.G. Hulet, Phys. Rev. A **55**, 3951, (1997).

[3] Kai Dieckmann, Igor Svarchuck, Martin Zielonkowski, Robert Spreeuw en Jook Walraven (Nog niet gepubliceerd).

Nawoord

Experimentele fysica is in hoge mate teamwerk. Dat is niet alleen zo omdat een experiment soms nu eenmaal meer handen en voeten nodig heeft dan een mens bezit, maar vooral ook omdat veel verschillende inzichten en vaardigheden nodig zijn. Bovendien is het prettig om samen te werken aan een mooi resultaat.

Een aantal van de mensen waarmee ik prettig heb samengewerkt, die me grandioos vooruit hebben geholpen, en waarvan ik het gewoon prettig vond dat ze in de buurt waren, wil ik bij deze noemen.

Aan mijn promotor Jook Walraven heb ik te danken, dat ik de mogelijkheid heb gehad in de waterstofgroep te promoveren. Jook's scherpe inzicht en oog voor detail zijn steeds een geweldige hulp en een uitmuntend voorbeeld voor me geweest, vanaf de tijd waarin ik met de apparatuur leerde omgaan tot die waarin Jook mijn manuscript kritisch doorlas.

Meritt Reynolds heeft het in dit proefschrift beschreven experiment ontworpen, en samen met mij opgebouwd, getest, uitgevoerd en geanalyseerd. Alleen dankzij Meritt's ideeën en plannen, en zijn enorme kennis van de materie kon dit experiment een succes worden.

Met Tom Hijmans heb ik vele meetsessies doorgebracht en nog meer interessante discussies gehad. Vaak gingen die niet over fysica, maar over de merkwaardige eigenschappen van bepaalde Europese talen, maar in ieder geval heb ik er steeds veel plezier aan beleefd.

Collega-promovendus Pepijn Pinkse heeft me een heleboel experimenteerkunsten geleerd. Ook als het wel eens tegenzat, en het experiment mij tot wanhoop dreigde te drijven, bleef Pepijn rustig en geduldig.

Groepstechnicus Bert Holsbeeke hielp ons niet alleen het omvangrijke (en weerbarstige) laserpark in stand te houden, hij heeft ook een belangrijke bijdrage aan de bouw van de fluorescentiedetector geleverd.

Joost Overtoom heeft vrijwel alle metalen onderdelen van de meetcel vervaardigd, en het succes van de metingen bewijst dat hij dat met vakmanschap en precisie gedaan heeft. Bovendien leverde hij steeds een belangrijke bijdrage aan de sfeer in het lab. Otto Höpfner heeft niet alleen uitstekende constructietekeningen gemaakt, hij heeft ook de waterstof-inlaatcombinatie ontworpen. De besprekingen met Otto en Joost over de haalbaarheid en maakbaarheid van wijzigingen en last-minute aanpassingen

aan het cel-ontwerp waren van cruciaal belang.

De precisie-optiek in de cel, zowel de magnesiumfluoride vensters als de lichtgeleiders van de fluorescentiedetector, zijn zeer vakkundig gemaakt door Michiel Groeneveld.

Ton Riemersma en Hugo Schlatter waren steeds bereid te helpen met metallurgische en chemische vraagstukken, en Bert Zwart en Eddie Ioeng hielpen ons met vacuümapparatuur en glasinstrumenten, bijvoorbeeld de glazen heliumzuiveraar. René Rik zorgde voor een probleemloze aanvoer van de levensbelangrijke koelvloeistoffen, en wist bij dreigende problemen altijd wat te regelen.

Verdere technische ondersteuning kregen we van Jan Dekker, Johan van de Ridder en Floris van der Woude, Flip de Leeuw, Theo van Lieshout en Edwin Baaij. Het computernetwerk heeft alle stormen doorstaan dankzij Thijs Post, Jaap Berkhout (die ook nog veel anekdotes uit zijn waterstof-tijd weet), Paul Langemeijer, Henk Pot en Derk Bouhuijs. Erik Hennes berekende magneetvelden voor ons.

Niet gering was ook de inzet van de administratieve ondersteunsters, onder andere Ineke Baay, Mariet Bos, Jenny Batson en Friedje Witzenhausen, en de mensen van het FOM-bureau.

Matthias Weidemüller bracht als post-doc veel nieuwe kennis en ideeën, en een geheel andere stijl van resultaten presenteren in de groep. Claus Zimmermann has co-developed the resonance-enhanced two-photon methods for probing hydrogen, which was not only used in the trapping experiments but also here.

It was a pleasure to discuss theoretical aspects of the work, and other unrelated matters, with Gora Shlyapnikov. Experimental aspects were also pleasurably discussed in Finland with our 'competitors' Simo Jaakkola, Sacha Safonov, Igor - Lukashevich, and Essa Tjukanov.

Collega-promovendi Kai Dieckmann en Peter Fedichev vertrokken al na een korte tijd naar AMOLF. Kai, gefeliciteerd met je condensaat!

Bij het ontwerpen en bouwen van de experimenteercel, vooral van de fluorescentiedetector, waren de vooronderzoeken van studenten Tycho Sonnemans en Susan Krieger zeer waardevol.

Ryer Jochemsen, Marco Eggenkamp en Richard van Rooijen hebben geholpen met het uitgloeien van de warmtegeleiders. Giorgio Frossati suggereerde een oplossing voor een lastig lekprobleem bij het celvenster, en de werkplaats van AMOLF maakte de daarvoor benodigde kunststofring.

Mijn voorgangers Irwan Setija en Jom Luiten lieten een goed verzorgde opstelling achter, waarmee Pavel Bouschev nu verder mag experimenteren.

Met Theo heb ik een heel mooi en lang artikel geschreven, en precies geleerd hoe moeilijk dat is. Toch had ik het gevoel dat Theo dat al wist...

Met de spectroscopisten van de verdichte materie Gerard, Rudolf, Willem, Ad, Mischa, Jaime, Gijs, Judith, Frank, Pedro, Johannes, Peter, Mark, Wim, Dirk en anderen heb ik een gezellige tijd op het lab en bij gelegenheid ook daarbuiten gehad.

Verdere labgenoten met wie ik aangenaam gepauzeerd en gewerkt heb wil ik nog noemen: Ben, Robert, Dirk, Bas, Stefan, Esther, Cor en Frederik; Eline, Heidi, Erik-Paul, Ruud, Nathalie; Gerard Bäuerle en Edy de Kerf, met wie ik een werkcollege heb voorbereid, en Barbara, die ik al eerder kende. Met Hessel heb ik een kelder en veel vage avonden gedeeld, en veel gelachen.

Het doen van onderzoek en het schrijven van een proefschrift vraagt niet alleen veel van de promovendus, ook zijn vrienden en familie ondervinden de indirecte gevolgen, van vermoeidheid en knorrigheid wegens drukte tot afgezegde afspraken wegens late metingen. Voor hun begrip, warmte en steun wil ik ze dan ook heel hartelijk bedanken.

Annemieke heeft me niet alleen steeds gesteund en geholpen, bij het werken aan dit proefschrift en bij al het andere, ze heeft ook steeds het vertrouwen bewaard dat het ergens goed voor is. Annemieke, met jou en Nina Simone zijn al mijn ogenblikken echt bijzonder.

List of publications

- Theory of semiballistic wave propagation
  A. P. Mosk, Th. M. Nieuwenhuizen and C. Barnes,
  Phys. Rev. B **53**, 15914 (1996).
- Adiabatically changing the phase-space density of a trapped Bose gas
  P.W.H. Pinkse, A. Mosk, M. Weidemüller, M.W. Reynolds, T.W. Hijmans, and J.T.M. Walraven,
  Phys. Rev. Lett. **78**, 990 (1997).
- Resonance enhanced two-photon spectroscopy of magnetically trapped atomic hydrogen
  P.W.H. Pinkse, A. Mosk, M. Weidemüller, M.W. Reynolds, T.W. Hijmans, J.T.M. Walraven and C. Zimmermann,
  Phys. Rev. Lett. **79**, 2423 (1997).
- Apparatus for optical study of atomic hydrogen on the surface of liquid helium
  A.P. Mosk, P.W.H. Pinkse, M.W. Reynolds, T.W. Hijmans,
  and J.T.M. Walraven,
  J. Low Temp. Phys. **110**, 199 (1998).
- One-dimensional evaporative cooling of magnetically trapped hydrogen
  P.W.H. Pinkse, A.P. Mosk, M. Weidemüller, M.W. Reynolds, T.W. Hijmans, and J.T.M. Walraven,
  Phys. Rev. A **57**, 4747 (1998).
- Optical excitation of atomic hydrogen bound to the surface of liquid helium
  A.P. Mosk, M.W. Reynolds, T.W. Hijmans, and J.T.M. Walraven,
  Phys. Rev. Lett. **81**, 4440 (1998).
- Comment on "A new type of evaporative cooling for neutral atoms"
  A.P. Mosk, M.W. Reynolds and T.W. Hijmans,
  Phys. Rev. Lett. **81**, 3046 (1998).
- Optical observation of atomic hydrogen on the surface of liquid helium
  A.P. Mosk, M.W. Reynolds, T.W. Hijmans and J.T.M. Walraven,
  J. Low Temp. Phys. **113**, 217 (1998).
- Photoassociation of spin-polarized hydrogen
  A.P. Mosk, M.W. Reynolds, T.W. Hijmans and J.T.M. Walraven,
  Phys. Rev. Lett. **82**, 307 (1999).